Seasat Views North America, the Caribbean, and Western Europe With Imaging Radar

J. P. Ford
R. G. Blom
M. L. Bryan
M. I. Daily
T. H. Dixon
C. Elachi
E. C. Xenos

November 1, 1980

Seasat Views North America, the Caribbean, and Western Europe With Imaging Radar

i. a

Seasat Views North America, the Caribbean, and Western Europe With Imaging Radar

J. P. Ford
R. G. Blom
M. L. Bryan
M. I. Daily
T. H. Dixon
C. Elachi
E. C. Xenos

November 1, 1980

iii

iv

Foreword

In June 1978, NASA launched Seasat, the first Earth satellite designed to study the oceans. Its payload included a synthetic aperture radar (SAR), which was also a first — the first scientific SAR to be placed in Earth orbit. When a spacecraft failure prematurely terminated the Seasat mission some 3 months after launch, the SAR had acquired images covering 100 million square kilometers, 65 million of these being of land. The land coverage concentrated on North America, the Caribbean, and Western Europe, with an image resolution of 25 meters.

The present atlas is a collection of 41 of the images, all of them digitally processed. Each SAR image is compared with a corresponding Landsat image or a sketch map to illustrate the capabilities of SAR for imaging land targets. It is expected that the material will be of interest to a wide audience, including university students who wish to explore the potential value of this new remote sensing tool. In turn, this should foster analysis of the remaining 99% of Seasat's SAR land images.

This SAR data set is a significant advance in the national effort to exploit space remote sensing platforms for the benefit of mankind. We hope that this atlas will give the reader some appreciation of the major contributions that we at JPL believe SAR can make to this endeavor.

Donald G. Rea
Assistant Laboratory Director
Technology and Space Program Development

Acknowledgment

Abstract

Forty-one digitally correlated Seasat synthetic-aperture radar images of land areas in North America, the Caribbean, and Western Europe are presented to demonstrate this microwave orbital imagery. The characteristics of the radar images, the types of information that can be extracted from them, and certain of their inherent distortions are briefly described. Each atlas scene covers an area of 90 X 90 kilometers, with the exception of the one that is the Nation's Capital. The scenes are grouped according to salient features of geology, hydrology and water resources, urban landcover, or agriculture. Each radar image is accompanied by a corresponding image in the optical or near-infrared range, or by a simple sketch map to illustrate features of interest. Characteristics of the Seasat radar imaging system are outlined.

Contents

Section I
Introduction

On June 29, 1978, the United States, through the National Aeronautics and Space Administration's Jet Propulsion Laboratory, launched Seasat, the first satellite dedicated to establishing the utility of microwave sensors for remote sensing of the Earth's oceans. The spacecraft carried five sensors in a nearly circular orbit with an inclination angle of 108°, at an altitude of 800 kilometers. Seasat circled the Earth 14 times each day.

One of the instruments onboard Seasat was a synthetic-aperture imaging radar (SAR). This instrument provided the first synoptic high-resolution radar images of the Earth's surface. The success of this complex sensor was a major technological advance, and it opened up a new dimension in our capability to observe, monitor, and study the Earth's surface.

On October 10, 1978, Seasat failed in orbit as a result of a massive short circuit in the electrical system. Fortunately, during the 3-1/3 months of orbital operations, the satellite returned a unique and voluminous set of data concerning the Earth's surface that permits us to make a preliminary assessment of the utility of orbital microwave remote sensors.

Only a limited number of ground stations were equipped to receive Seasat SAR data. The receiving stations were located at Goldstone, California; Fairbanks, Alaska; Merritt Island, Florida; Shoe Cove, Newfoundland, Canada; and Oakhanger, U.K. Consequently, SAR data were obtained over areas only where the satellite was in view of any one of these five stations, and image coverage is limited to North America, parts of Central America and the Caribbean, and parts of Western Europe. The total amount of data collected corresponds to about 2500 minutes of operation. This is equivalent to approximately 100 million square kilometers areal coverage.

At the ground processing facility, the radar-signal data were correlated to generate radar images. This was done optically for all data, and digitally for a selected number of 100 X 100 kilometer scenes. Details of the data processing are given by Jordan (1980) and Wu (1980).

This atlas presents a number of SAR images of land areas. The images were selected to show a wide range of features with geologic and hydrologic interest, and to include areas of urban landcover and agriculture. The intent is to provide the scientific, academic, and user community with examples, and to familiarize them with spaceborne radar images.

The atlas was compiled by J. P. Ford with the assistance of E. C. Xenos, and edited by J. P. Ford with the assistance of D. E. Fulton. Section II by C. Elachi and J. P. Ford summarizes the characteristics of the Seasat SAR images, the types of information that can be extracted from them, and certain of their inherent distortions. More extensive details are to be found in papers by Beal (1980), Elachi (1980), Ford (1980), and Sabins, et al. (1980). The arrangement and the main pictorial section of the atlas is presented in Section III. Appendix A by C. Elachi provides a brief summary of the Seasat SAR system. Appendix B by J. P. Ford is a glossary of the acronyms and technical terms in remote sensing and geology as used in this report. Appendix C is an index of the images that appear in the atlas.

Section II
Characteristics of the Seasat SAR Images

The SAR provides images that represent the reflectivity of the surface at the operating frequency in the backscatter direction. The image brightness is directly proportional to the surface backscatter cross section. In the decimeter spectral region (Seasat radar wavelength is 23.5 cm), the backscatter energy is dependent primarily on the surface physical properties (i.e., average slope and small-scale roughness), and the surface and near-surface dielectric constant, which is a function of the surface composition, cover, and moisture content.

The interpretation of radar images is based on geometric patterns, forms, and shapes, and on image tone and texture. Examples of features represented by the former are lineaments, joints, folds, domes, drainage patterns, fracture patterns, cultivated fields, and highways. The patterns, forms, and shapes are interpreted in a way similar to that used with aerial photography. The interpreter has to keep in mind that the radar return is extremely sensitive to the surface slope, and that the radar geometry is different from that of aerial photography.

The radar image tone and texture are primarily a function of the surface roughness at the scale of the radar wavelength, the change in topography at the scale of the resolution element, and the surficial electric properties. The tonal and textural data in the radar image provide new information that is not available with optical or infrared sensors. Their interpretation requires an understanding of the interaction of electromagnetic waves with natural surfaces in the microwave region. In general terms, the image tone in the Seasat SAR image is high if the surface is either rough at the scale of 10 to 30 centimeters, inclined toward the radar, moist or damp, covered by vegetation, or any combination of these conditions. For more details on the backscattering properties from natural surfaces, the reader is referred to the text by Long (1975).

With Seasat SAR, users are cautioned not to use the image tone for quantitative measurement because the system was not calibrated, and a number of nonlinear processes such as clipping and saturation are inherent in certain of the subsystems.

The image format of the Seasat SAR system contains distortions that result from motion of the spacecraft relative to the Earth, and distortions due to the imaging geometry. In the first instance, distortions arise from the effects of the Earth's rotation and curvature, and from differences in pixel dimensions in the along-track (azimuth) and across-track (range) directions. Pixel size in the along-track direction varies with the relative velocity between the spacecraft and the image target on Earth at any particular Earth latitude. Pixel size in the across-track direction varies with the range distance between the spacecraft nadir and the target. For the digitally correlated images presented in this atlas, the pixel sizes are approximately 16 meters in the along-track direction, and vary from about 19.4 meters in the near range to about 14.8 meters in the far range across track.

Distortions due to the imaging geometry are inherent in all SAR imaging systems, as the radar-image format basically

Preceding page blank

represents the slant range, or distance from the radar to each of the respective surface elements in the scene. The Seasat SAR imagery is presented in slant-range format and has not been geometrically corrected for ground-range format or compensated for Earth's curvature. The effect is illustrated in Figure 1, where the ground ranges abc appear as slant ranges $a_1 b_1 c_1$ on the radar imagery.
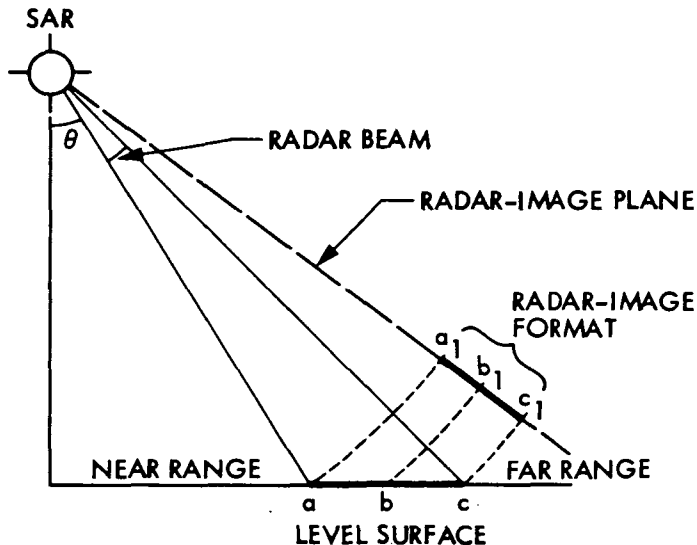
Figure 1. Radar-image format showing slant-range presentation $a_1 b_1 c_1$ relative to ground-range abc, assuming a level surface. Long-dashed line represents radar-image plane. Look angle θ is inclination of the radar beam off vertical

A further set of geometric relief displacements in the Seasat SAR images that is characteristic of all imaging radars is the apparent variation in length of equal terrain slopes when the respective slope lengths are imaged at different incidence angles. The displacements result in (1) foreshortening, (2) layover, and (3) shadowing. These effects are feature-dependent and cannot be easily corrected.

A. Foreshortening

Slopes inclined toward the radar appear compressed relative to slopes inclined away from the radar. The effect is illustrated in Figure 2. The foreshortening factor F_f is approximately:

$$F_f = \sin (\theta - \alpha)$$

where the look angle θ is the angle between the vertical plane and a line that links the imaging-radar antenna to a feature on the ground, and α is the slope angle of the surface. Alpha is positive (α^+) where the slope is inclined toward the radar (foreslope), and negative (α^-) where the slope is inclined away from it (backslope).
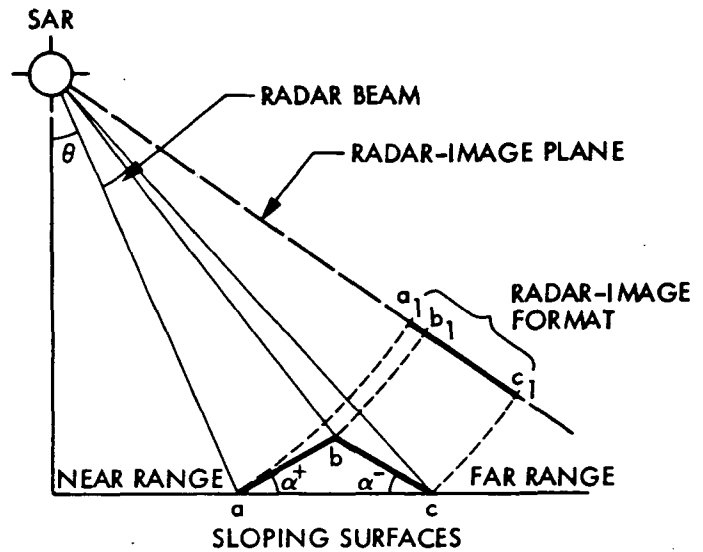
Figure 2. Radar foreshortening of slope ab, which is projected as $a_1 b_1$, relative to slope bc, which is projected as $b_1 c_1$, showing look angle θ, foreslope angle α^+, backslope angle α^-. Long-dashed line represents radar-image plane

B. Layover

Layover is an extreme case of foreshortening that occurs when the look angle θ is smaller than the foreslope α^+ ($\theta < \alpha^+$). This is illustrated in Figure 3. In this case, a moun-
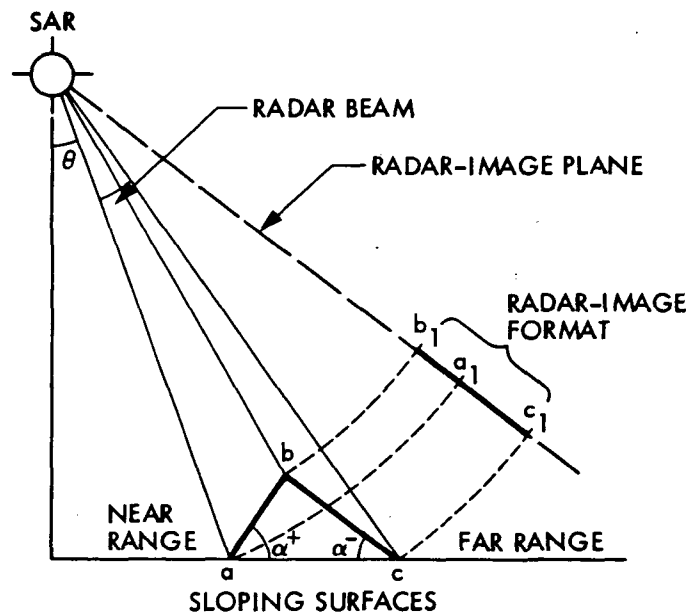
Figure 3. Radar layover of slope ab projected as $b_1 a_1$ on radar image, where look angle θ is smaller than slope angle α^+. Long-dashed line represents radar-image plane

4

tain appears laid over on its side. The effect occurs on Seasat SAR images whenever a foreslope as seen by the radar exceeds about 20°. An excellent example appears on the Mount McKinley National Park, Alaska, image 31 in this atlas. This distortion cannot be corrected even when the surface topography is known because return signals from spatially separated locations in the across-track direction arrive at the radar receiver simultaneously, and appear superimposed on the image.

C. Shadowing

Shadowing is essentially the opposite of foreshortening. Slopes inclined away from the radar are in shadow when the look angle θ plus the backslope angle α^- are greater than 90° $[(\theta - \alpha^-) > \pi/2]$. Shadows are caused by ground features that obstruct the radar beam and prevent illumination of the area behind them. This effect occurs on Seasat SAR images whenever the backslope in the radar viewing direction exceeds about 70°. It is shown diagrammatically in Figure 4.

Figure 4. Radar shadow of surface *bcd* projected as b_1d_1 on radar image. Long-dashed line represents radar-image plane

D. Look Direction

Because the Seasat SAR was a single right-side-looking system orbiting in an inclined plane (108°), images of certain scenes were acquired from two different look directions. The look direction for any given image is determined from the bearing of the spacecraft at the time of image acquisition. The direction of the radar illumination has a pronounced effect on feature perception in any given scene, especially with respect to the perception of linear features of natural or cultural origin. The extent to which linear features are enhanced or suppressed on the imagery depends significantly on their orientation relative to a given direction of radar illumination. Consequently, some linear features that appear dark or are imperceptible in one look direction may appear bright in the other look direction. Some scenes that were illuminated by the Seasat SAR from different look directions are given in the atlas as examples. The scenes are: Folded Appalachians, Pennsylvania (I) and (II) (image numbers 1 and 2); Los Angeles, California (I) and (II) (image numbers 34 and 35); and New Orleans, Louisiana (image number 37).

E. Artifacts

The Seasat SAR images presented in this atlas have been selected from among the better quality images available. Occasionally, certain artifacts and defects that occurred during the acquisition or processing tend to mar the images. Some notable artifacts and defects include range offset, a line in the along-track direction, and local defocusing. Range offset takes the form of feature doubling on the image in the across-track direction. It represents approximately one second of image-acquisition time during which the radar receiver sensitivity time control (STC) was shifted to compensate for variation in the antenna gain. A line through the center of the image in the along-track direction generally results from a radar-calibration pulse. Local defocusing is a complex defect that arises in correlation of the images. Obvious acquisition and processing defects are noted in the captions of the images where they occur.
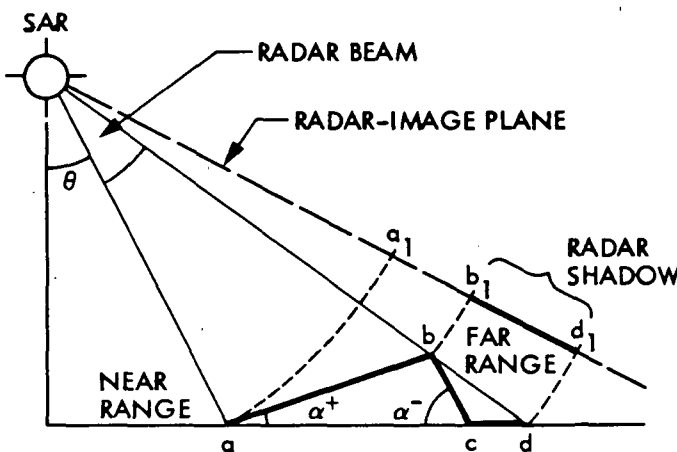
Section III
Atlas Arrangement and Description of Seasat SAR Images

The Seasat SAR images presented here consist of thirty-two scenes in the U.S.A., three scenes in Western Europe, two scenes each in Mexico and the Caribbean, and one scene each in Greenland and Iceland. Figure 5 shows the locations of the scenes in the conterminous United States, Mexico, and the Caribbean. The scenes in Alaska, Greenland, and Iceland are located in Figure 6. The locations of scenes in Western Europe are shown in Figure 7. In addition, these figures provide the locations of the respective receiving stations.

All the Seasat images in this atlas were digitally correlated on the JPL processor. The image contrast of certain images has been enhanced at the JPL Image Processing Laboratory, or at the Photo-Duplication Laboratory. The images cover an area of 90 X 90 kilometers, except that of the Nation's Capital (image 33). Each Seasat image is accompanied by a corresponding image in the optical or near-infrared range for comparison purposes, or by a simple sketch map to illustrate features of interest. The corresponding image in the optical or near-infrared range is a single Landsat multispectral scanner (MSS) image, except one example each of a return beam vidicon (RBV) image and an aerial photograph. For each scene in the atlas, the material is presented on facing pages, with the Seasat SAR image on the left.

The vertical left and right margins of each Seasat image parallel the satellite orbital path at the time of image acquisition.

The stepwise aspect of these margins is a processing artifact that results from corrections to compensate for the Earth's rotation. The direction of radar illumination in each case is specified by an arrow below the image. In cases where the radar illumination is toward the northeast quadrant, the arrow is situated at the lower left and points to the right. In cases where the radar illumination is toward the northwest quadrant, the arrow is situated at the lower right and points to the left. A north arrow provides the appropriate geographic-reference datum in each case.

Although current availability influenced the selection of scene material, the images were chosen for their scene-specific content in the areas of geology, hydrology and water resources, urban landcover, and agriculture. The range of topics selected is apparent from the Contents. The scenes span an area from 18°N latitude (Jamaica, W.I.) to 71°N latitude (Dease Inlet, Alaska), and from 6°E longitude (Geneva, Switzerland) to 164°W longitude (Unimak Island, Alaska). Included among the scenes are such notable features as the highest peak in North America (Mount McKinley, Alaska), the lowest land elevation in North America (Death Valley, California), the oldest rocks on Earth (Isua region, Greenland), the largest active sand dune field in North America (Sonora Dunes, Mexico), the largest urban landcover in North America (Los Angeles, California), and the Nation's Capital (Washington, D.C.).
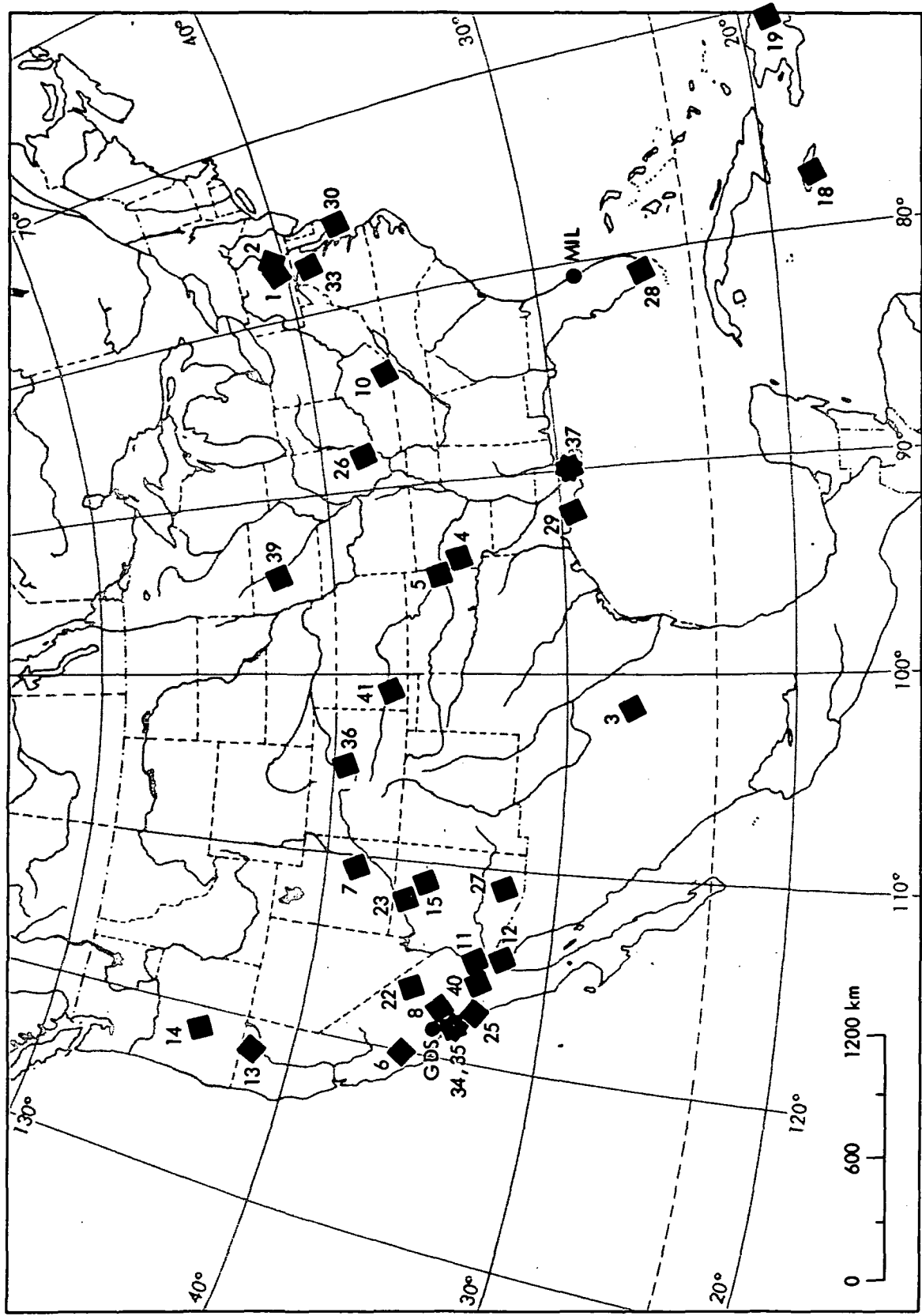
Figure 5. Geographic locations in the conterminous United States, Mexico, and the Caribbean of the numbered images; receiving stations for the images were Goldstone (GDS), California, and Merritt Island (MIL), Florida
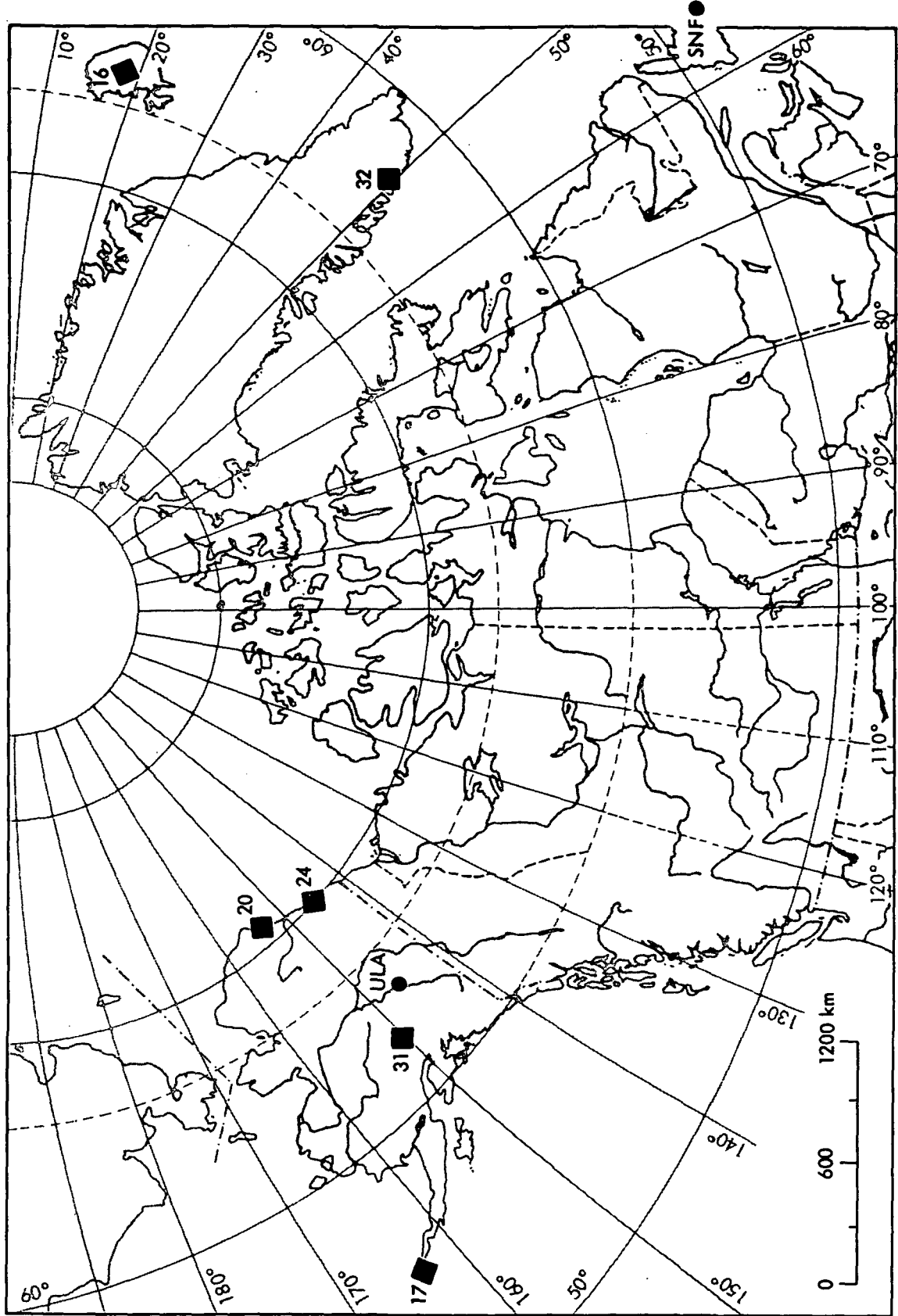
Figure 6. Geographic locations in Alaska, Greenland, and Iceland of the numbered images; receiving stations for the images were Fairbanks (ULA), Alaska, and Shoe Cove, Newfoundland (SNF), Canada
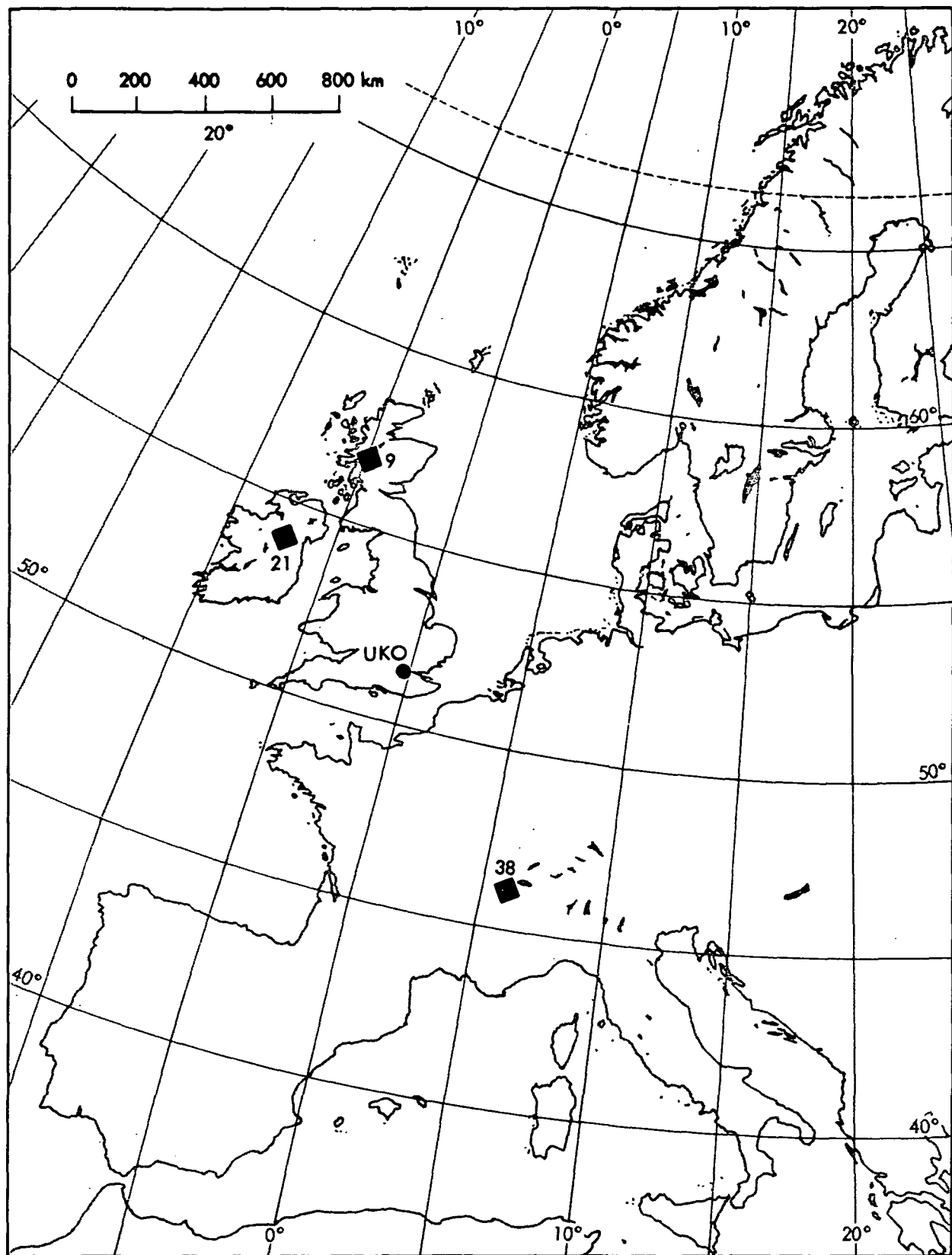
Figure 7. Geographic locations in Western Europe of the numbered images; receiving station for the images was Oakhanger (UKO), United Kingdom

A. Geology

(i) Fold Structures
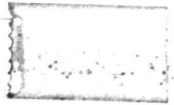
13

ILLUMINATION
DIRECTION →

N

0   10   20 km
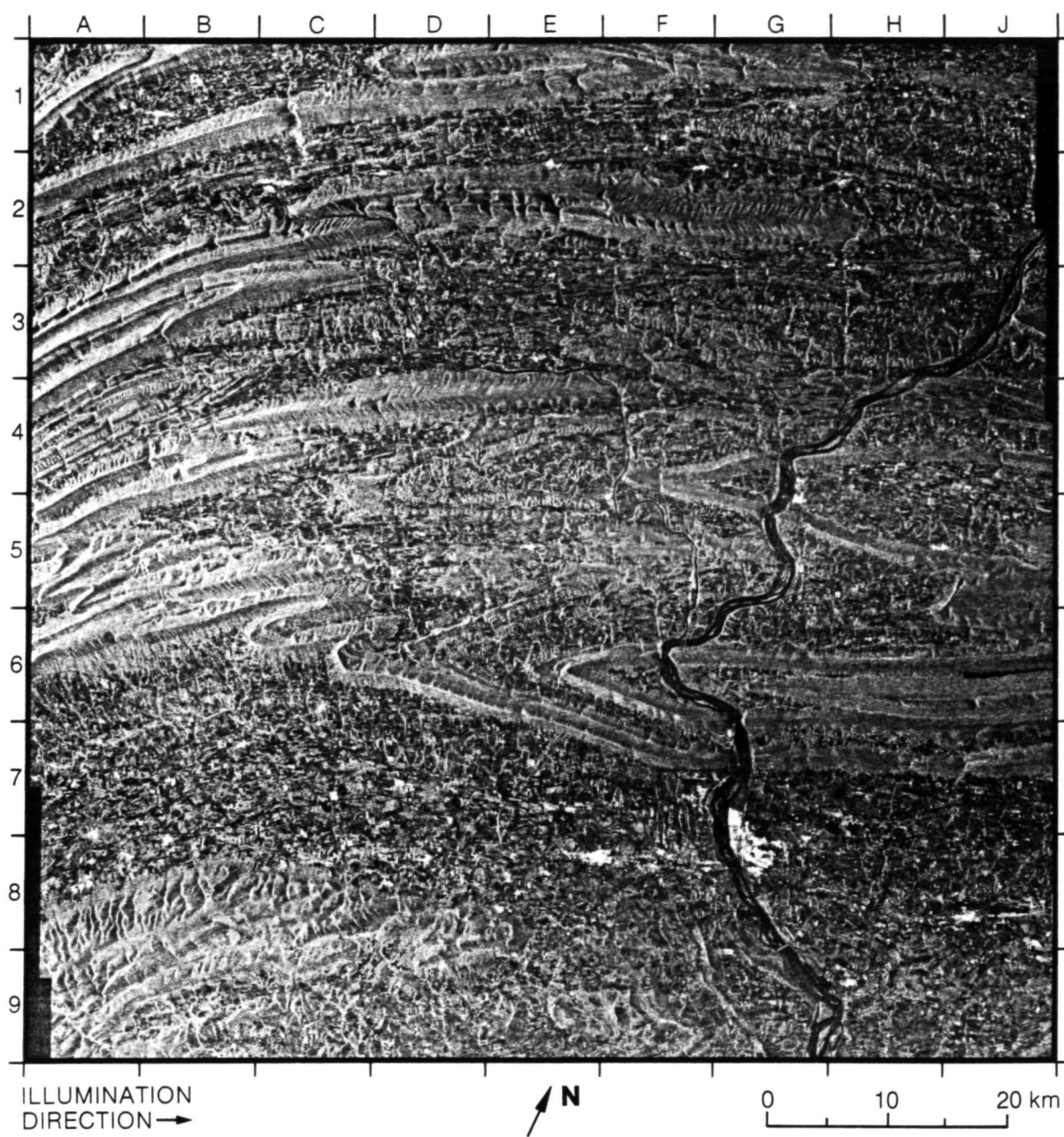
This scene depicts the folded Appalachian Mountains in east-central
Pennsylvania. The pattern of "noses" formed by the mountains and valleys on
the image represents plunging structures, such as the synclines at E6, F4, and
J3, and the anticlines at G5, C2, and H2. Regional drainage crosses the
structural strike as demonstrated by the Susquehanna River (J2 to G9) and its
major tributary, the Juniata River (A3 to F6). The course of the Susquehanna
River through the mountains directly northwest of Harrisburg is a classic
example of a major water gap. Lesser concordant streams, such as the
Conodoguinet Creek, are deeply incised in a meander valley, especially
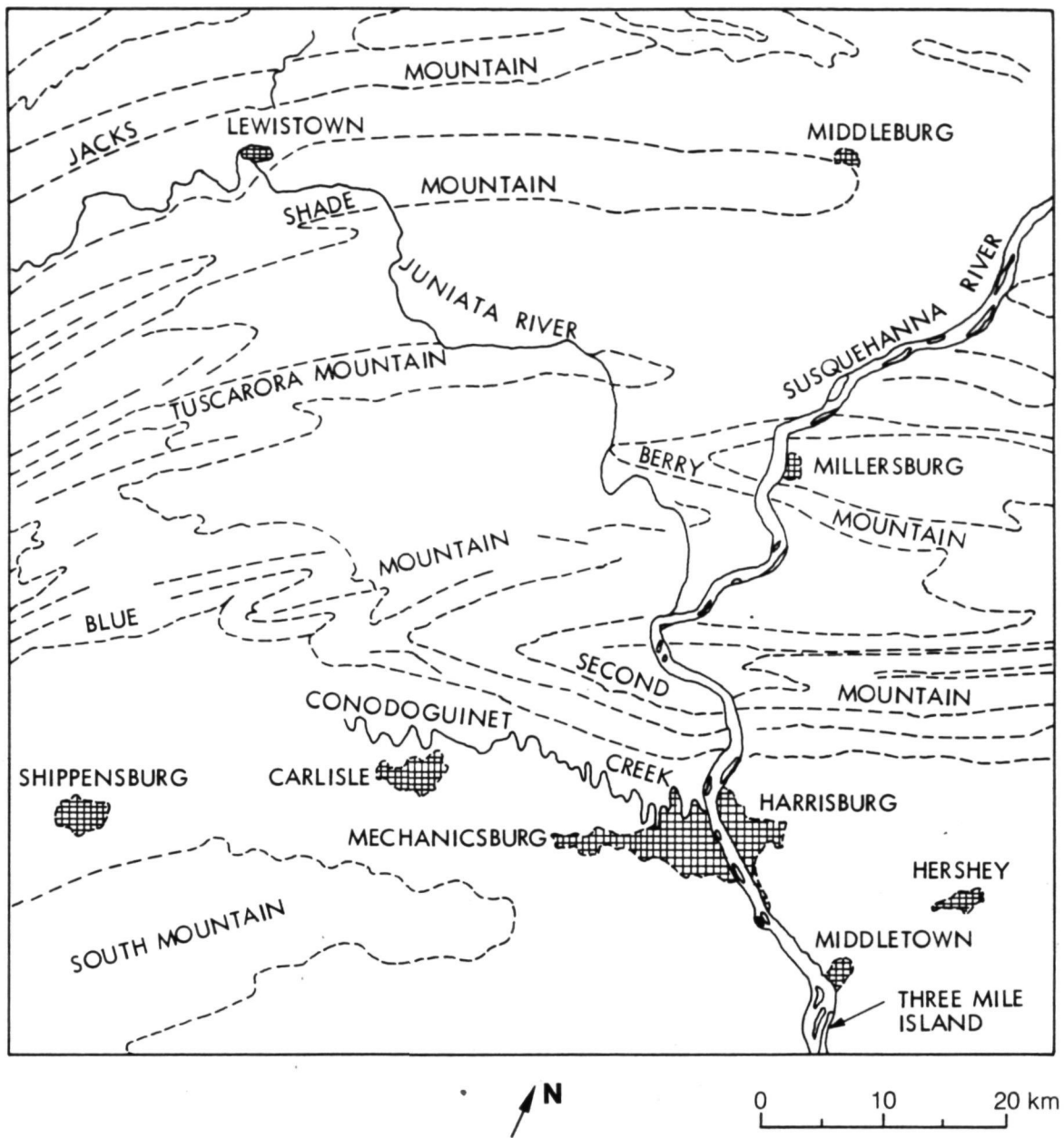
between Mechanicsburg and Harrisburg. The heavily forested mountain slopes exhibit fine, smooth texture and generally low image contrast because most of the mountains are elongated features that strike almost parallel to the direction of radar illumination. By comparison, the valleys have a wide range of image tone and texture. The patterns reflect the human occupancy of the area, including numerous cities and extensive agricultural usage. Three Mile Island is situated in the lower right corner of G9.

(Seasat image from Rev. 1296.)

2. Folded Appalachians, Pennsylvania (II)

0   10   20 km   N   ILLUMINATION
← DIRECTION
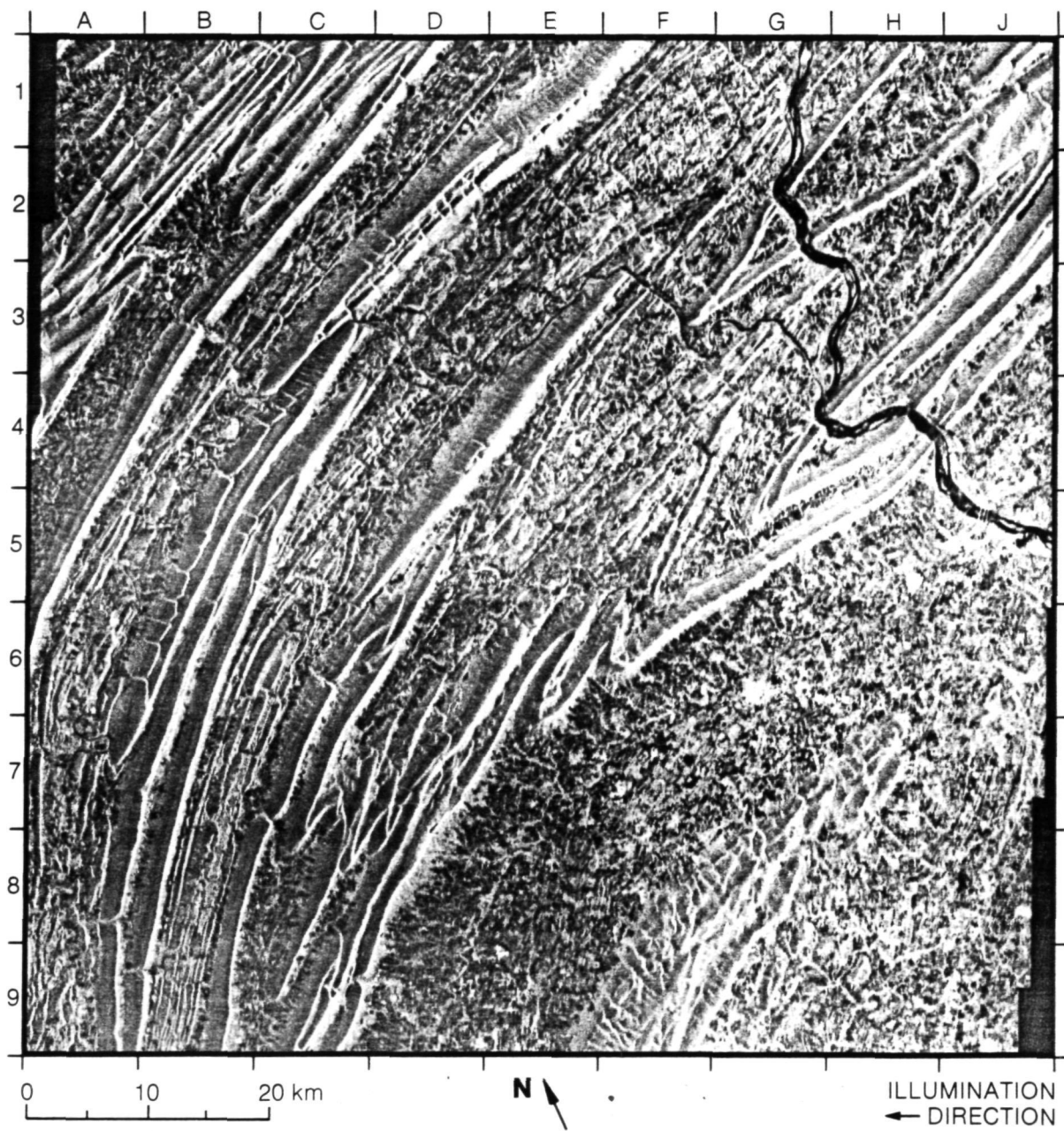
This scene covers approximately the same area as that shown in Appalachians (I), but it is illuminated by the radar from a different viewing direction. Slopes that face toward the radar appear very bright in contrast with slopes that face away, which appear quite dark. A good example is Tuscarora Mountain from D5 to F3, where the orientation of the linear topography is oblique to the illumination direction of the radar. Correspondingly, where Tuscarora Mountain is oriented almost parallel to the radar illumination direc-
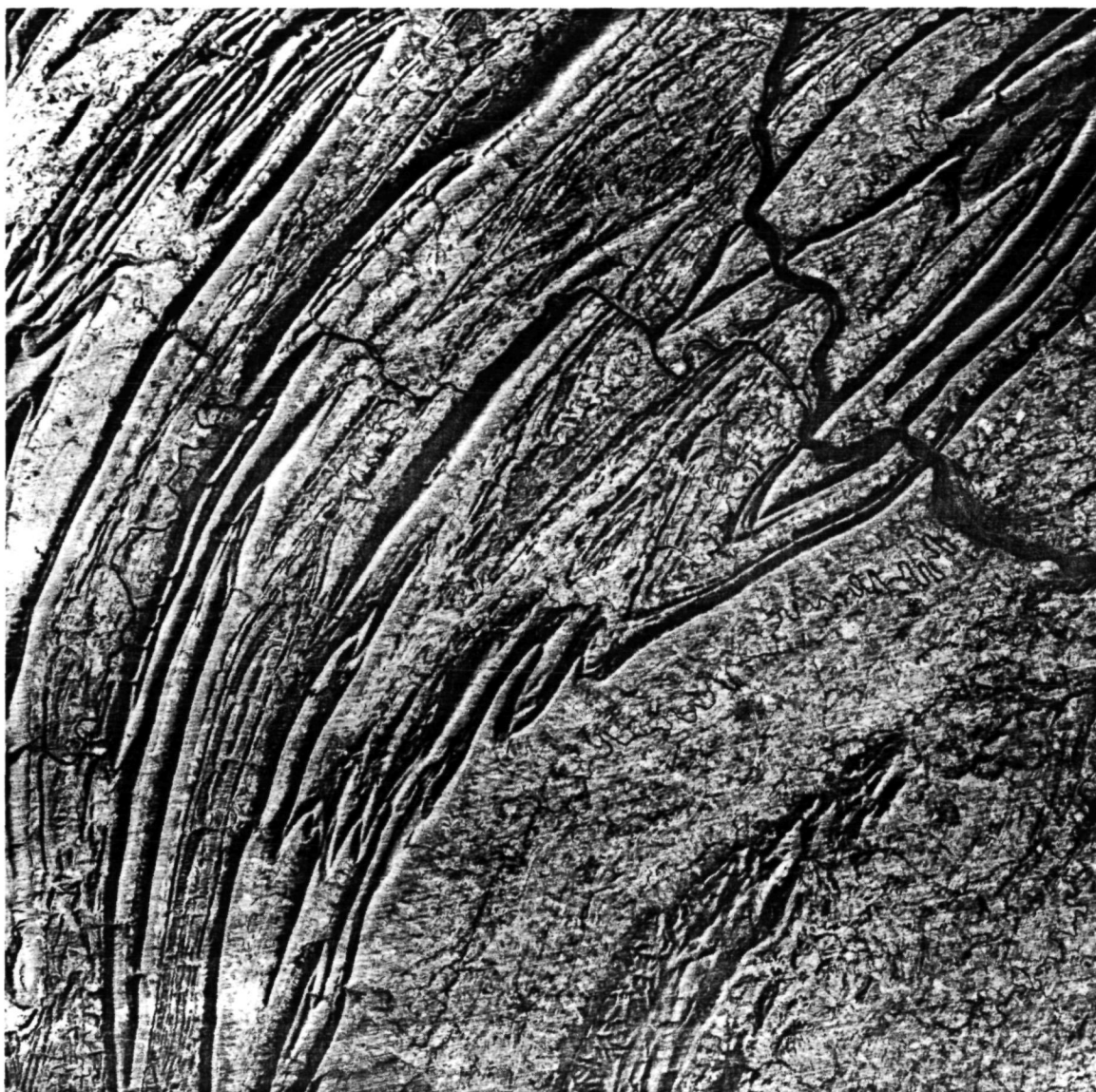
N ↑   0   10   20 km

tion on the Seasat image of Appalachians (I) (B4 to F4), the slopes appear uniformly dark.

On the Landsat image above, the mountain slopes, including Tuscarora, that face toward the sun appear bright, but due to the low sun elevation the slopes that face away from the sun are in shadow.

(Seasat image from Rev. 759; Landsat scene ID: 1171-15245.)

3. Sierra Madre Oriental, Mexico

ILLUMINATION DIRECTION ➡

↗ N

0   10   20 km
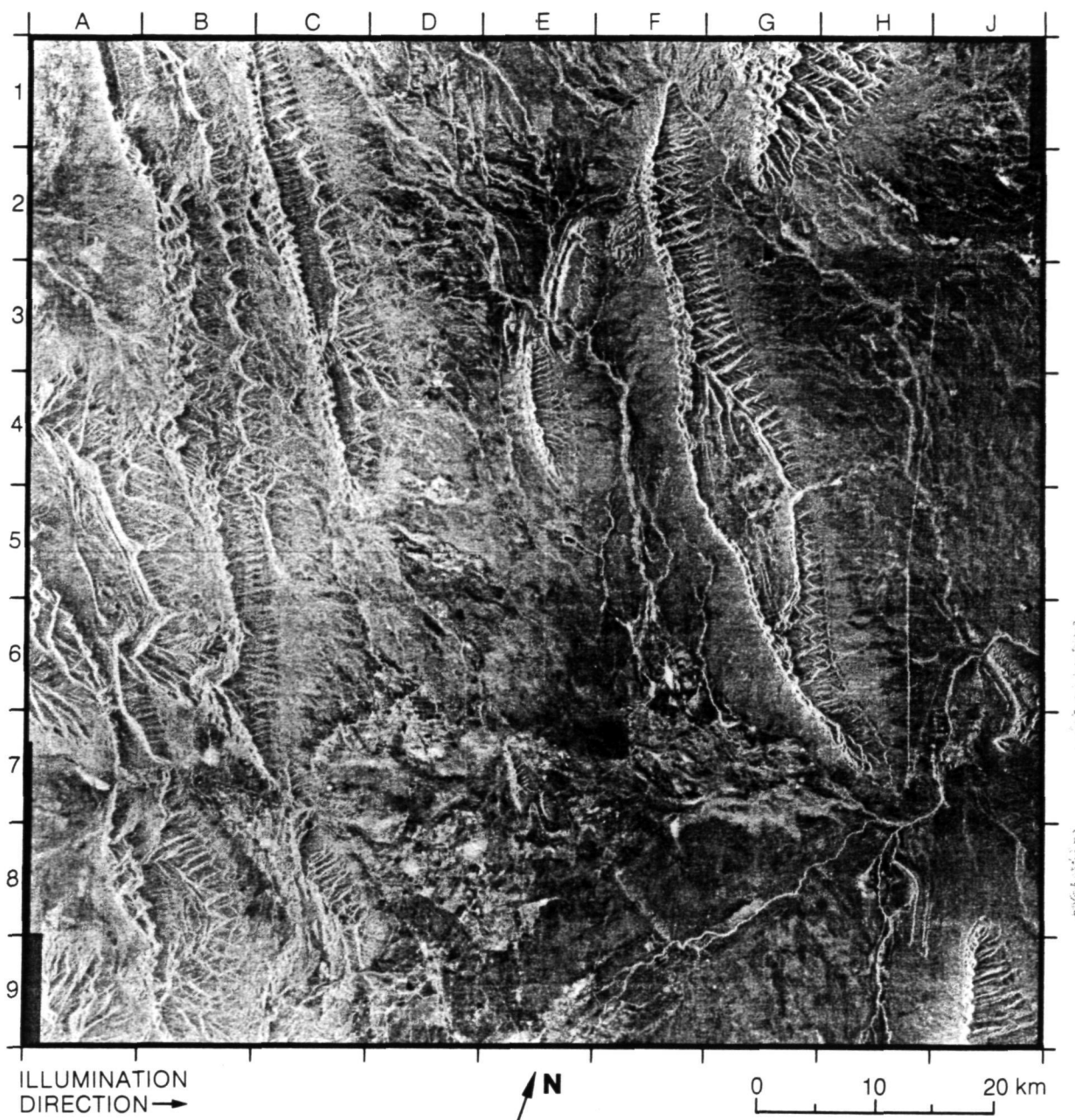
Upper Cretaceous sedimentary rocks are exposed in the slopes of the Sierra Madre Oriental fold belt, northeast Mexico. The extensive pattern of small flat irons along the slopes denotes layered rocks, and the elliptical patterns, notably in E3, E4, and F4 to G5, denote doubly plunging anticlines. Petroleum and mineral deposits are frequently associated with this type of
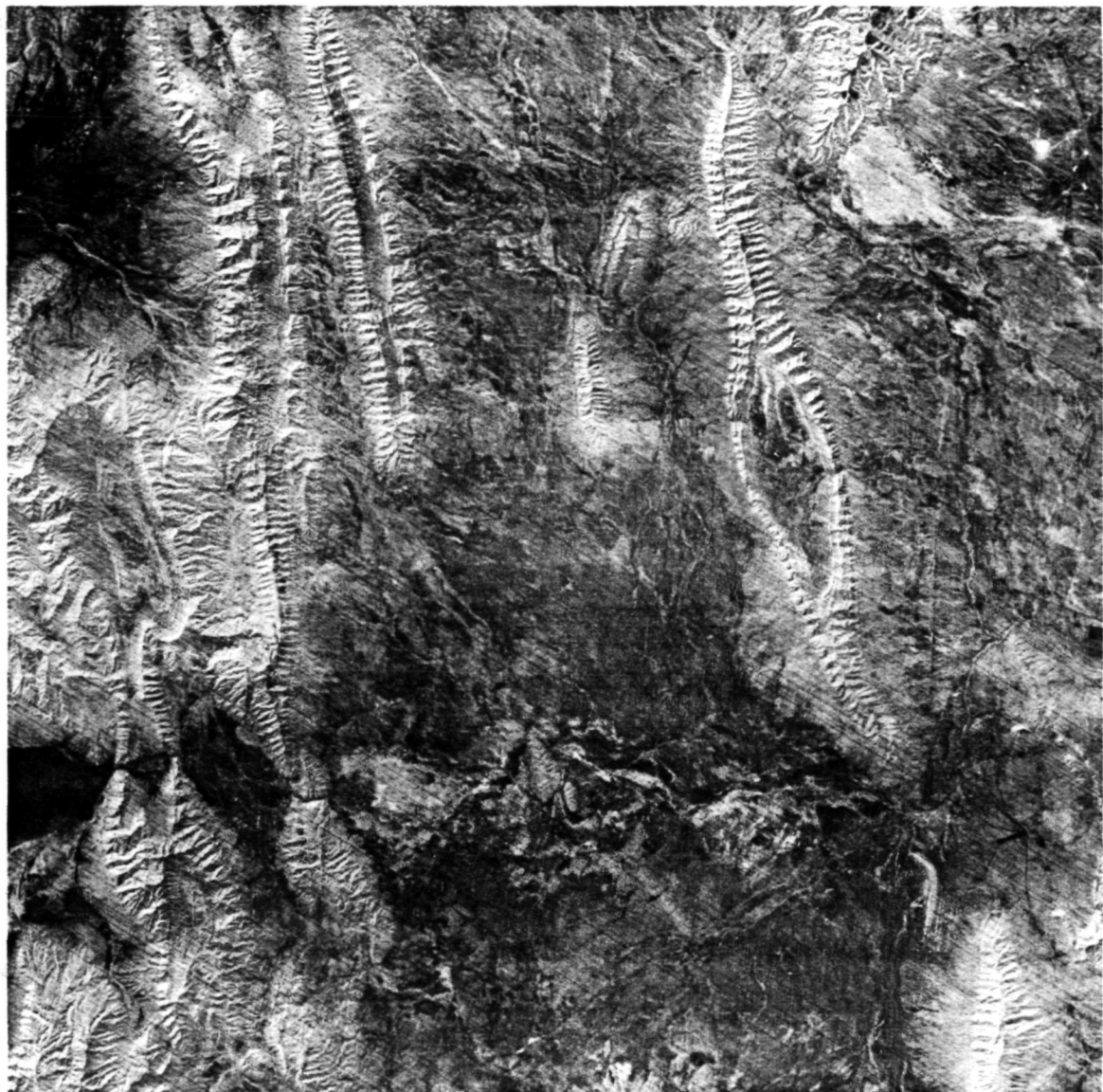
N   0   10   20 km

structure. Alluvium and lacustrine deposits fill the low spaces between the slopes. Contrast topographic detail on the Seasat image with the Landsat MSS image above.

(Seasat image from Rev. 738; Landsat scene ID: 2055-16372.)

4. Ouachita Mountains, Oklahoma-Arkansas

ILLUMINATION DIRECTION →

↗ N

0   10   20 km
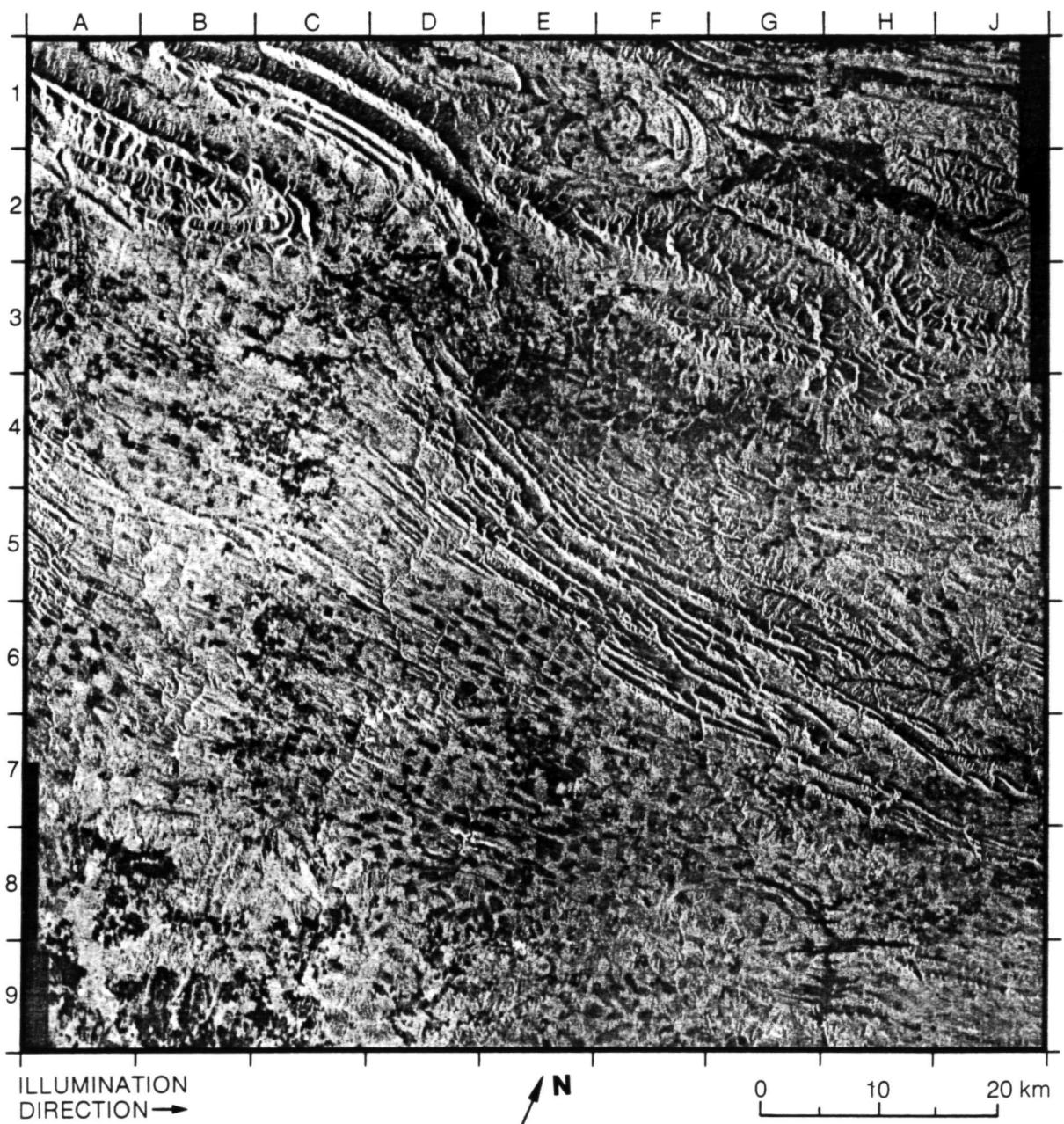
The Ouachita Mountains northwest of Mena, Arkansas (D3 and E3), are relatively rugged and provide some of the southern-most prominents north of the Gulf of Mexico. The top of Rich Mountain (C1) rises more than 350 meters above the surrounding valleys, making it one of the higher mountains in Oklahoma.

Three reservoirs, Lake Greeson (G8 to G9 through H8 to H9), Dierk's Lake (D7 to D8), and Gillham Lake (C6 to C7 through D6 to D7) provide prominent identification features on the Landsat image (right). The two western-most reservoirs are less obvious on the Seasat image because the water levels were slightly lower when the image was acquired. In addition, the land-use patterns surrounding Dierk's Lake (D7 and D8) are very similar in image tone to the
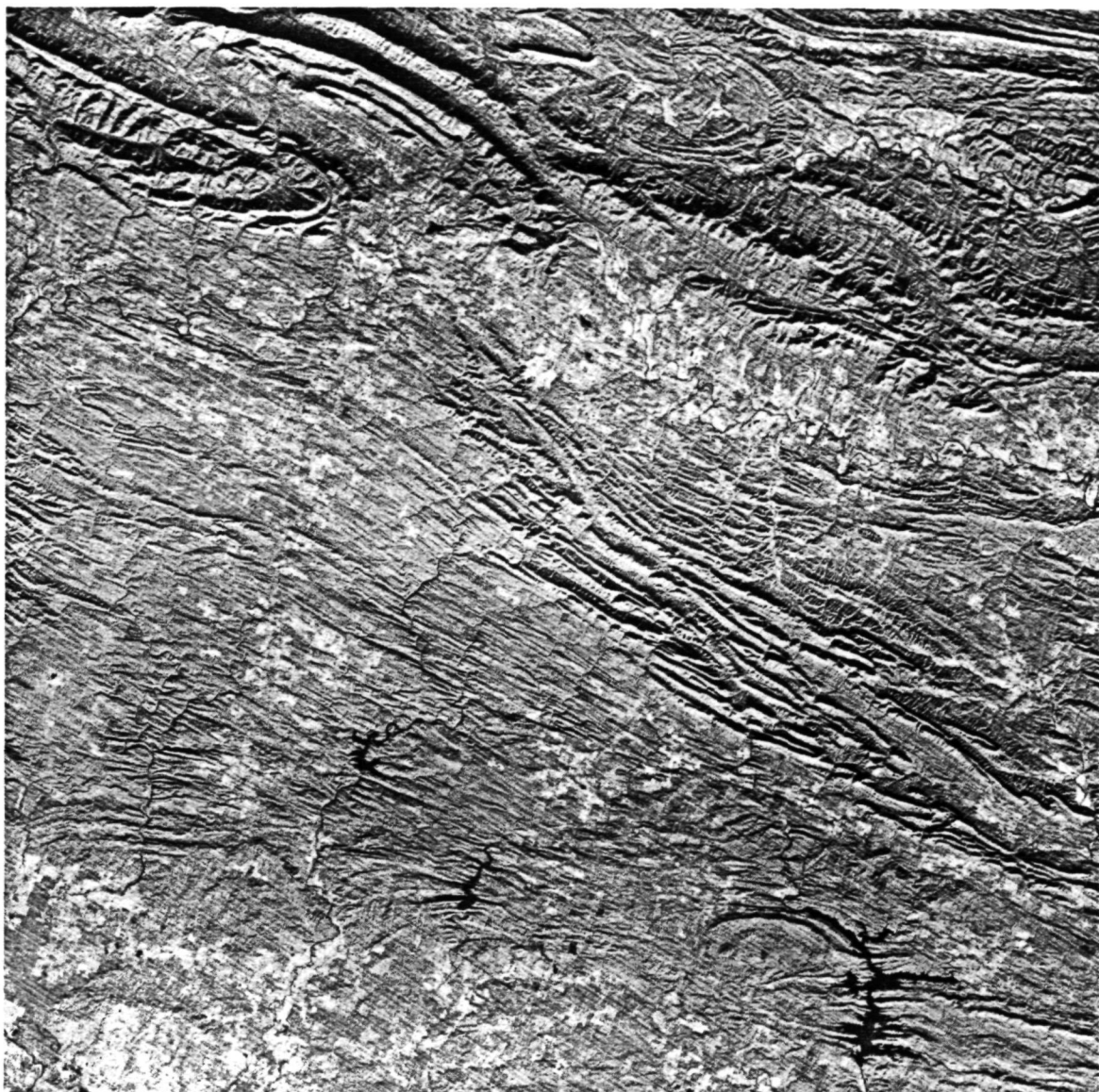
↑ N   0   10   20 km

water surface itself, thus providing only minimal contrast. The checkerboard pattern of forest clearcut regions (patches of low return or dark tone) on the Seasat image (E6 to E7) is not as apparent on the Landsat scene. However, the Landsat image illustrated here is band 7, and the image of band 5 provides a significant increase in the visibility of clearcut areas over that of the Seasat.

Numerous folds and faults that are detectable on the Landsat image are not easily distinguished on the Seasat image (see for example areas A3 to B3 and A6 to B6).

(The caption and the selection of this Landsat image are by courtesy of Prof. H.C. MacDonald, Department of Geology, University of Arkansas.)

(Seasat image from Rev. 795; Landsat scene ID: 5261-15492.)

21

5. Arkoma Basin, Oklahoma-Arkansas

ILLUMINATION DIRECTION→   N   0   10   20 km
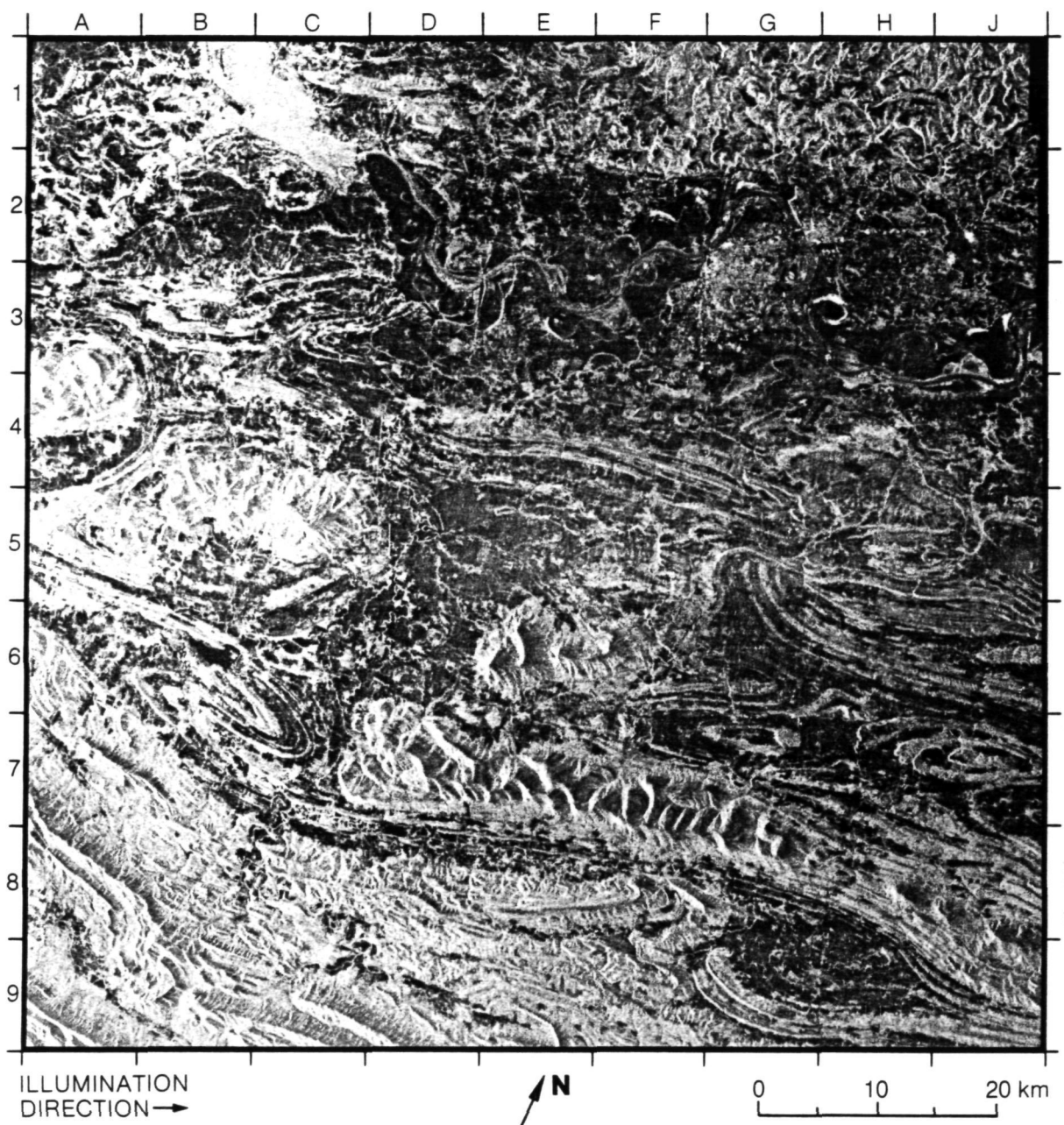
The Arkoma Basin has an arcuate shape that parallels the eastward flowing Arkansas River between the Ozark uplift on the north and the Ouachita Mountains on the south. Fort Smith, Arkansas (G2 and G3) is in the center of the Arkoma Basin. Moderate folding characterizes the northern Ouachita Mountains (A4 to A5 through J4 to J5), whereas intense folding and imbricate thrusting is the tectonic style recorded to the south (A8 to A9 through F8 to F9).

Because of relatively low solar illumination, the Landsat image (right) provides definition of structural features not readily apparent on the Seasat image. Hogback ridges (areas E4 to F4 and A5 to A6 through B5 to B6) are difficult to distinguish on the Seasat image. An area of tight folding and faulting (B8 to B9)
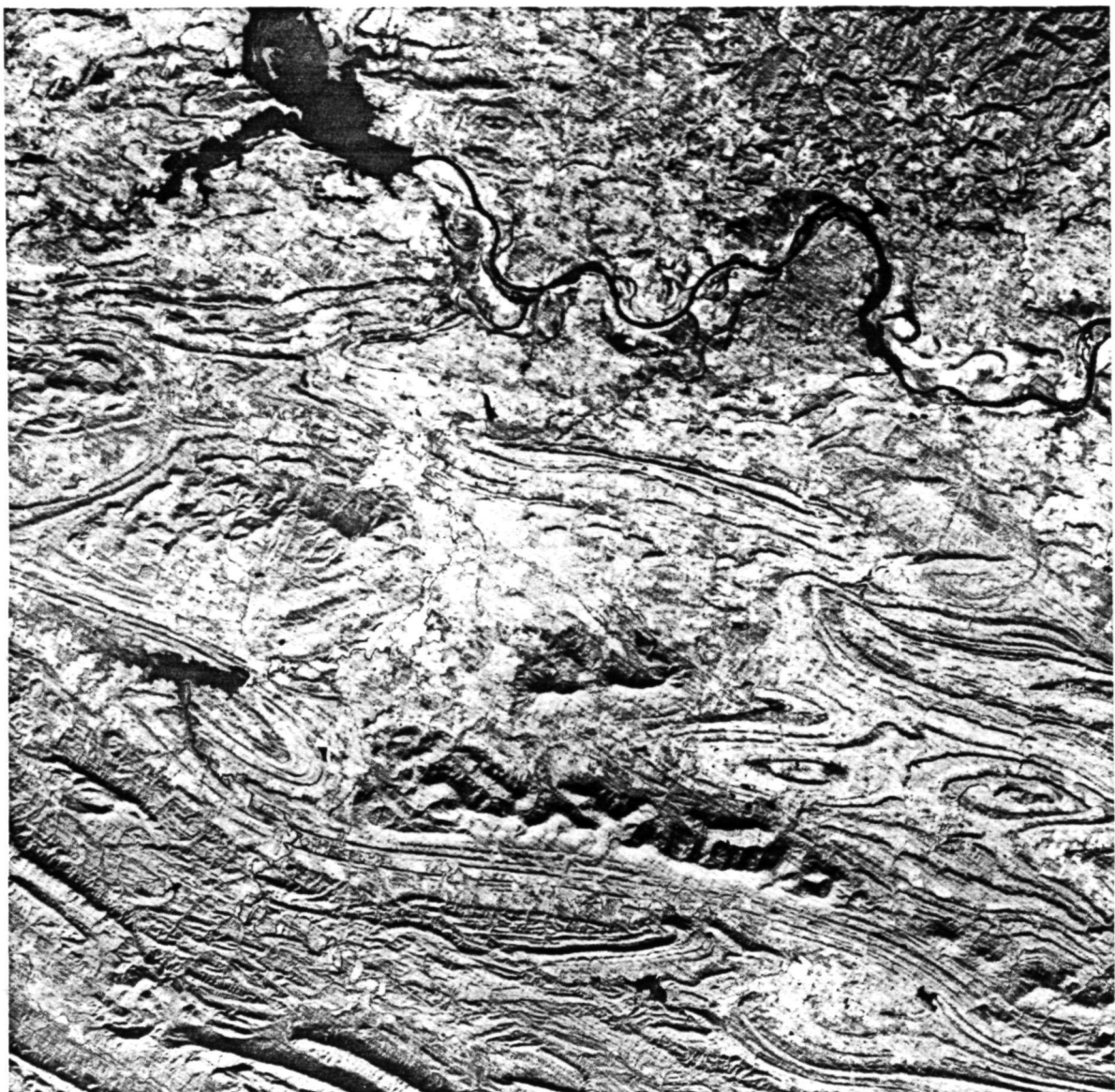
N   0   10   20 km

is poorly defined on the Seasat image. However, in several areas (see for example area A6), small folds are apparent on the Seasat image that are not obvious on the Landsat. A complementary mode for Seasat/Landsat operation is suggested. Lake Robert S. Kerr in the northwest corner of the Landsat image (B1 to B2 through C1 to C2) is not readily apparent on the Seasat image because of the choppy water on the date of radar imaging.

(The caption and the selection of these Landsat images are by courtesy of Prof. H.C. MacDonald, Department of Geology, University of Arkansas.)

(Seasat image from Rev. 795; Landsat composite scene ID: 5244-15555, 5261-15492, 5261-15490, and 5244-15561.)

6. Kettleman Hills, California

0 — 10 — 20 km

N

ILLUMINATION
← DIRECTION
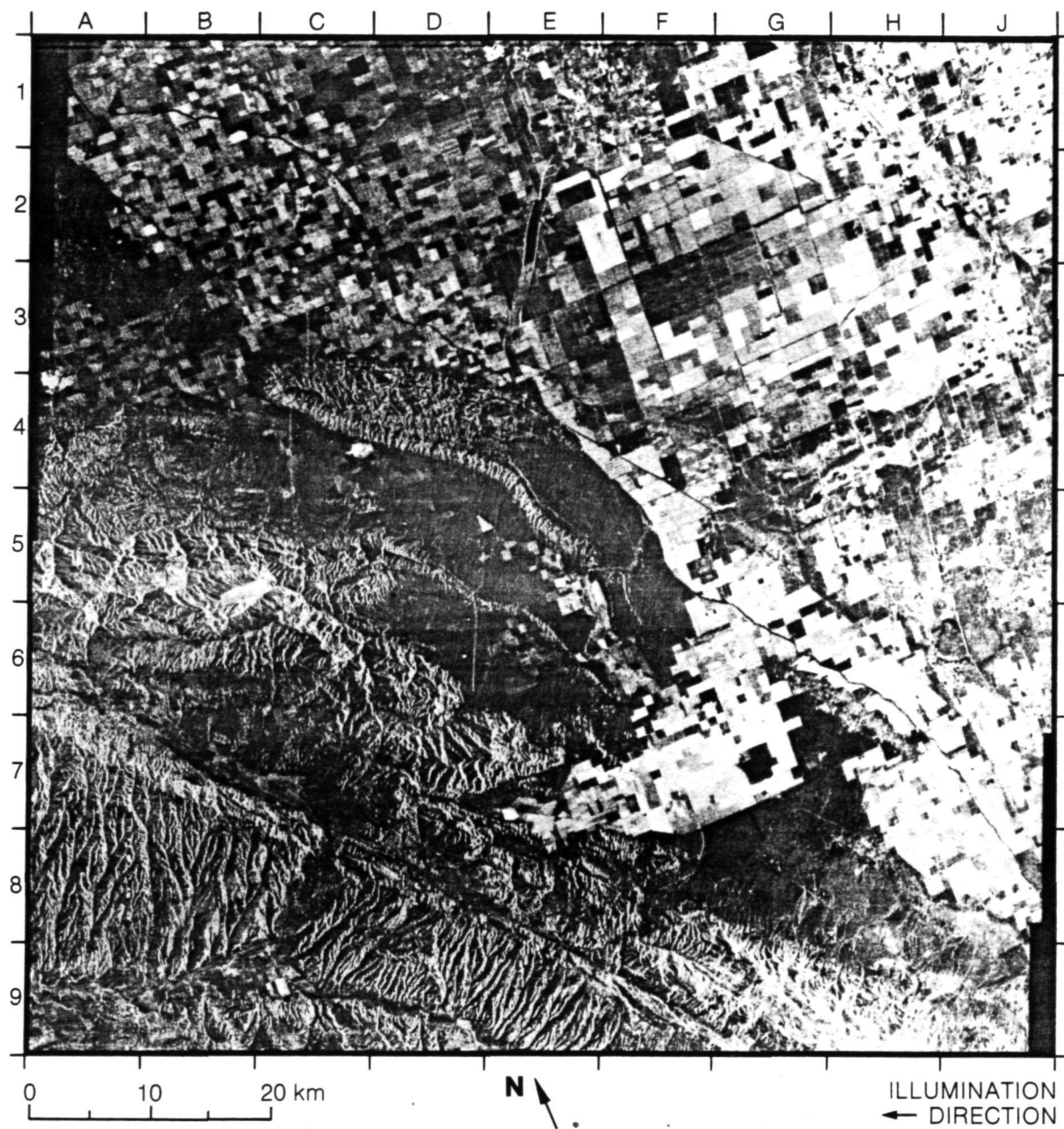
This image covers a portion of the western San Joaquin Valley of California and the foothills of the coast ranges. The San Andreas Fault cuts through the foothills from A6 to G9 on the image. Separated from the foothills by a syncline (downfold) are the anticlinal (upfolded) Kettleman Hills, centered at about E4. The Kettleman Hills are the largest of a series of anticlines that border the
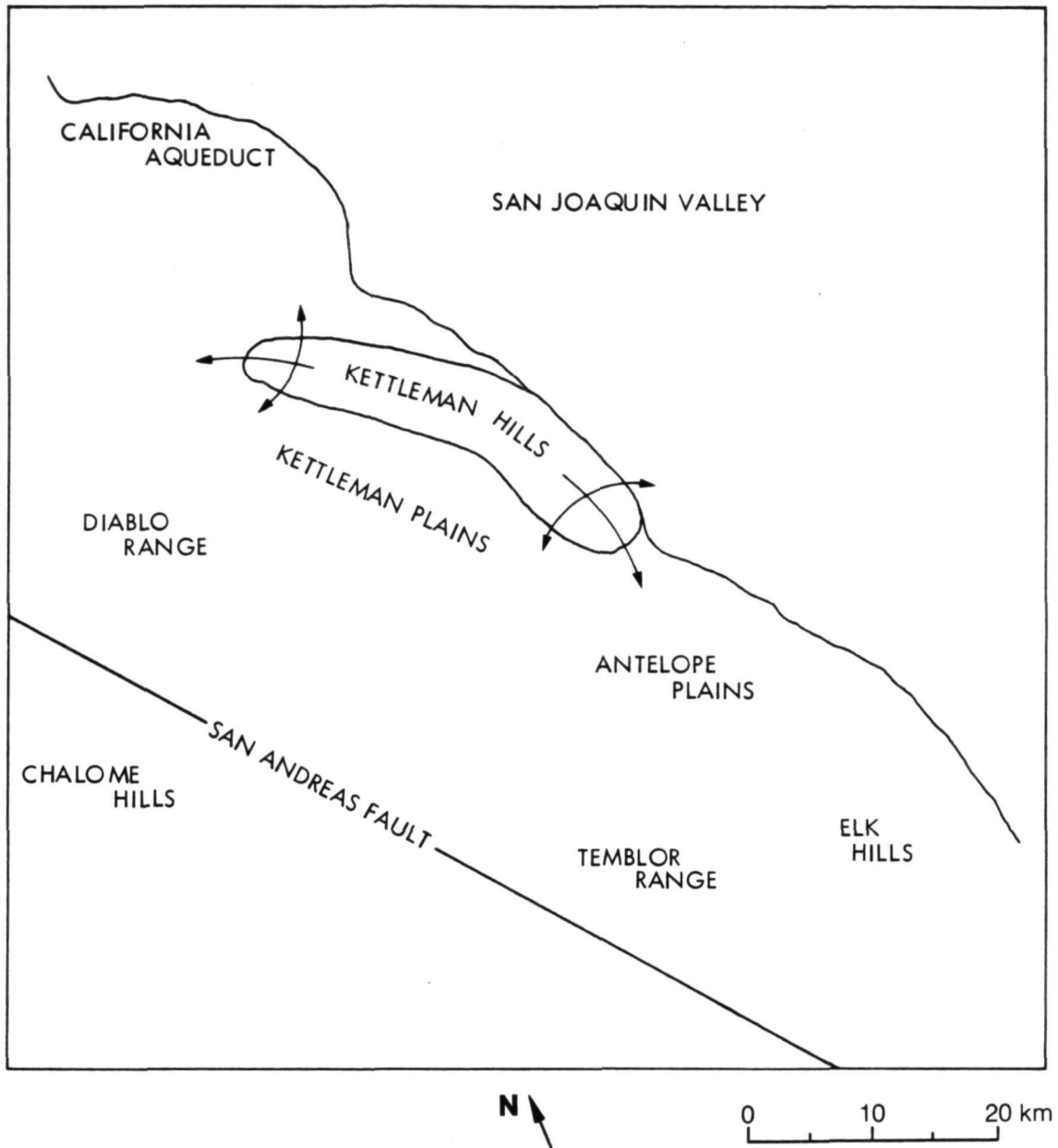
western San Joaquin Valley. These geologic structures form excellent conditions for petroleum reservoirs. This series of anticlines extends from A2 to J8 and includes several major oil fields. The Kettleman Hills are the largest of these.

(Seasat image from Rev. 574.)

7. San Rafael Swell, Utah

ILLUMINATION DIRECTION →

N

0   10   20 km

The San Rafael Swell in Utah is a doubly plunging breached anticline, about 100 kilometers long and 50 kilometers wide. The axis of the structure trends approximately N 30° E. The exposed sedimentary rocks in the area consist primarily of sandstones and shales with lesser amounts of limestone and conglomerate. They range in age from Pennsylvanian to Jurassic. Economically significant deposits of uranium occur in the Upper Triassic Chinle Formation. The general structure and form of the swell is clear on both the Seasat image (above) and the facing Landsat image.

The gray levels in the Landsat image vary with surface composition, while the gray levels in the Seasat image vary with surface roughness and slope.
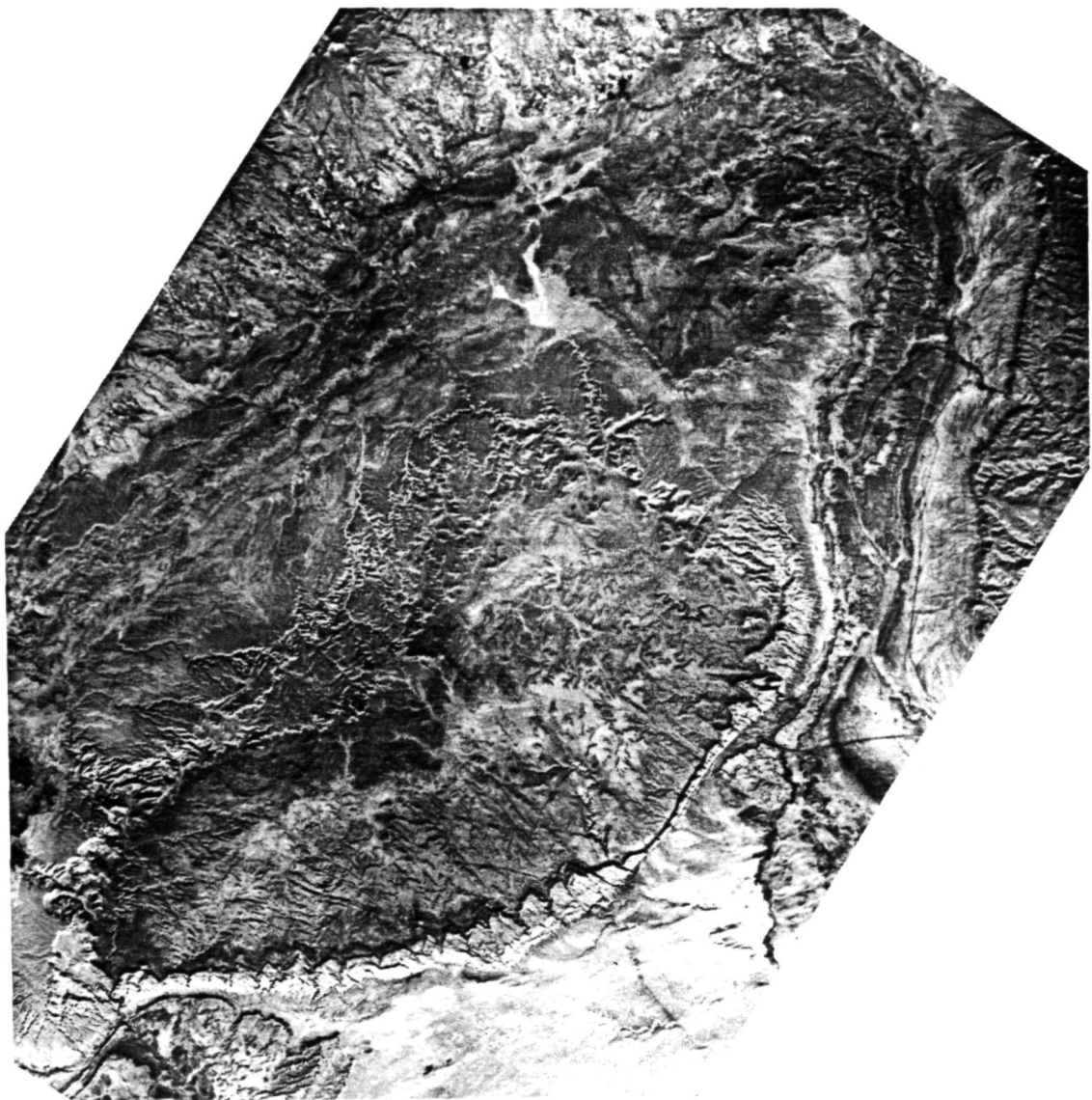
↑ N   0   10   20 km

Thus the two images give different types of information. Because of the radar's
sensitivity to slope, the Seasat image enhances linear topographic features
which the Landsat image does not. A good example can be seen extending
from about D6 to E8 in the Seasat image. In general, smooth surfaces underlain
by shales are darker than surrounding areas, and the rougher sandstone sur-
faces appear brighter on the Seasat image.

(Seasat image from Rev. 853; Landsat scene ID: 1068-17364.)

(ii) Fault Structures

29

8. San Andreas Fault, Southern California

ILLUMINATION DIRECTION →   N   0   10   20 km
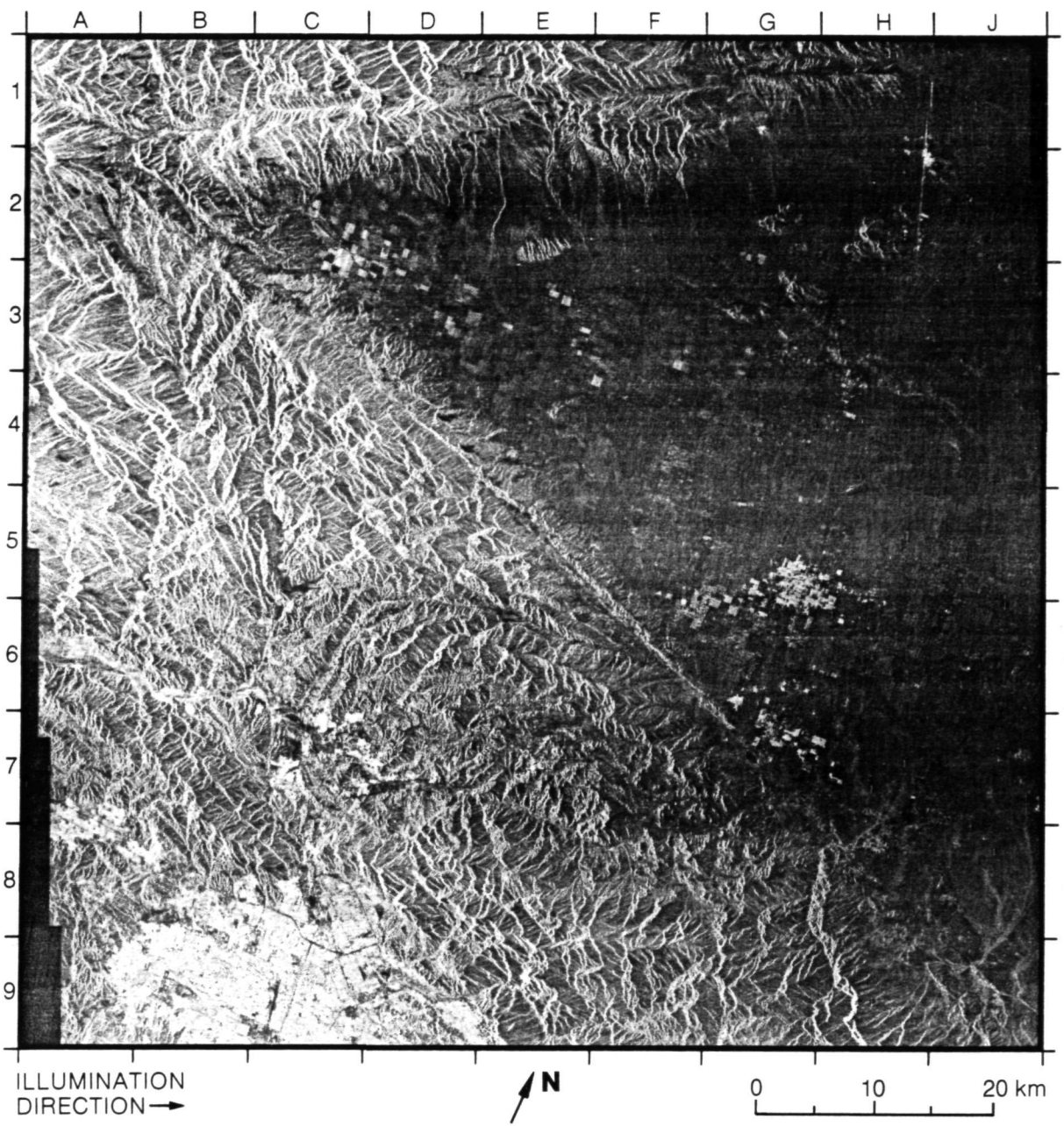
The San Andreas Fault extends across this image from A1 to J9, separating the Antelope Valley and Mojave Desert to the northeast from the San Gabriel Mountains and Angeles Forest to the southwest. The fault forms a pronounced linear scarp at the base of which occur numerous alluvial fans, such as the one in J8. Toward the top of the image, the San Andreas Fault is intersected by the Garlock Fault, which extends from B1 to J1, and marks the boundary between the Mojave Desert and the Tehachapi Mountains to the north. Part of the densely populated San Fernando Valley appears at the lower left of the image.

The relatively smooth and somewhat level surface of the Mojave Desert produces little radar backscatter and appears dark on the image. This is notably true for the dry-lake bed (Rosamond Lake) in H4 to J4. The smooth surfaces of major highways and reservoirs in the San Fernando Valley, and the

                    ╱**N**   0   10   20 km
                                              |___|___|___|___|
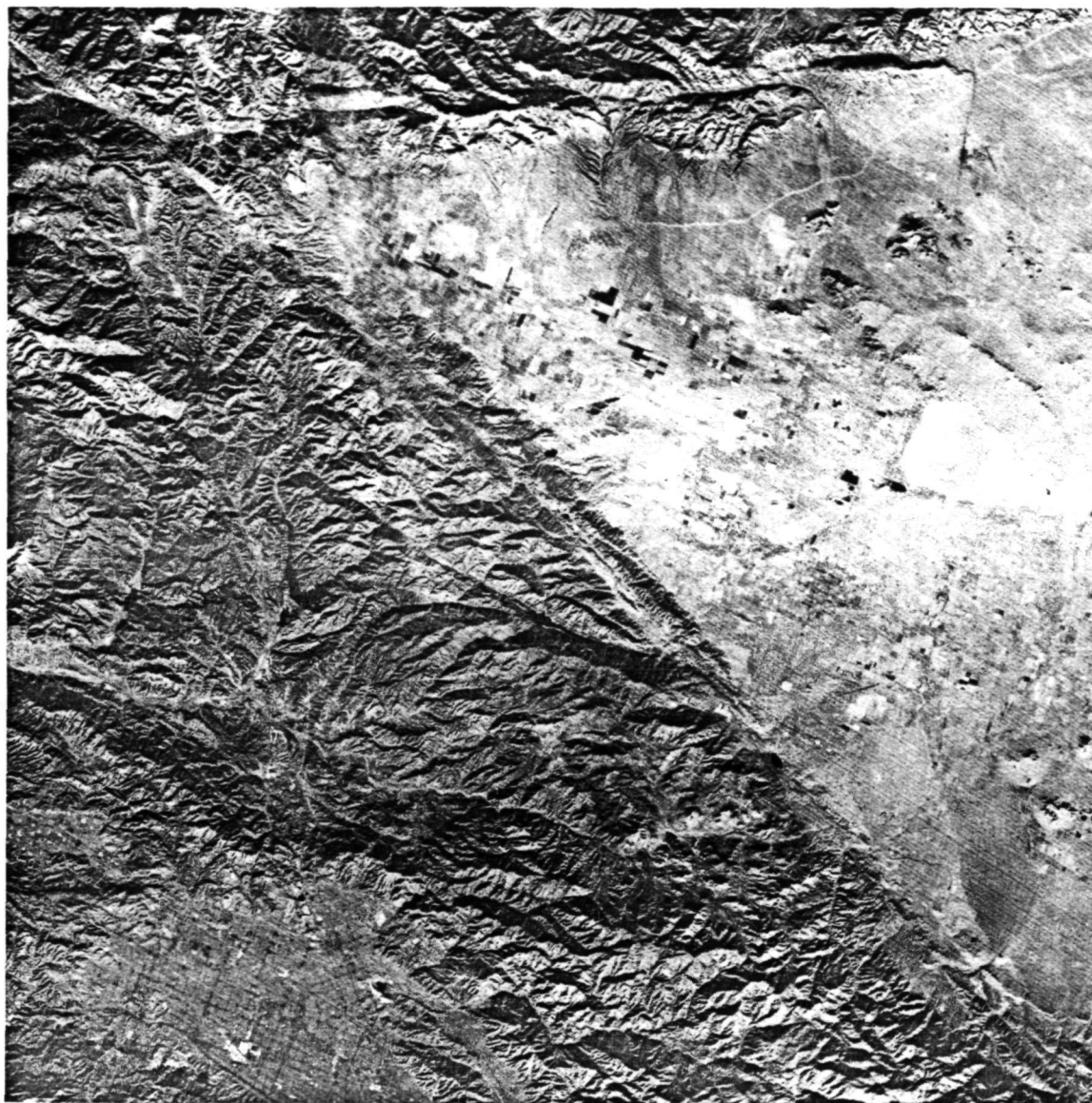
Van Nuys Airport (C9) are likewise dark on the Seasat image. In contrast, the sloping mountain surfaces in the San Gabriel and Tehachapi Mountains that face the radar-illumination direction appear very bright due to radar layover. In addition, the geometric distortion of the terrain obscures the trace of the San Gabriel Fault from B2 to E9.

The Mojave Desert surface is highly reflective in MSS band 7 and is correspondingly bright in this Landsat image. The trace of the San Gabriel Fault from the San Fernando Valley to the junction of the San Andreas/Garlock Faults is more apparent than on the facing Seasat image. Topography is enhanced by shadowing at the low sun-elevation angle.

(Seasat image from Rev. 351; Landsat scene ID: 2698-17371.)

9. Great Glen Fault, Scotland

ILLUMINATION DIRECTION →

↗N

0   10   20 km

This radar image depicts the rugged terrain of the Scottish Highlands. The highest point in the British Isles, Ben Nevis (1343 meters) in the Grampian Mountains, is shown here at the lower right corner of C8. The Great Glen Fault (A9 to J5) separates the Grampian Mountains from the Northern Highlands to the north and west. This is a left-lateral strike-slip fault that was active in Paleozoic time. The Great Glen (Glen Mor, H6 to J5) lies along the fault and contains Loch Ness—home of the fabled monster of the same name.
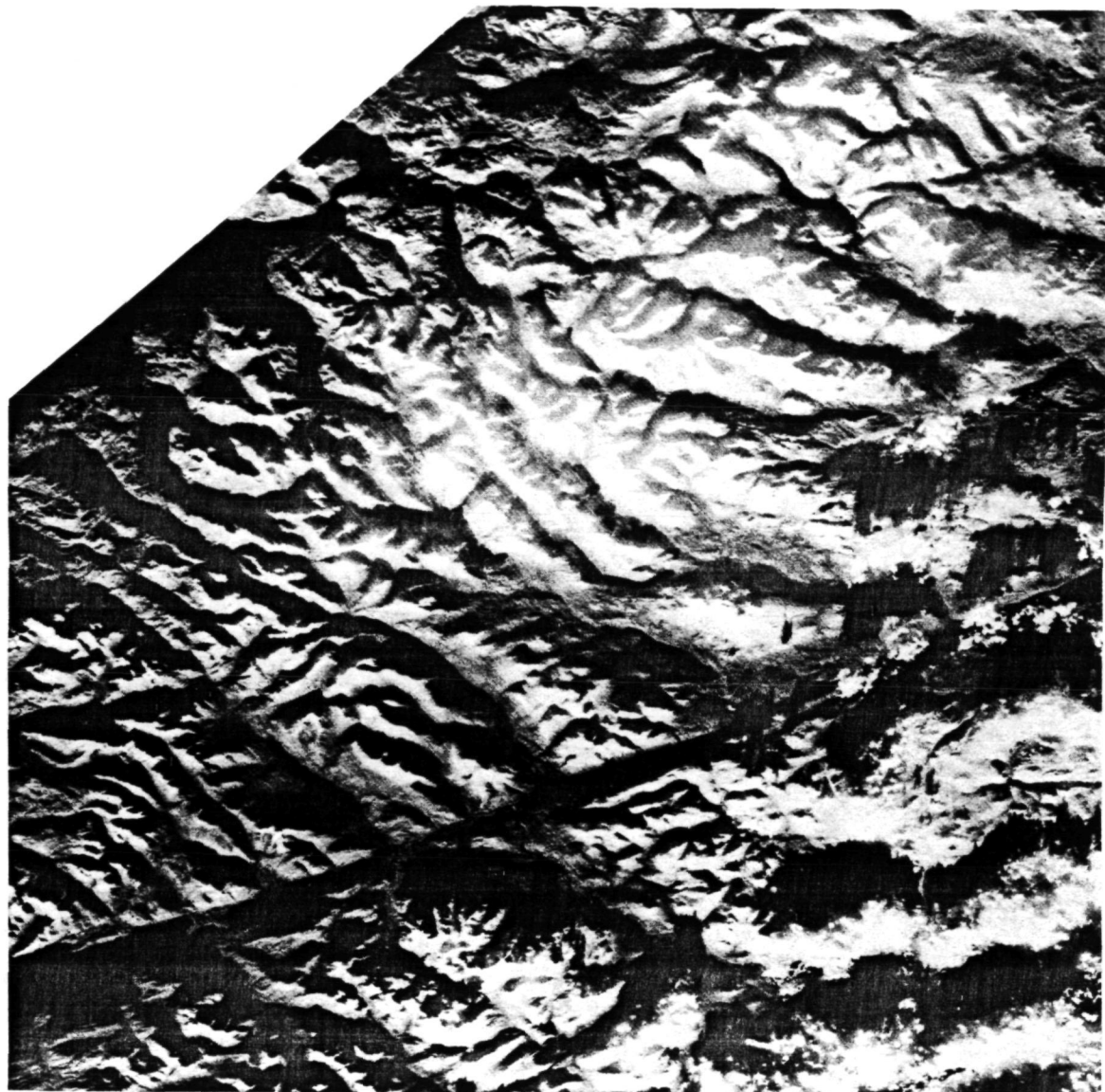
The Landsat scene above, which was acquired in winter, shows snow on the Highlands. Topography is partially obscured by shadowing due to the very low sun-elevation angle. Clouds obscure the scene, notably over Ben Nevis and Loch Ness.

(Seasat image from Rev. 719; Landsat scene ID: 2373-10414.)

10. Pine Mountain Thrust Fault, Tennessee-Kentucky-Virginia

ILLUMINATION DIRECTION→

↑N

0   10   20 km
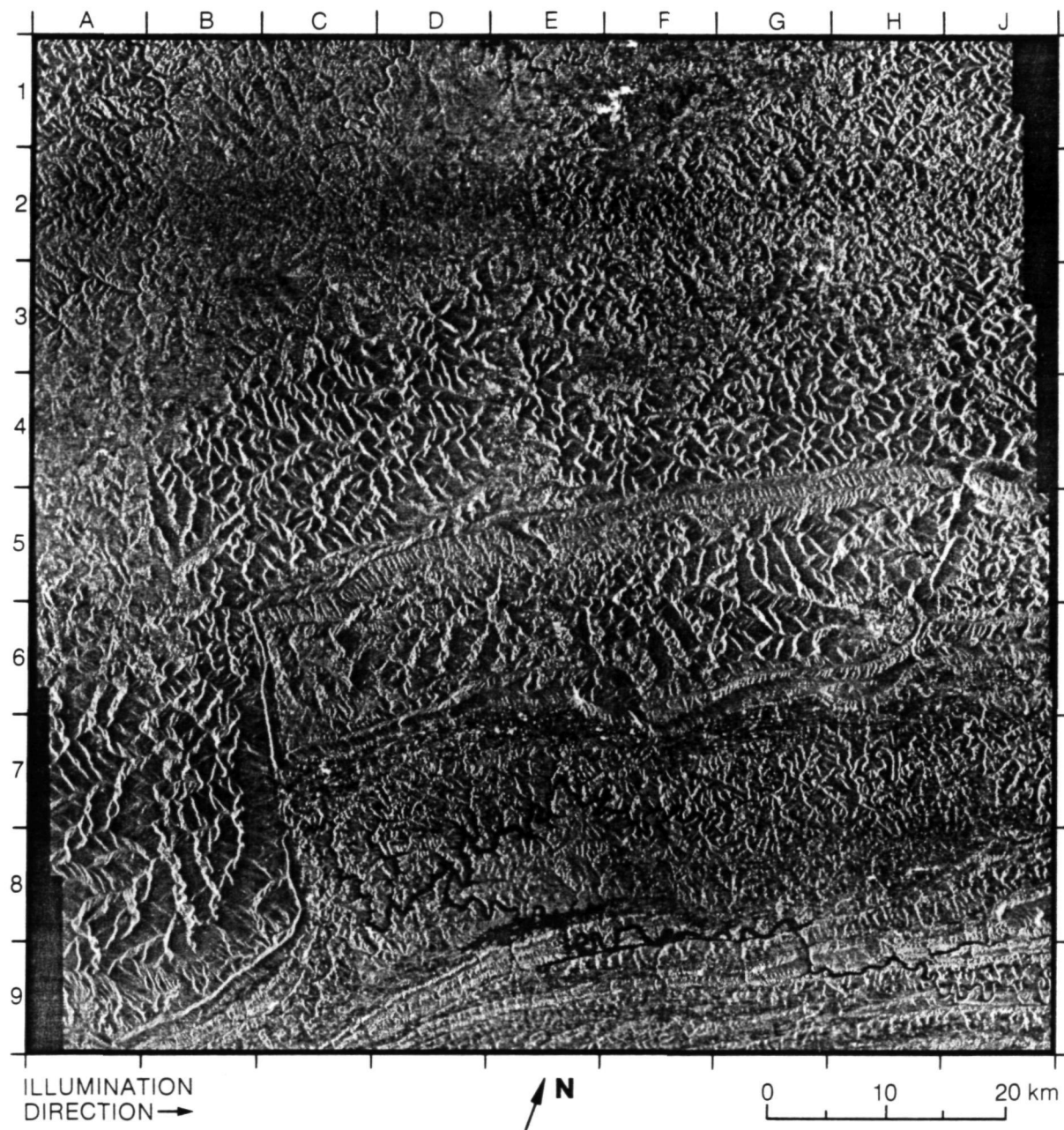
The Pine Mountain Thrust Fault (B5 to J4) marks the separation between the Cumberland Plateau to the north, and the Valley and Ridge Province to the south. Steep slopes that face the radar-illumination beam appear bright. Topography is enhanced by radar sensitivity to change of slope. The slopes are densely forested and covered by a mixed deciduous- and coniferous-leaf

<N
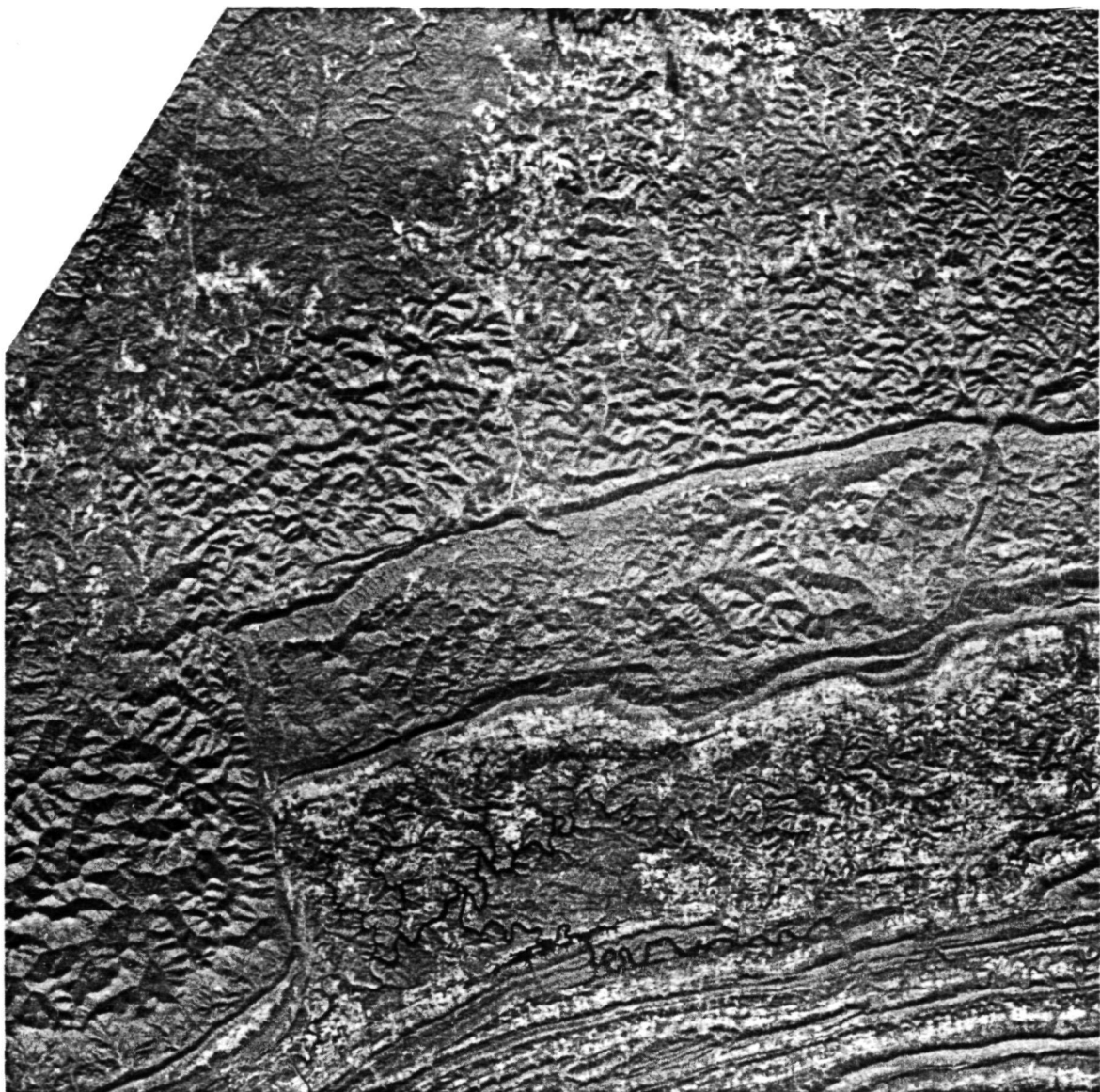
| 0 | 10 | 20 km |

canopy. Extensive lineaments denote fault traces, notably the Jacksboro Fault (B6 to C8), and the Rocky Face Fault (J4 to H5). The City of Middlesboro, Kentucky, is at H6. Reservoirs of the Tennessee Valley Authority appear black (notably in D8 to G8).

(Seasat image from Rev. 407; Landsat scene ID: 1858-15303.)

(iii) Sand Dunes

11. Algodones Dunes, California

ILLUMINATION
DIRECTION →

↑ N

0   10   20 km
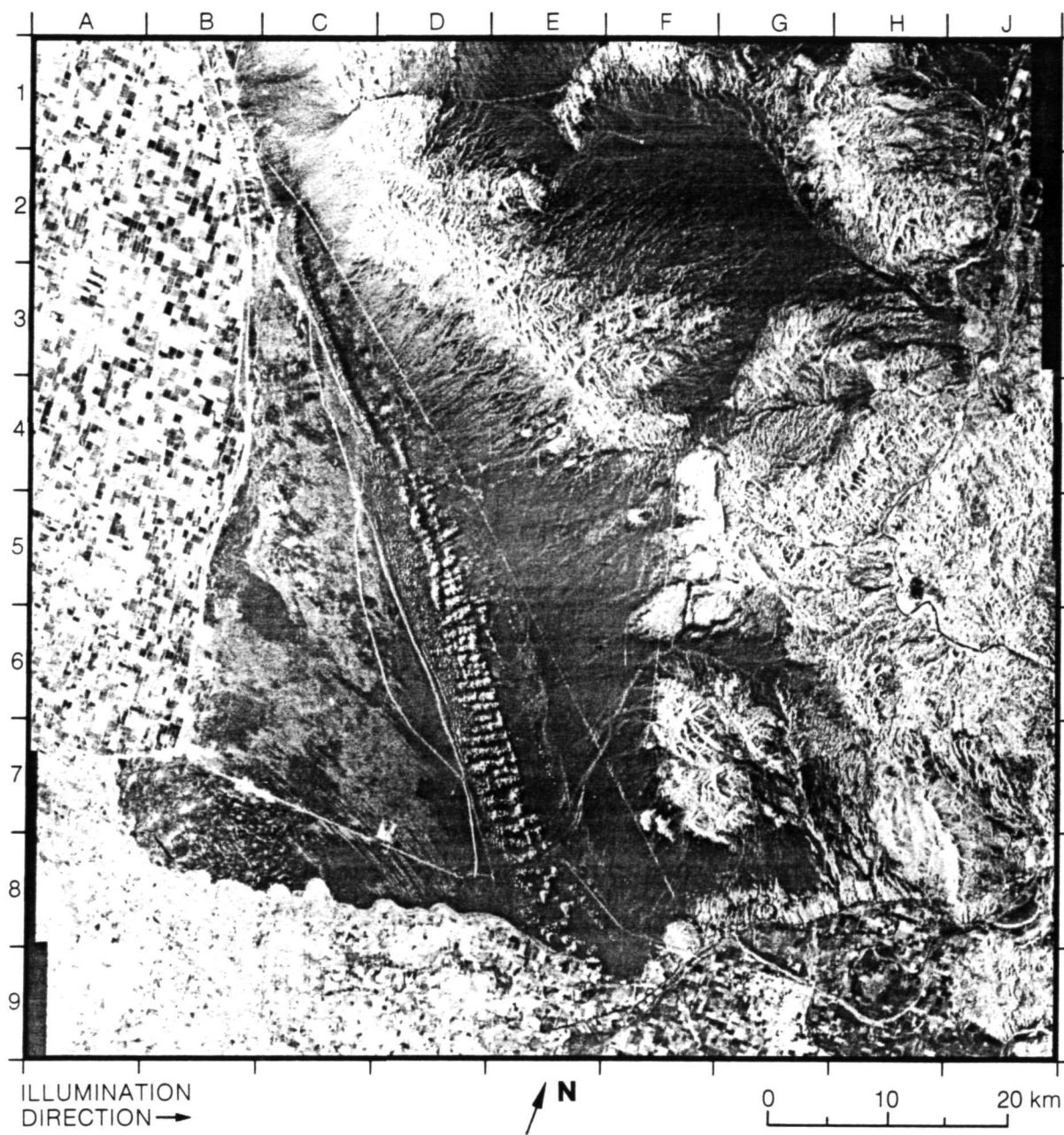
The Algodones Dune Field in southeastern California is about 60 kilometers long and 10 kilometers wide, and displays a variety of aeolian features. The features are described in reference to the Seasat image (above), but each feature should be examined also on the Landsat image (right).

The narrow northern end of the dunes is at C2 on the Seasat image. The dunes gradually widen toward D4 where they abruptly become considerably wider. The eastern slope of the dunes from D5 to F8 is dark on the Seasat image because it slopes away from the radar illumination and produces low backscatter. The same feature is bright in the Landsat image because of the direction of sun illumination. The central-to-southern part of the dune field is characterized by long, narrow dunes on the west side, complex coalesced

N

0   10   20 km
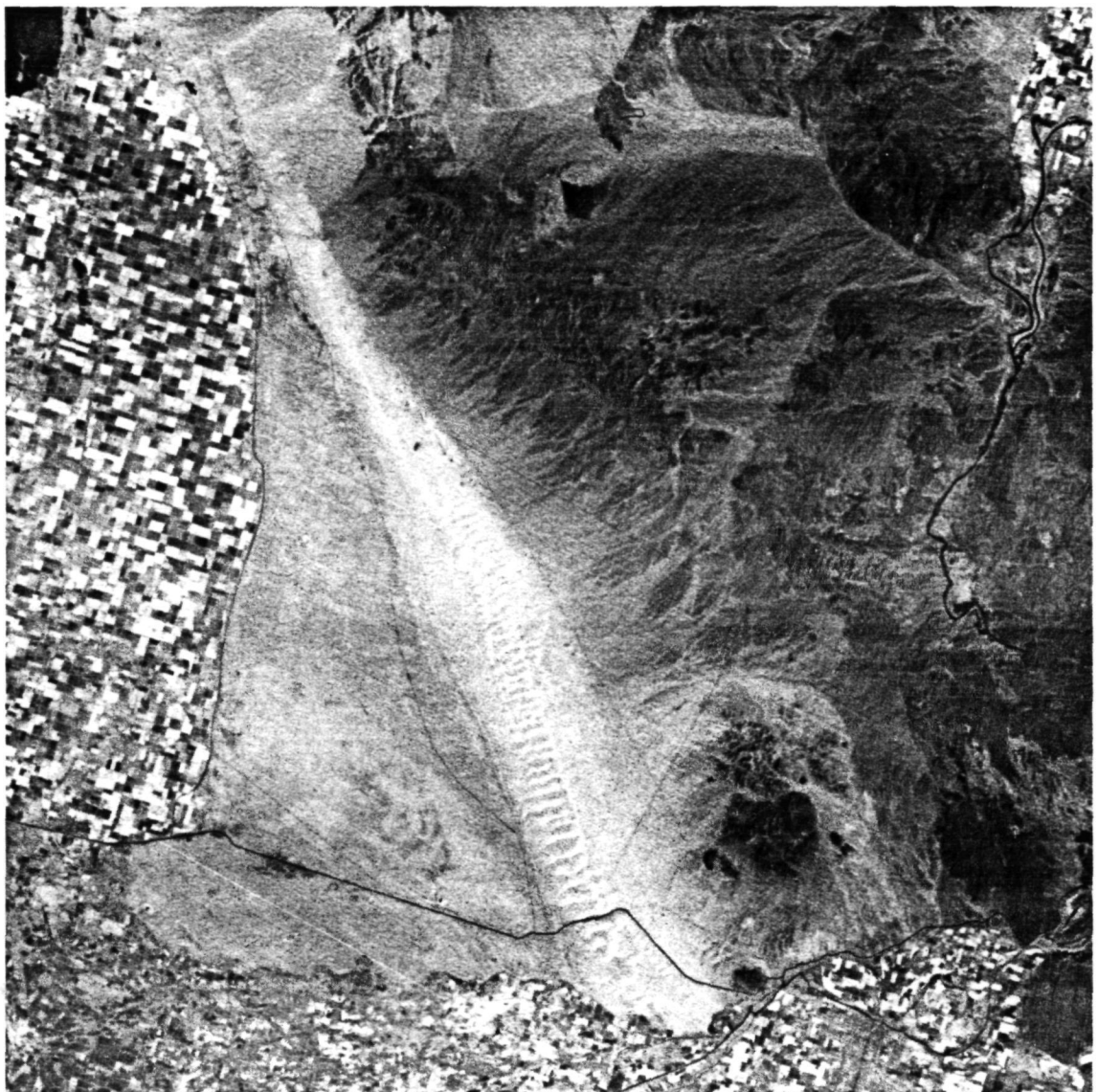
domical dunes in the west center, and giant crescentic dunes from the center southward. The crescentic dunes are up to 60 meters high. The southern terminus of the dune field is at F8. Sand sheets and stringers occur west of the dunes from about C3 to C8.

Other noteworthy features are the canals and a corner of the Salton Sea at A1, which appear bright on the Seasat image and dark on the Landsat image. The checkered rectangular pattern at the left side of both images represents agricultural fields. The abrupt change in this pattern at A7 marks the U.S.-Mexico border.

(Seasat image from Rev. 1140; Landsat scene ID: 5473-16551.)

12. Sonora Dunes, Sonora, Mexico

ILLUMINATION
DIRECTION →

N

0   10   20 km
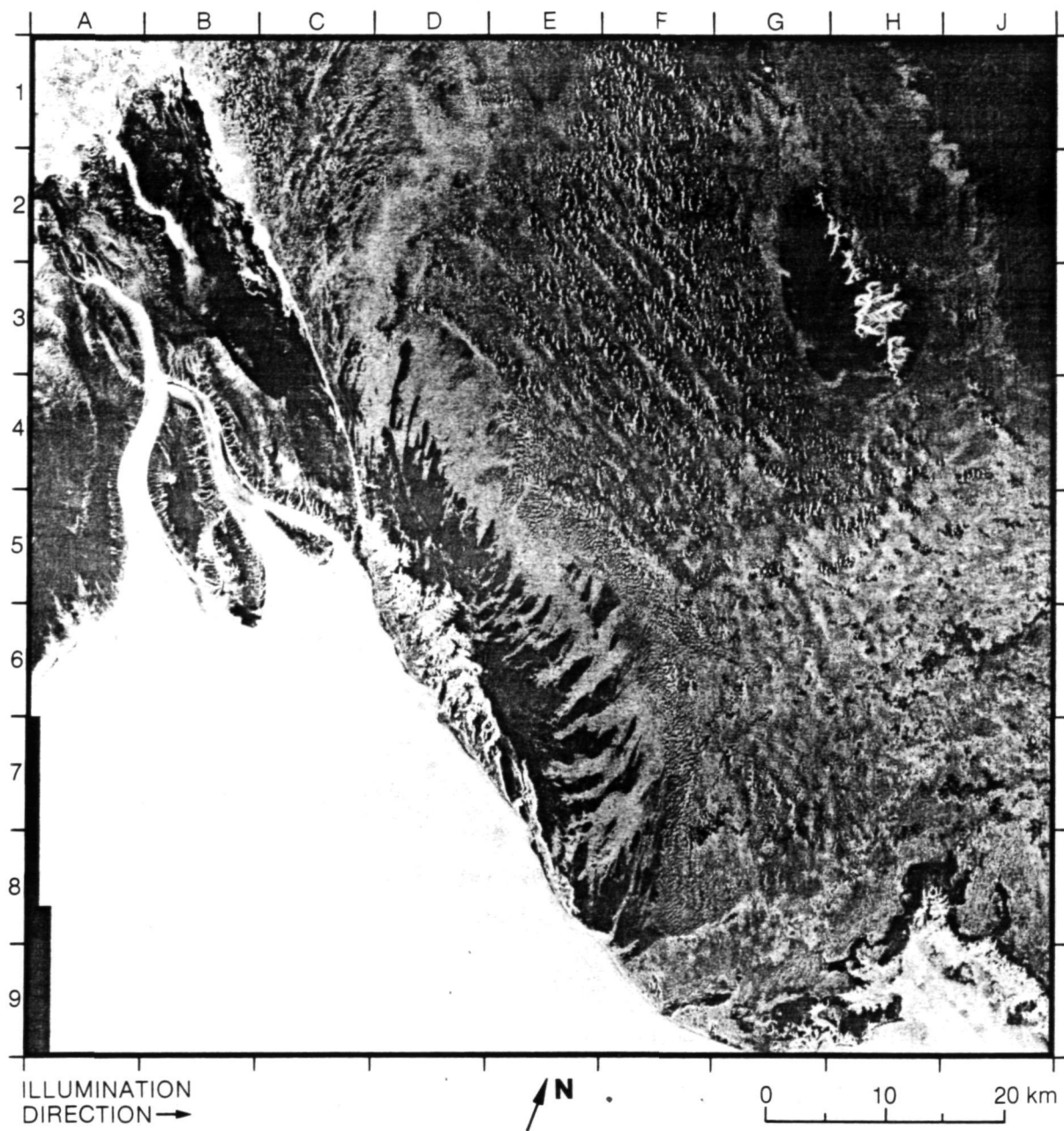
The Sonora Dunes, situated east of the Colorado River Delta and adjacent
to the Gulf of California, are the largest active dune field in North America.
Major dune features on the Seasat image (above) and on the facing Landsat
RBV (return beam vidicon) image are star dunes that occur in chains in the
center of the dune field from about F1 to F5, and surrounding crescentic dunes
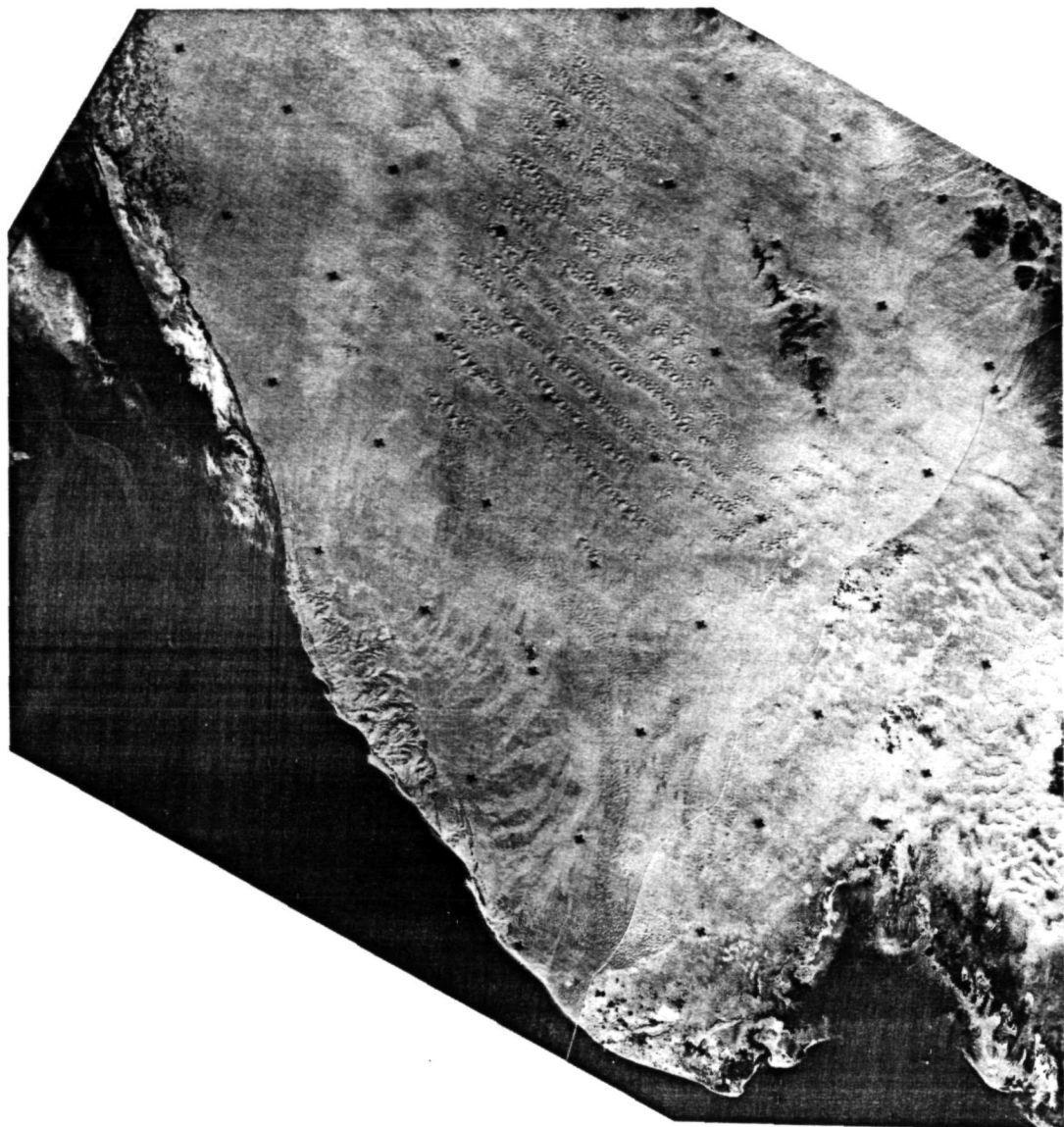
↑N   0   10   20 km

and sand sheets. Tonal variations in the aeolian features are similar on both the Seasat and the Landsat images. The regularly spaced, small black crosses on the RBV image are fiducial markers.

(Seasat image from Rev. 1140; Landsat RBV composite scene ID: 30214-17343 B and 30231-17285 A.)

(iv) Volcanic Terrain

43

13. Medicine Lake Highland, California

0   10   20 km   N   ILLUMINATION
                                      ←DIRECTION

This image shows a variety of volcanic features in Northern California. Most prominent is Mount Shasta at location C8. The parasitic cone Shastina and volcanic flows on the northwest side of Mount Shasta show clearly. The Medicine Lake Highland volcanic area (G4) is a broad shield volcano with a summit collapsed caldera rimmed by small volcanoes (refer to sketch map). There are numerous small cinder cones and domes on the slopes of the shield volcano. Recent flank eruptions of basalt include the Callahan Lava Flow (F3)

Features
Doubled by
STC Change

TIMBER
MTN

CALLAHAN
LAVA FLOW

GLASS MTN
AND FLOW

CALDERA
RIM

MEDICINE LAKE

BURNT
LAVA
FLOW

Power
Line

Faults

Faults

BEAR MTN

TIMBER
CRATER
O

MOUNT
SHASTA

N

0   10   20 km
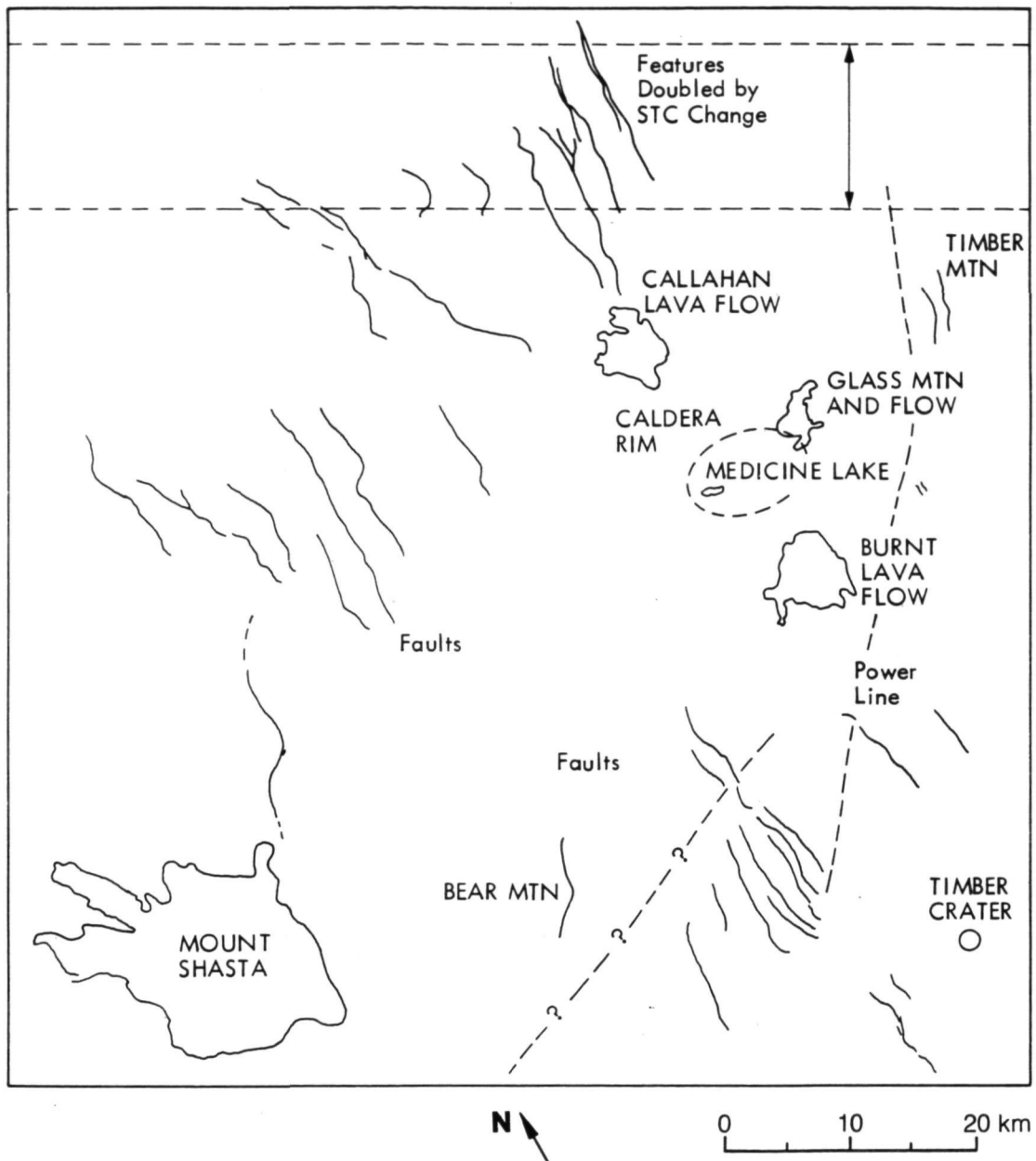
and the Burnt Lava Flow (G5). Glass Mountain and the flow are formed from a recent obsidian eruption at the caldera rim (G4). These features and numerous topographic scarps related to faulting are indicated on the geologic sketch map above. Scarps with only about 2 meters relief are visible on the Seasat image. The doubling of bright features in the northern part of the image is due to an STC change during the time that the image was acquired.

(Seasat image from Rev. 1406.)

14. Newberry Volcano, Oregon

ILLUMINATION DIRECTION→   ↗ N   0   10   20 km
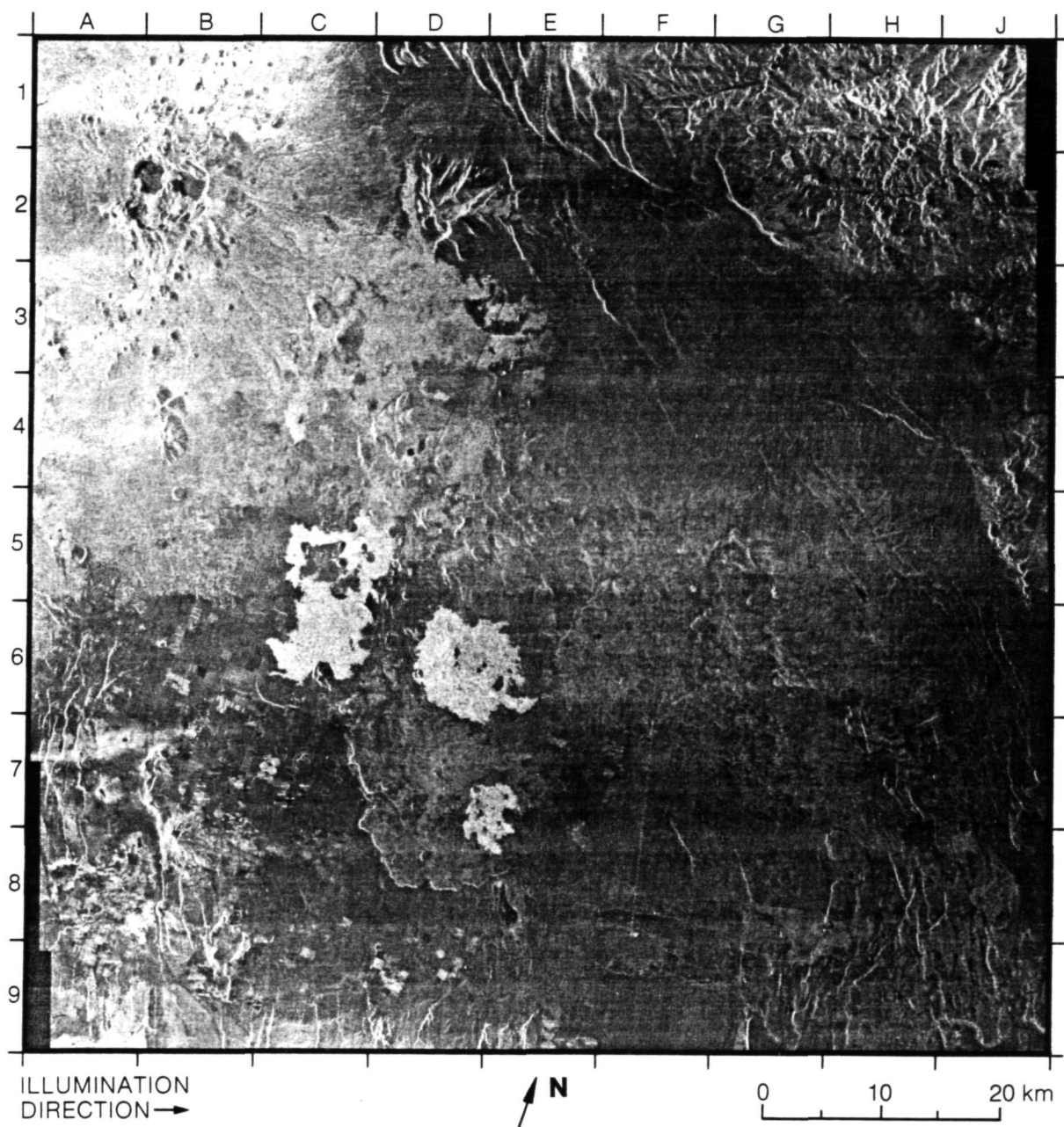
Newberry Volcano (B2) is a large shield volcano whose caldera is occupied by two scenic lakes (see sketch map). The cinder cones on the volcano flanks are most numerous on the north and south slopes. The overall bright tone of the volcano is due to backscatter from the forest canopy. The lower terrain to the east receives much less rain and the geology is less obscured by vegetation. Recent basalt flows (Q1b on the geologic sketch map) are much brighter

Map labels:

PAULINA LAKE

CALDERA RIM

EAST LAKE

NEWBERRY VOLCANO

BROTHERS FAULT ZONE

Qlb

Qlb

Qlb

FORT ROCK VALLEY

Qb

Qlb

Faults

CHRISTMAS LAKE VALLEY

N

0   10   20 km
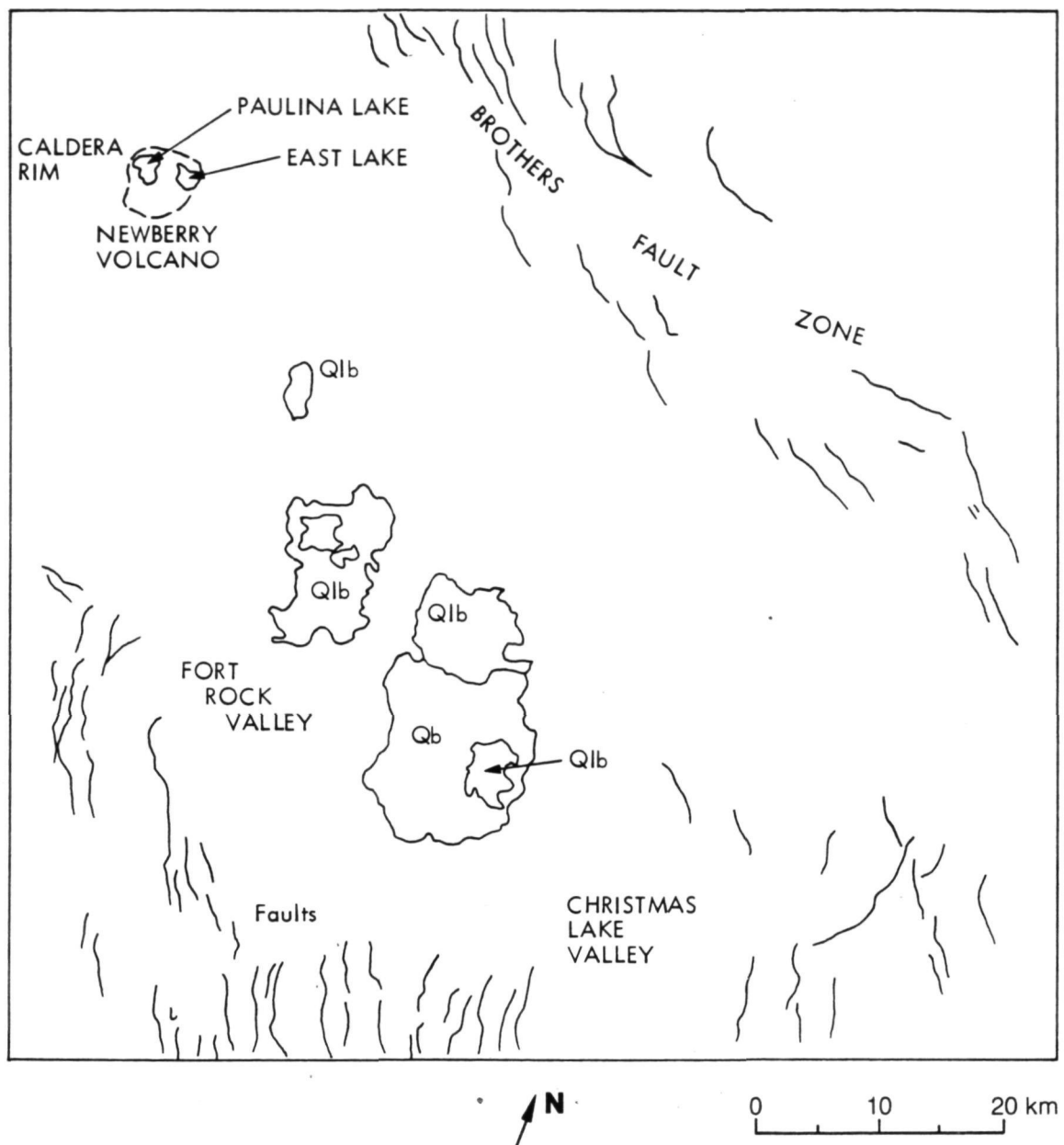
than the surrounding terrain due to their roughness. Older, more eroded basalts are smoother and hence darker, such as those at E6 to E7 (Qb on the map). Two major structural trends indicated by numerous fault scarps intersect just north of the volcano. The north trending faults are obscured by the volcanic outpourings from Newberry Volcano.

(Seasat image from Rev. 681.)

ILLUMINATION
DIRECTION ➞

↗ **N**

0   10   20 km
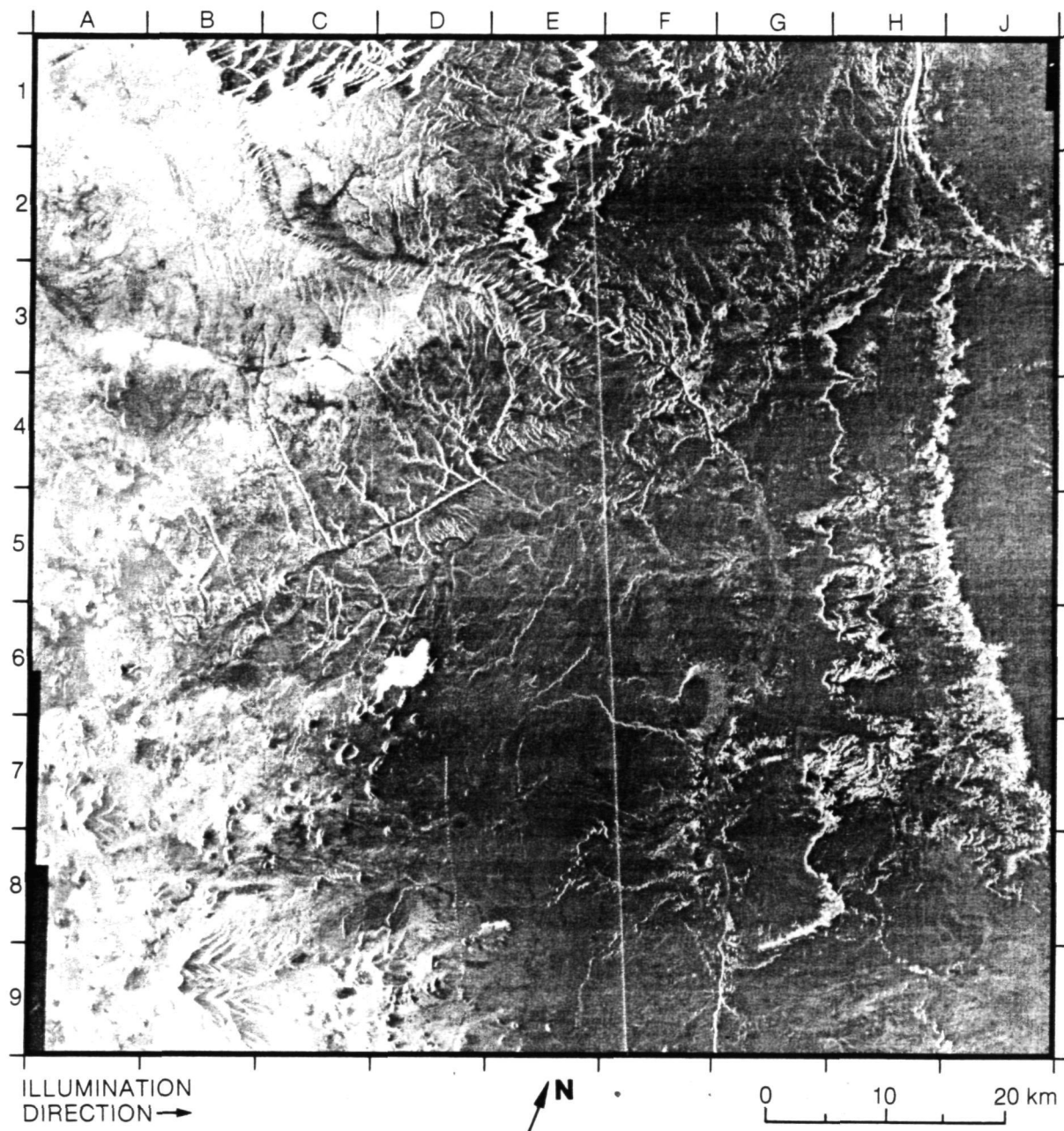
South of the Grand Canyon (B1 and C1) lies the Coconino Plateau. It forms
the southern half of the great uplift known as the Colorado Plateau. Its eastern
boundary (H1 to H8 and J1 to J8) is the Echo Cliffs monocline, east of which lies
the Kaibito Plateau (J2). The major drainage visible at E1 and E2 is the Little
Colorado River. Structural features in the scene include the sinuous Grandview

N

0   10   20 km
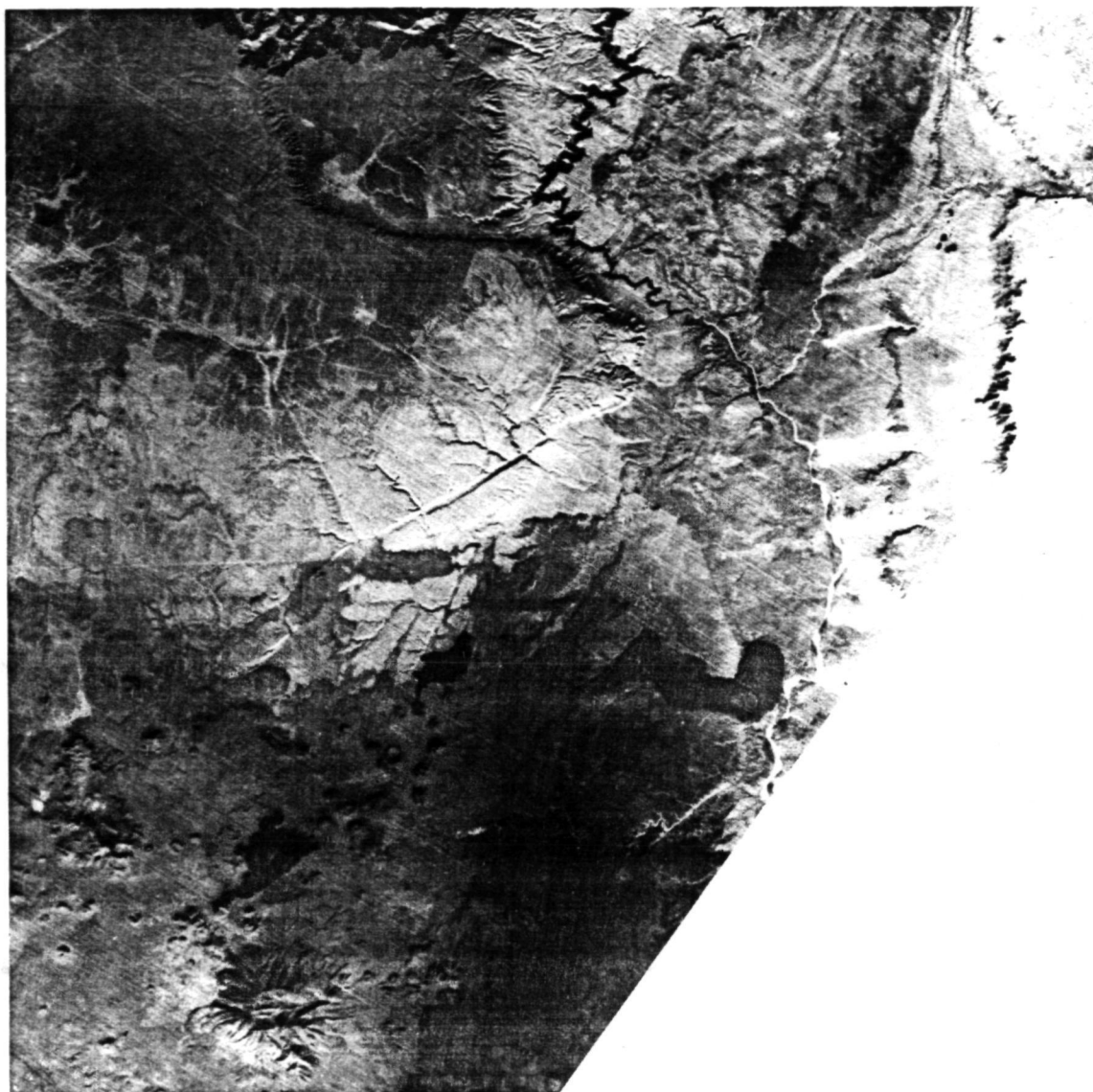
monocline (C2 and D3) and the well-defined Mesa Butte graben (C4 and D4 to C5 and D5). Major volcanic features include the young SP flow (D6) and the San Francisco Peaks Province, including the high peaks near Mt. Humphreys (B9) and the numerous cinder cones including Sunset Crater (D9).
(Seasat image from Rev. 322; Landsat scene ID: E-1464-17354.)

16. Askja Caldera, Iceland

ILLUMINATION
DIRECTION→

N

0   10   20 km
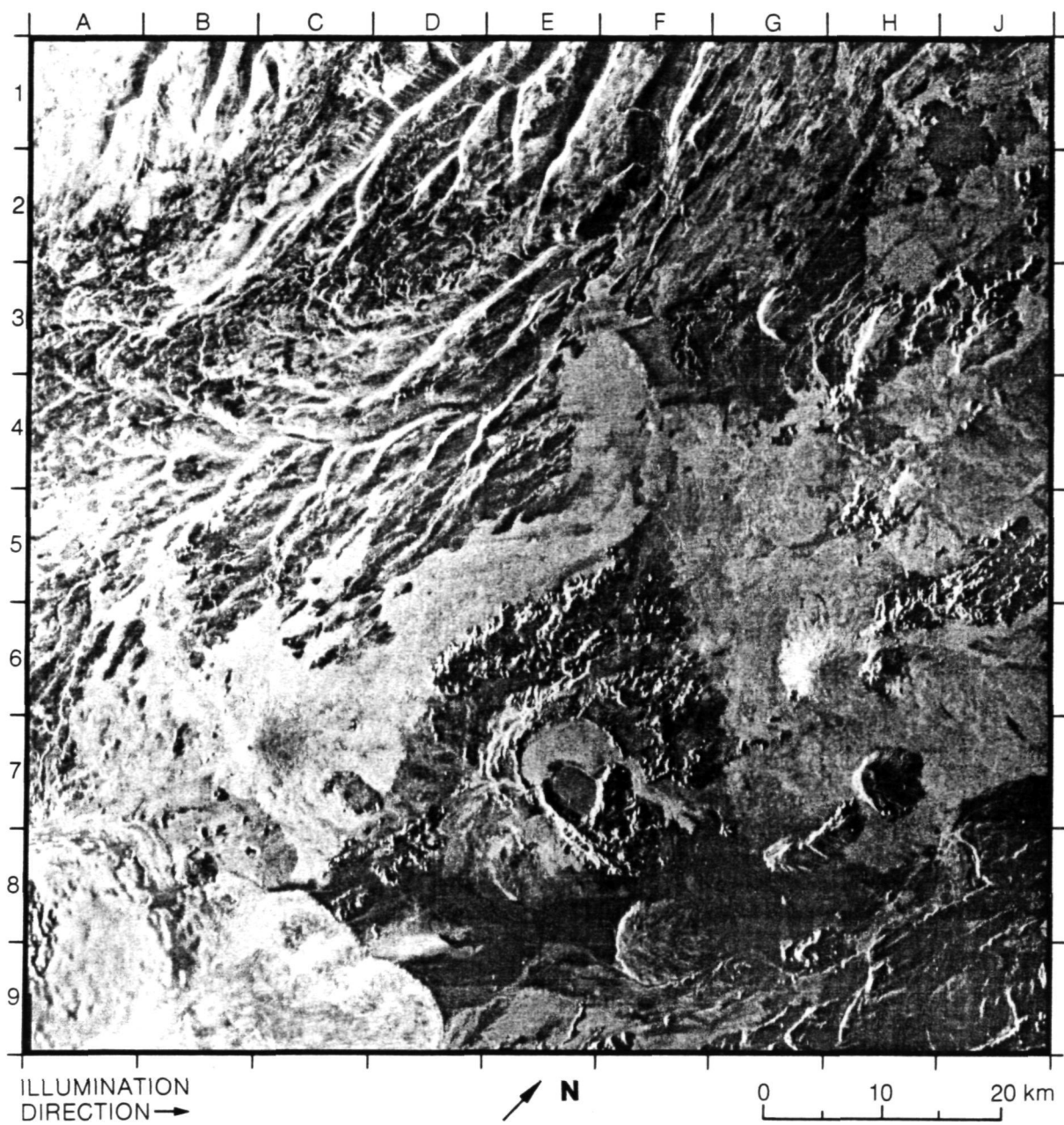
This image of north-central Iceland covers part of the largest emergent section of the mid-Atlantic rift zone. The area is characterized by shield volcanoes and active central and fissure eruptions aligned along the northeast-southwest trending axial rift. The lake (Myvatn) located at H1 and H2 to J1 and J2 is surrounded predominately by aa lavas that emanated from the Threngslaborgir-Lúdentsborgir crater row. This crater row or fissure is the northeast-southwest trending linear feature at J2, which lies between two large tephra rings: Lúdent to the east, and Hverfjall to the west.

Askja Caldera (E7) is an example of a central eruption. An explosive rhyolitic eruption within this caldera in 1875 resulted in the formation of a second caldera, which is now occupied by Lake Öskjuvatn. The most recent
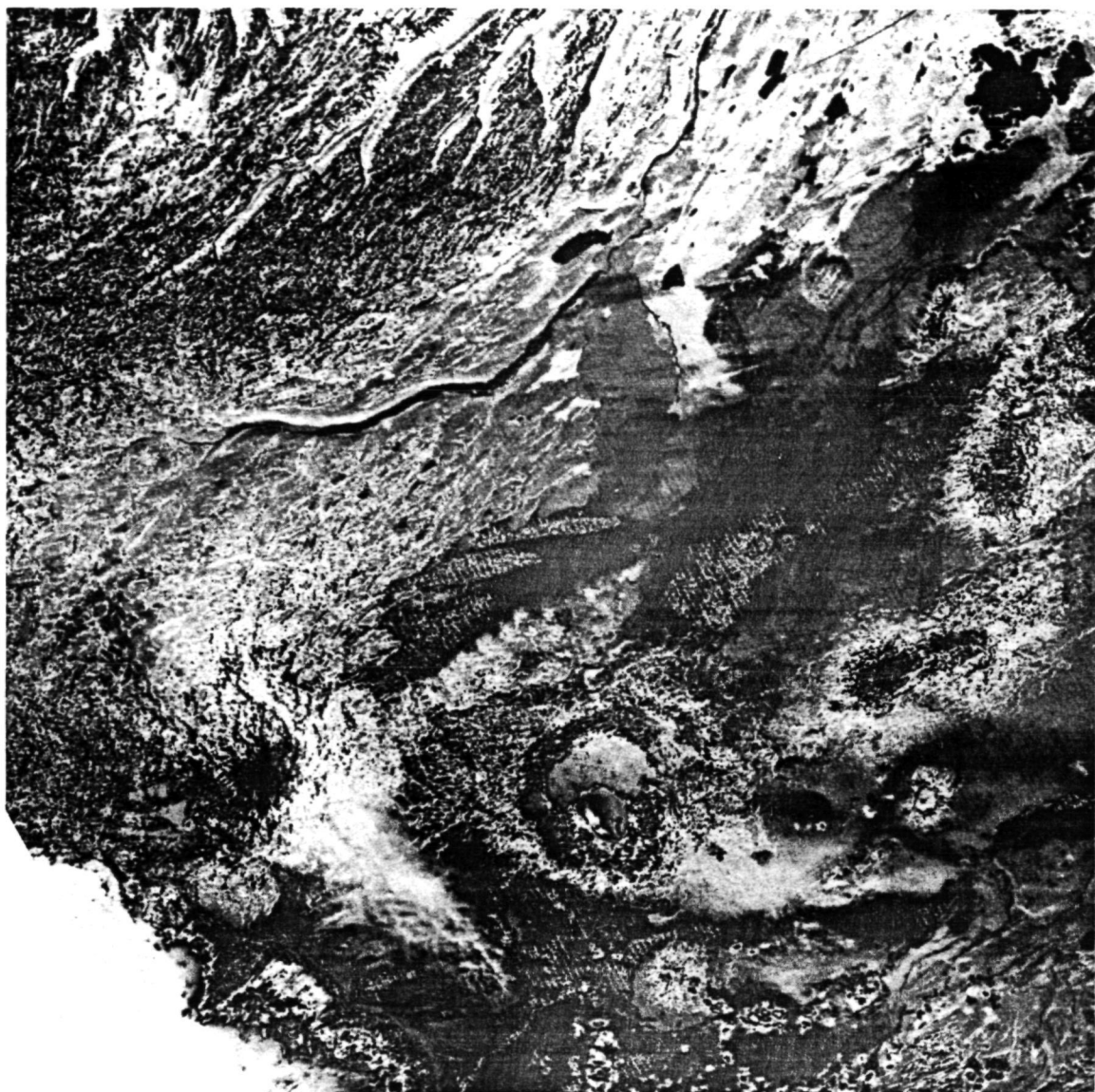
/ N   0   10   20 km

eruption in this area was in 1961. The lavas, which can been seen at F7, were a combination of aa and pahoehoe. Trölladyngja (B7) is an example of a shield volcano. The Frambruni lava flow, which erupted from Trölladyngja, can be traced northward to E3.

There are also some unusual volcanic landforms in this image such as Sellandafjall (G3), Bláfjall (H3), and Herdubreid (H7). These so-called table mountains resulted from volcanic eruptions under glaciers or icesheets such as Vatnajökull (A,B,C,-8,9).

(The caption is by courtesy of Diane Evans, University of Washington, Seattle, Washington.)

(Seasat image from Rev. 719; Landsat scene ID: 2494-11503.)

17. Unimak Island, Alaska

0   10   20 km

N

ILLUMINATION
←DIRECTION
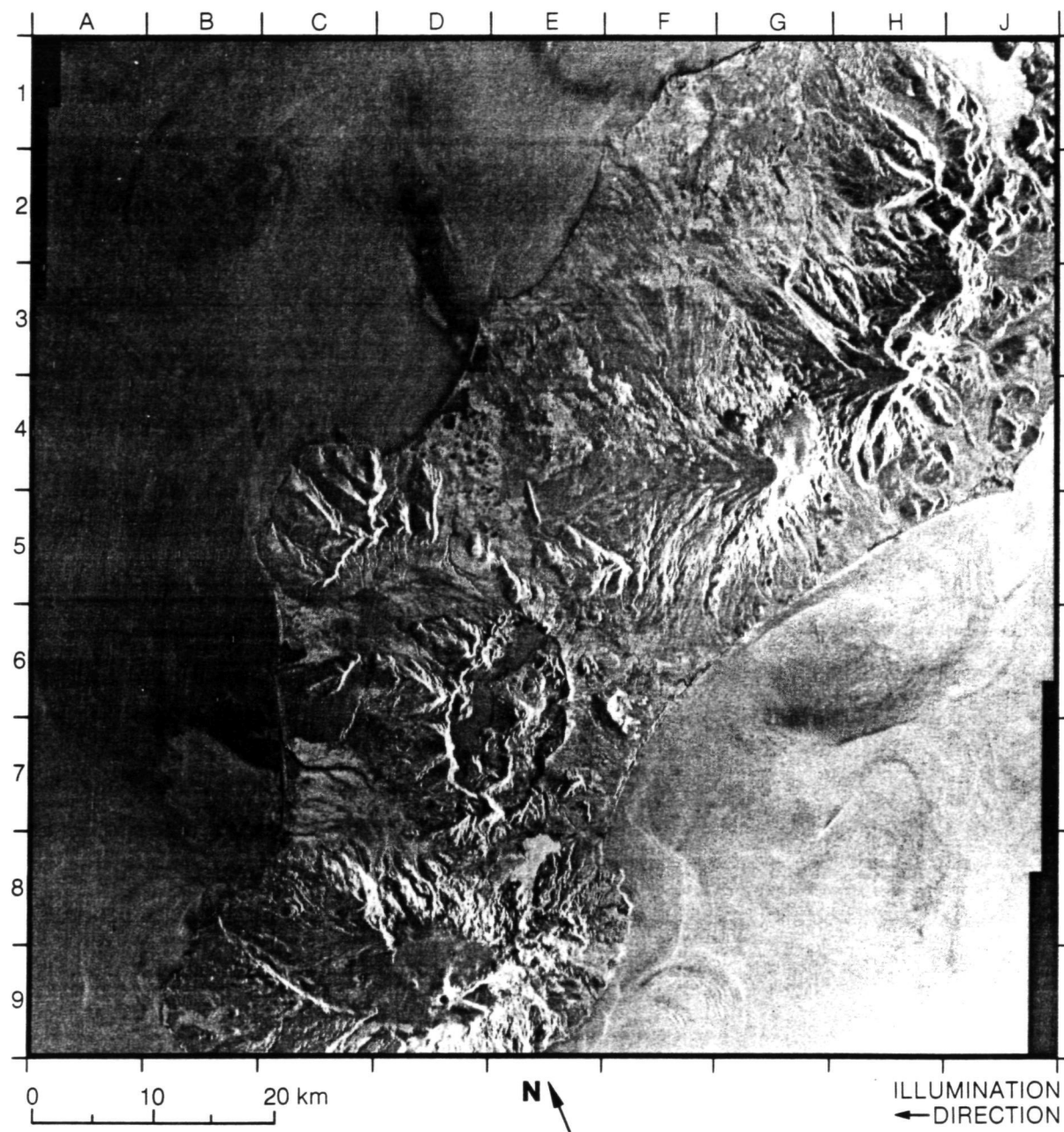
Unimak Island lies in the transition between the continental Alaska Peninsula and the Aleutian island arc. Surface geologic units are dominantly

Alluvial
Plain

ROUNDTOP
MOUNTAIN

Flows?

TUGAMAK
RANGE

ISANOTSKI
PEAKS

SHISHALDIN
VOLCANO

FISHER
CALDERA

FARIS PEAK

WESTDAHL
PEAK

N

0   10   20 km
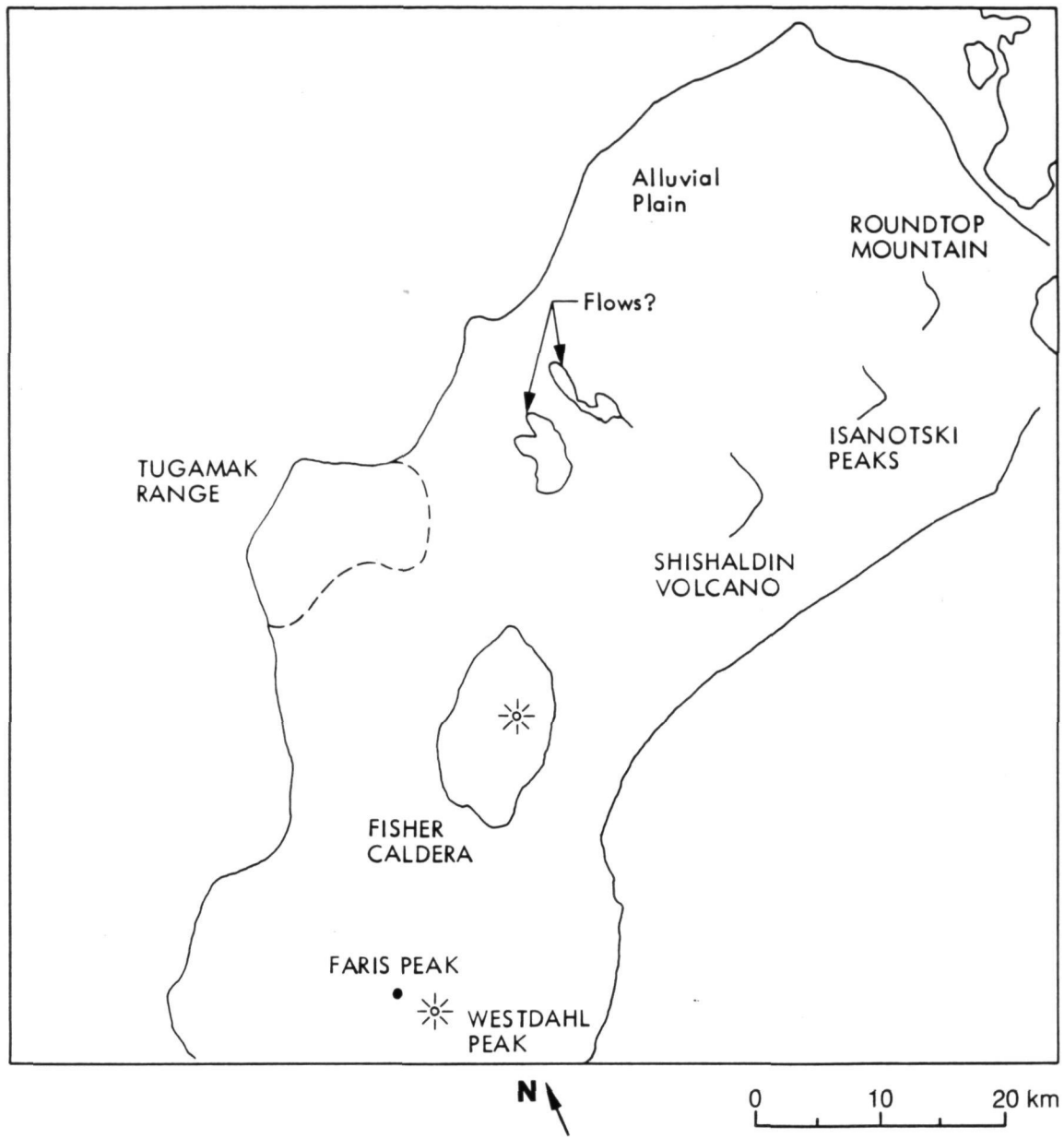
pyroclastic and volcanic rubble associated with the volcanic edifices.
Glaciofluvial plains mantle the gentler slopes.
   (Seasat image from Rev. 605.)

(v) Karst

55

18. Jamaica, West Indies

ILLUMINATION
DIRECTION →

N

0   10   20 km
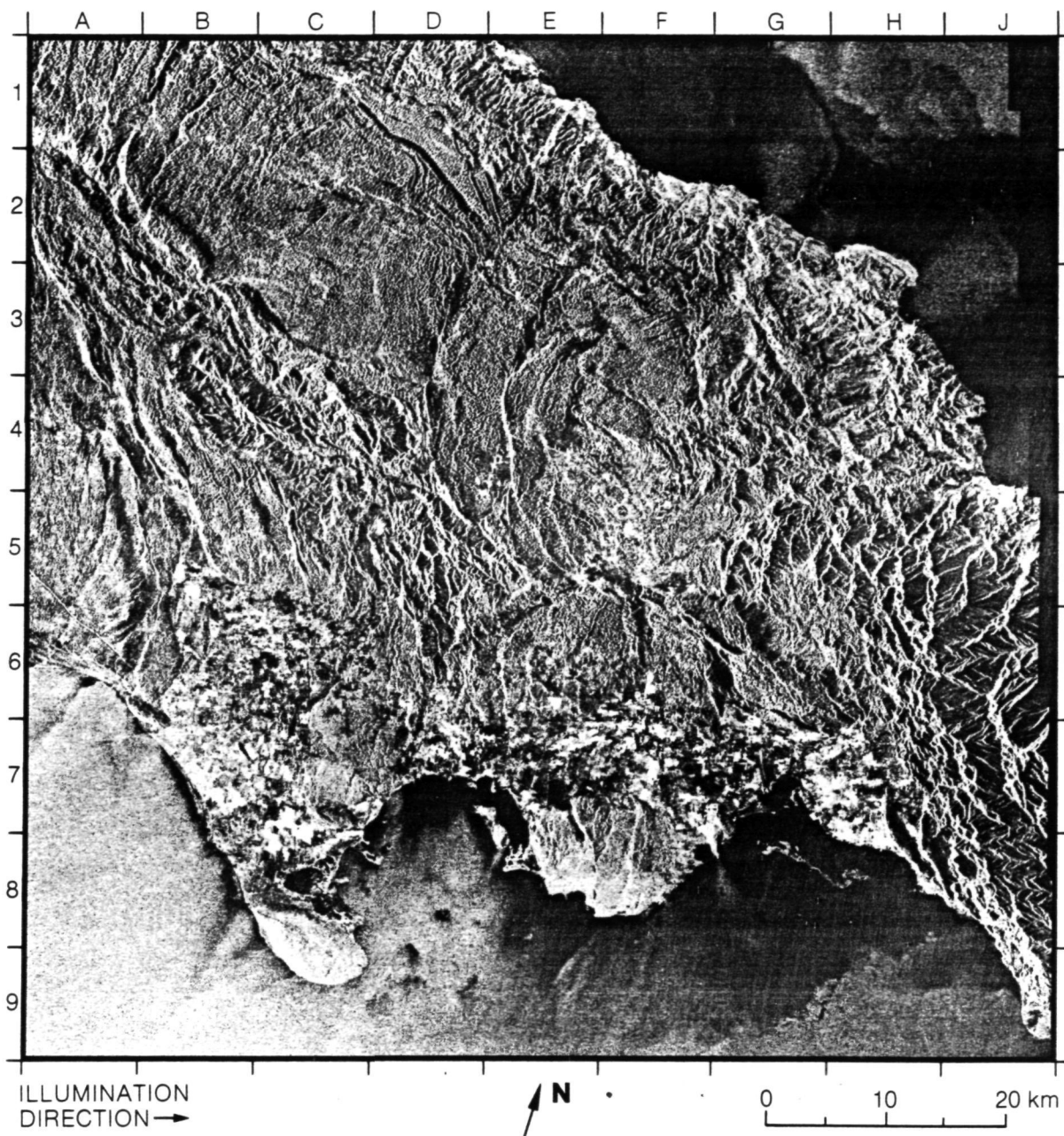
In this image of Jamaica and accompanying geologic sketch map, Kingston and agricultural areas stand out in the flat alluvial southern region (B7 to H7). The Blue Mountains in eastern Jamaica (G3 to J8) represent a pre-Eocene (mainly Cretaceous) igneous and metamorphic complex. Younger limestones cover much of the island, and are easily distinguished on the radar image due to well-developed karst topography.

A striking geologic feature of the island is the abundance of fault structures and other lineaments. Two trends are apparent: an east-west trend, parallel to

Legend:

- (stippled) RECENT ALLUVIUM
- (Ⅱ) WHITE LIMESTONE FORMATION, EOCENE
- (× ×) PRE-EOCENE BASEMENT
- (— — —) FAULT

0   10   20 km

↑N
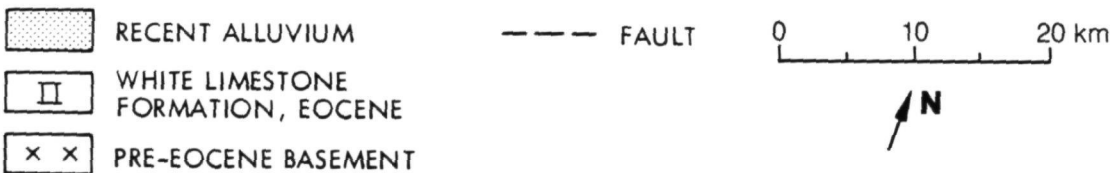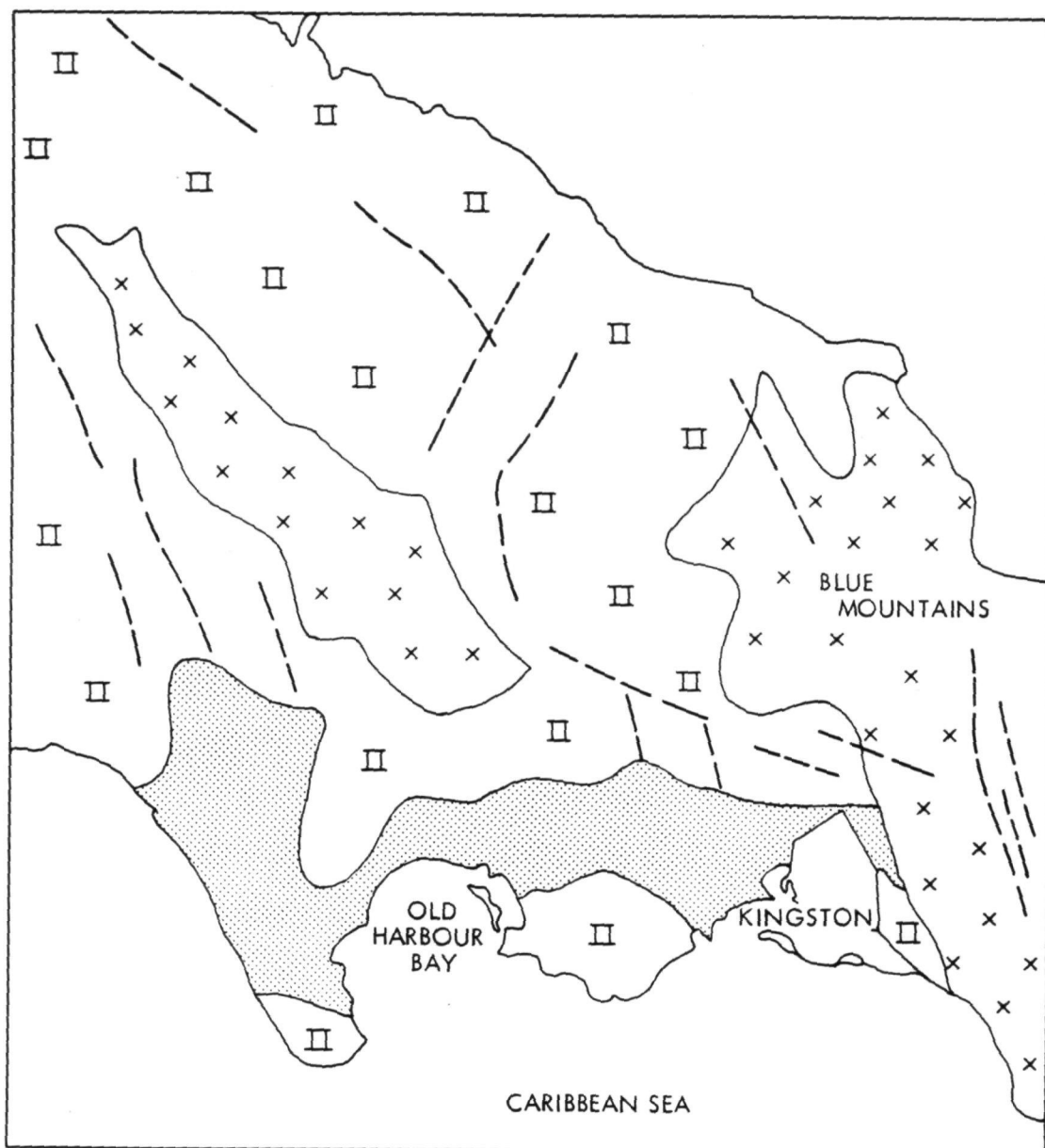
the island's elongation, and an oblique system running northwest to southeast. Jamaica lies in the plate boundary zone between the North American and Caribbean plates, and represents a tectonic focal point for relative motion between these regions. Studies of the fault systems and their displacements in Jamaica are an important constraint on relative plate motions, and aid in understanding the geologic history of the Caribbean area.

(Seasat image from Rev. 608.)

19. Northeast Dominican Republic

ILLUMINATION
DIRECTION →

↑ N

0   10   20 km
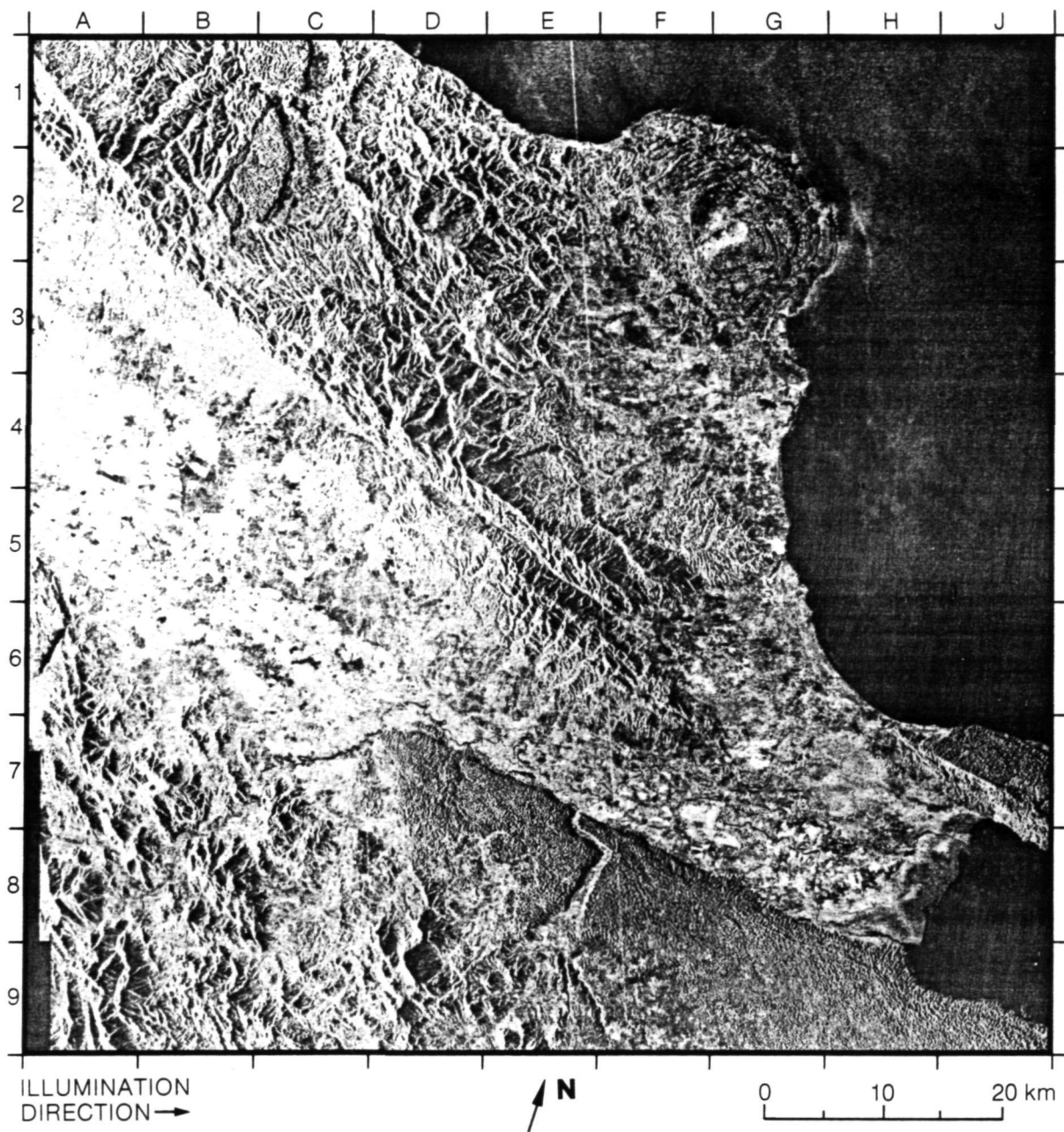
Three major topographic units that correspond to geologic units of different age are visible on the SAR image and accompanying sketch map. The youngest deposits are flat-lying soils and gravels that occupy the alluvial plain of the Rio Yuna (C7 to H8). The next older unit consists mainly of Tertiary limestones that give rise to a characteristic karst topography. Cretaceous and

	QUATERNARY ALLUVIAL DEPOSITS			---	FAULT
	TERTIARY SEDIMENTARY ROCKS, MAINLY KARST LIMESTONE		⨉ ⨉	SWAMP MARSH
⨉ ⨉	CRETACEOUS AND OLDER IGNEOUS AND METAMORPHIC ROCKS			

0   10   20 km

N
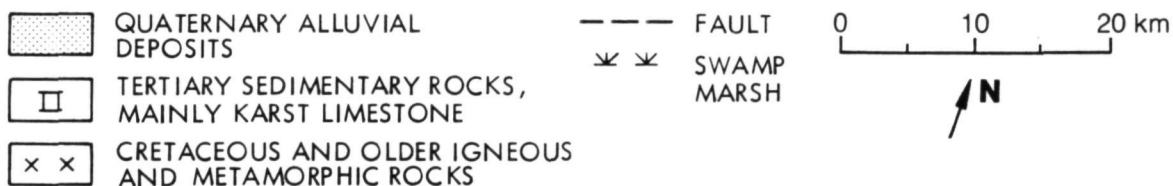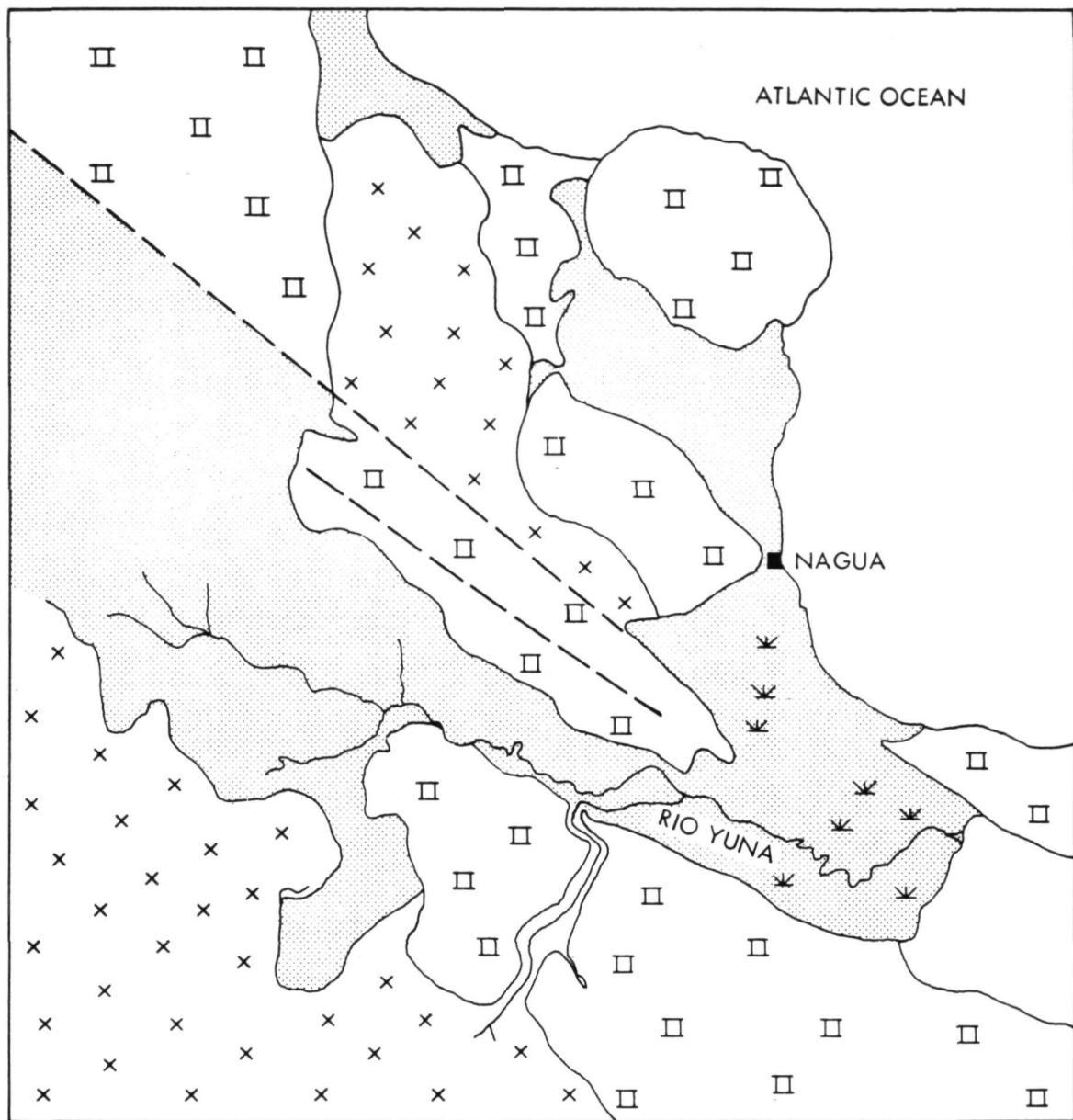
older volcanic, sedimentary, and plutonic rocks, which may be highly metamorphosed, underlie the more rugged, mountainous basement. The strong east-southeast to west-northwest trending faults from A1 to J7 parallel a major structural trend in the northern Caribbean area.

(Seasat image from Rev. 335.)

(vi) Glacial and Periglacial Landforms

20. Dease Inlet, Alaska

ILLUMINATION DIRECTION →

N

0   10   20 km
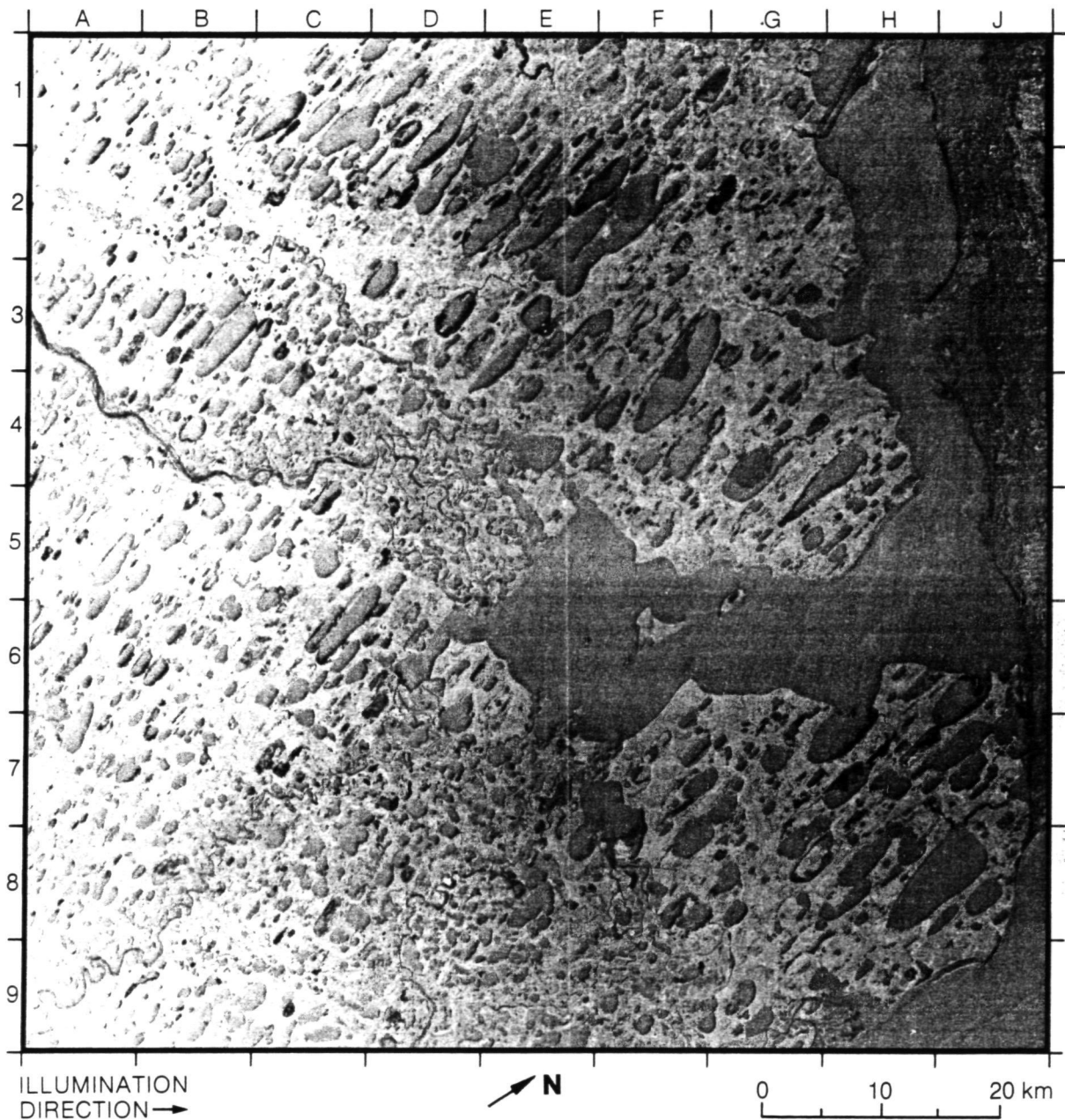
Dease Inlet (G5 to G6) and Elson Lagoon (H1 to H6) are separated from ice floes in the Beaufort Sea (J1 to J7) by the Plover chain of barrier islands. The northernmost land in the United States, Point Barrow, is situated about 2 kilometers northwest of the barrier island at the margin of H1. The Elson Lagoon shoreline is characterized by sand and silt spits (as in H1), and areas of bluffs 1 to 3 meters in height.

The oriented lakes are thermokarst features that occur by the thousand on the permafrost in this low-relief area of the Arctic north slope. The cause of the orientation has been extensively studied and debated, though it remains unresolved. Serious explanations that have been offered include thawing and subsidence followed by bimodal wind-oriented wave action, structural control, and the angle of solar radiation. Whatever may be the explanation for the
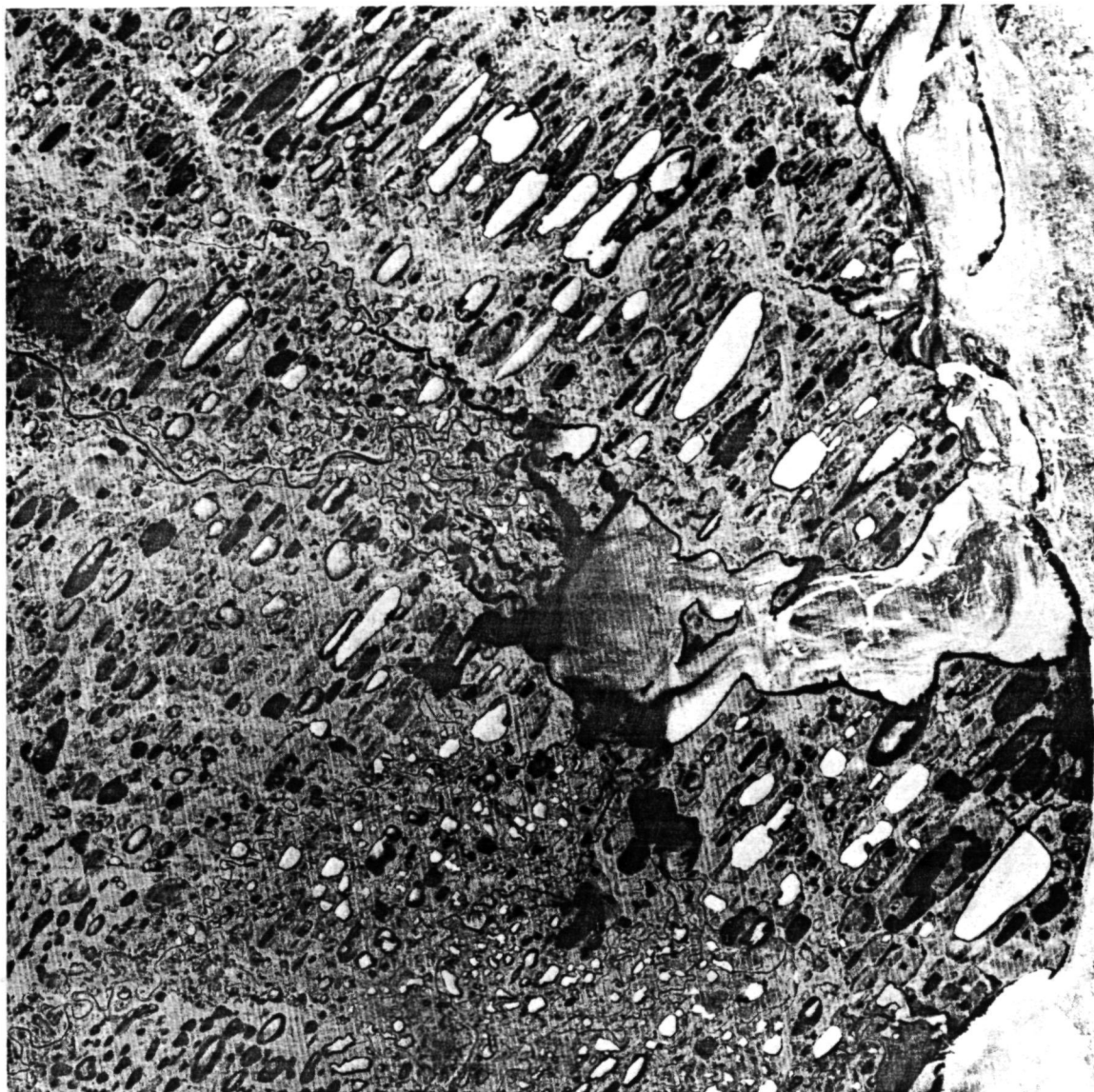
N   0   10   20 km

orientation of the lakes, it is clear that they are continually being drained and reformed, and that the processes are currently active. The lakes are mostly less than 3 meters deep. They are frozen for most of the year, but undergo partial to total thawing in summer, about the time of year that this image was acquired.

Extensive sand bars accumulate along the Meade River from A3 to D4. Meanders occur in the distributaries of the Meade at the delta in D4 to D5, and along the Topagoruk River notably from A9 to C7.

The Landsat subscene shows white to light-gray tones in Elson Lagoon, Dease Inlet, and many of the oriented lakes. These tones represent ice or ice floes in the Beaufort Sea area. Rivers and lakes that have thawed are black on the image.

(Seasat image from Rev. 322; Landsat scene ID: 5803-20324.)

63

21. Drumlin Field, Ireland

ILLUMINATION DIRECTION →

N

0   10   20 km
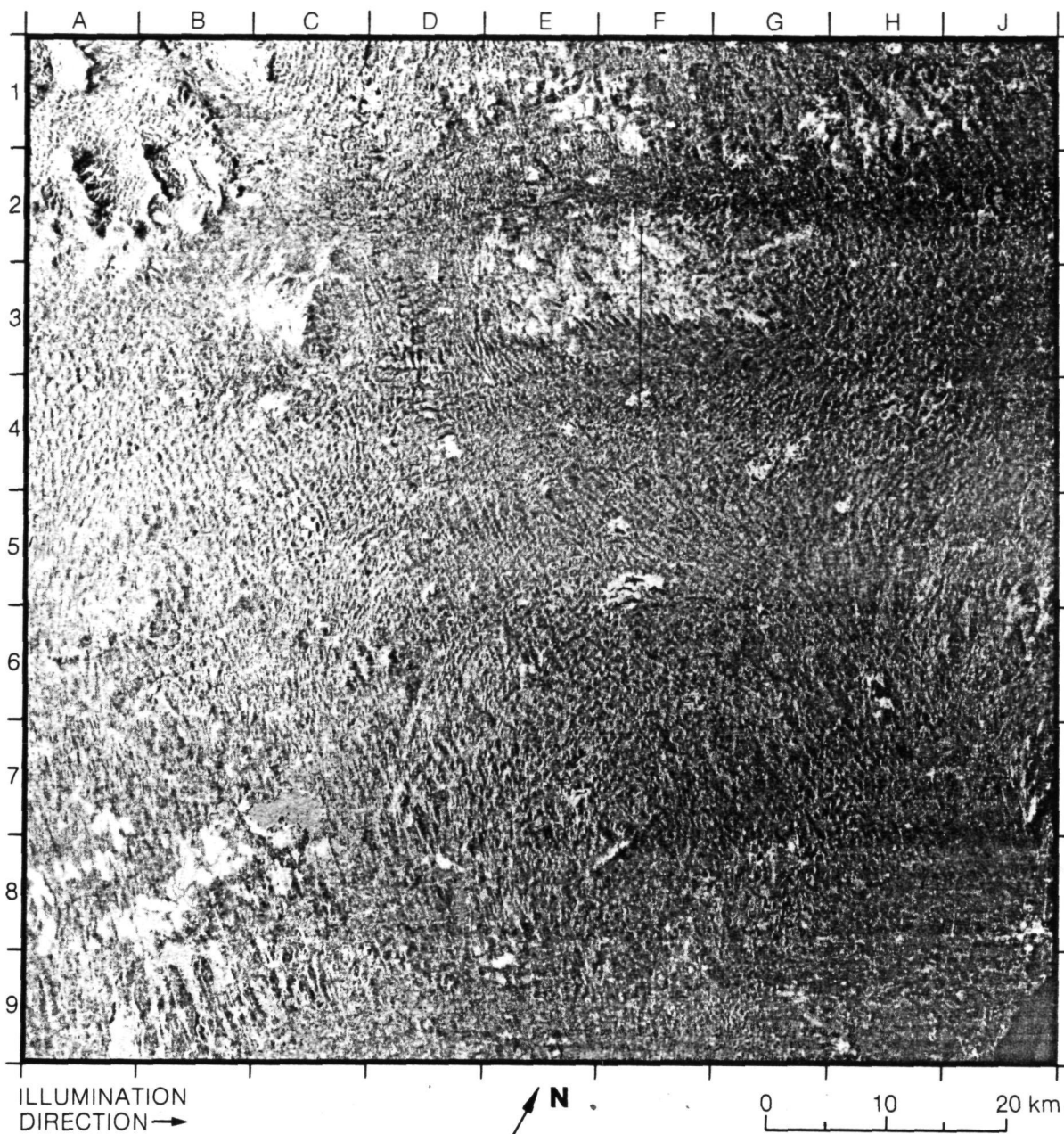
This scene extends from Dundalk Bay, at the bottom right, to a line that runs parallel to and about 40 kilometers southeast of the coast at Donegal Bay, at the top left. The town of Dundalk is denoted by the bright returns in the lower right of J8. The area contains tens of thousands of drumlins, and forms one of the most extensive drumlin regions in the world. The flow patterns of the glacial ice that formed the drumlins are clearly evident on the radar image, and to a lesser extent they are perceptible on the facing Landsat image. The curvilinear orientation of the drumlins from J4 through G5 to H8, and from C6 through F5 to H8 on the radar image reveal two flow patterns of ice that drained into Dundalk Bay. The linear pattern of drumlins in C1 to D1, at the head of Lower Lough Erne, denotes the flow of ice that drained northwest toward Donegal

N
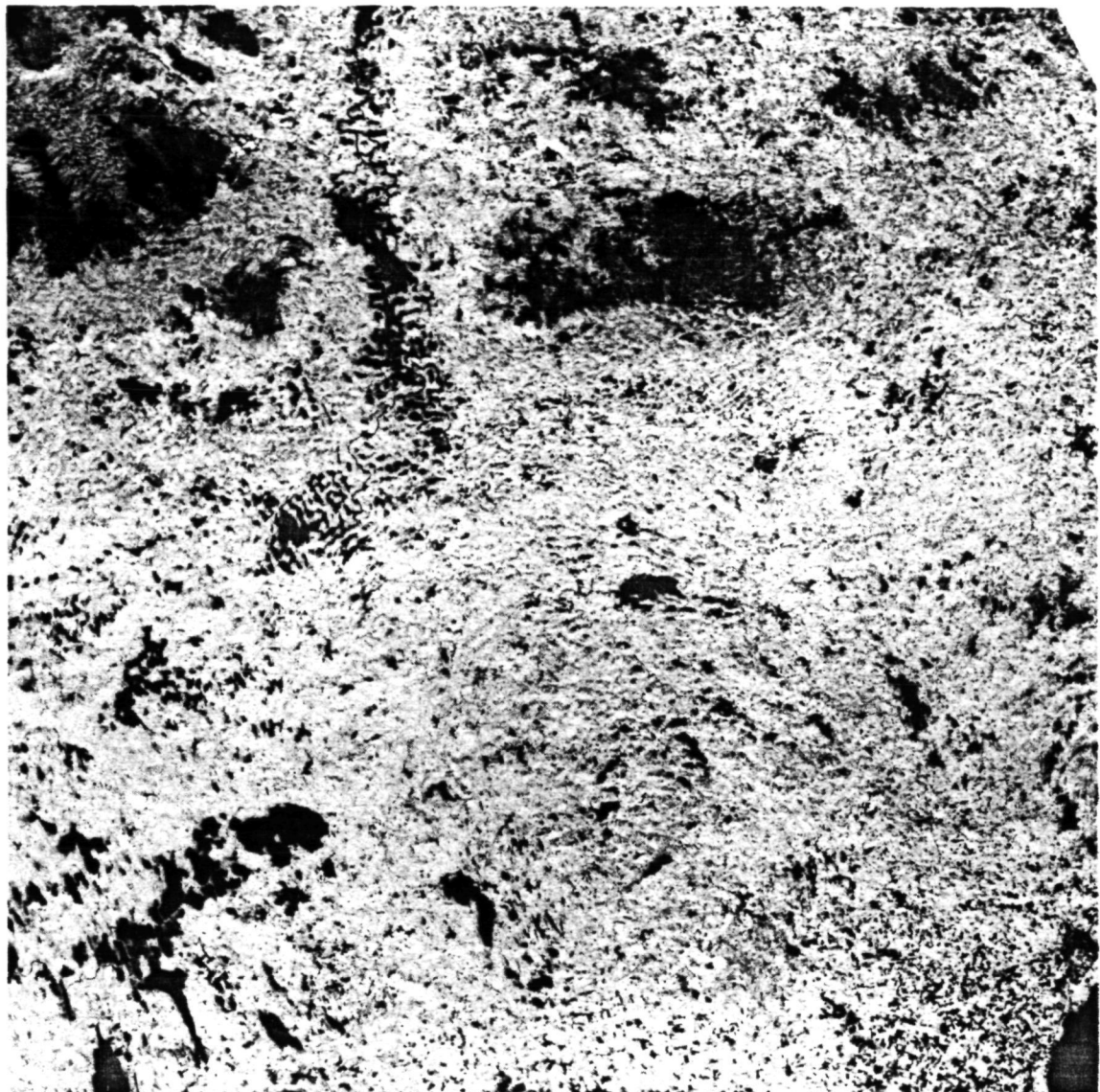
0   10   20 km

Bay. The effect of glaciation has totally disrupted drainage, and created extensive bogs, ponds, and lakes. Numerous lakes and ponds that are dark on the Landsat image are correspondingly medium-gray to bright on the radar image. This may reflect seasonal conditions at the different times of the year when the respective images were acquired, in some cases including differential effects of vegetation in a poorly drained environment.

(Seasat image from Rev. 791; Landsat image received at Fucino, Italy, Apr. 21, 1976. This digitally mosaiced enhanced Landsat scene was provided by courtesy of Mr. Nigel Press, Nigel Press Associates, Ltd., Edenbridge, Kent, U.K.)

(vii)   Enclosed Basin

22. Death Valley, California

ILLUMINATION
DIRECTION →

↗ N

0   10   20 km
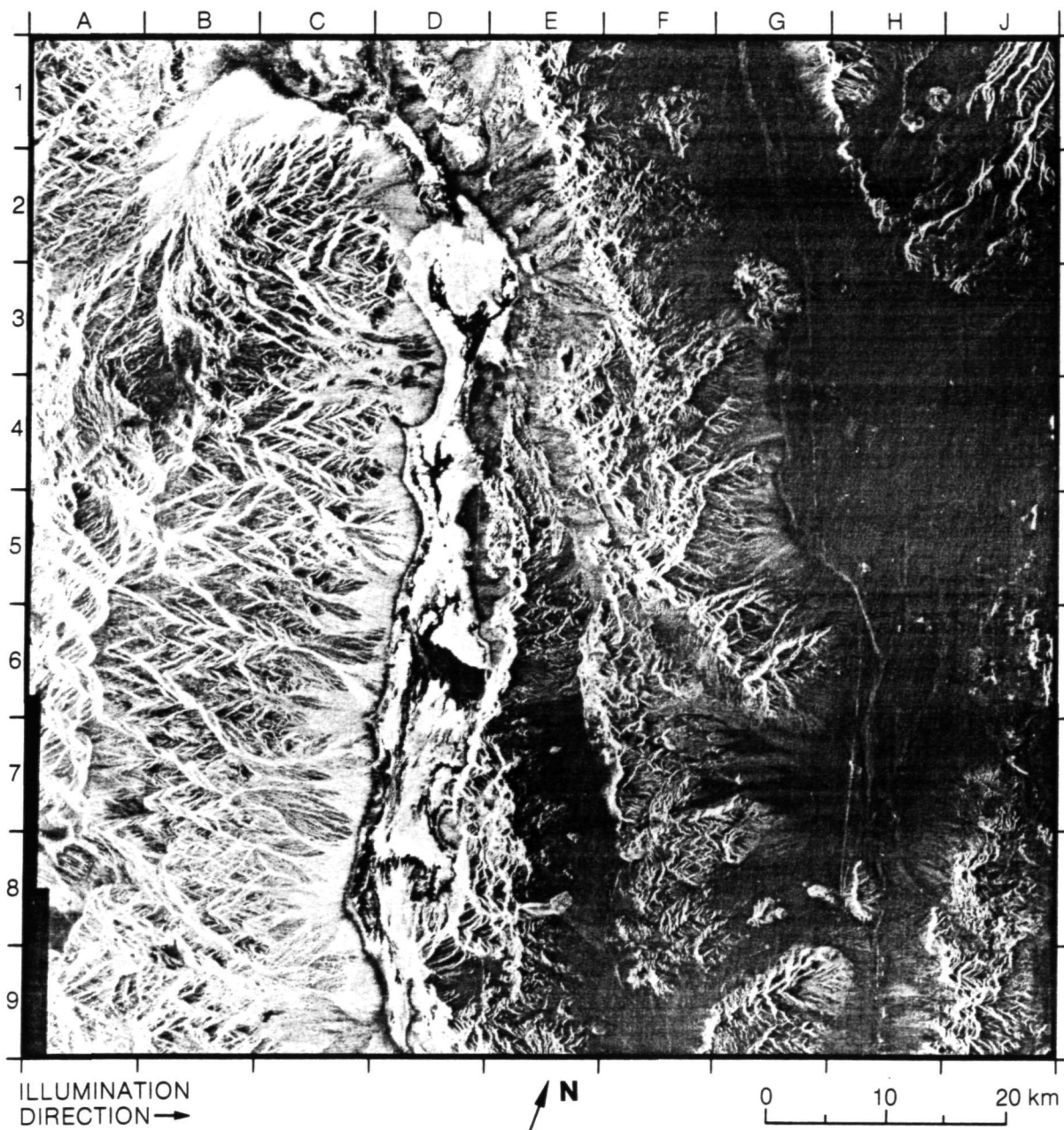
The large massif (A1 to C1 through A9 to C9) is the Panamint Range whose early Quaternary, Cambrian, and late Precambrian outcrops have different textures on the image. Fans draining eastward (e.g., D5) display smooth (dark) desert pavements and basal sand facies cut by rougher (bright) active channel deposits. The valley floor units range from extremely rough salt deposits (bright) to smooth playas (dark). The mottled bright tones in the southern third

EXPLANATION

	Qhe	ERODED SILTY ROCK SALT
	Qhr	SILTY ROCK SALT, ROUGH FACIES
	Qhs	SILTY ROCK SALT, SMOOTH FACIES
	Qh	MASSIVE ROCK SALT
	Qsg	MASSIVE GYPSUM
	Qsm	MARSH DEPOSITS, SULPHATE ZONE
	Qch	SALINE FACIES, CARBONATE ZONE
	Qsh	SALINE FACIES, SULPHATE ZONE
	Qcm	MARSH DEPOSITS, CARBONATE ZONE
	Qcs	SAND FACIES, CARBONATE ZONE
	Qcsi	SILT FACIES, CARBONATE ZONE
	Qg_4	NUMBER 4 FAN GRAVEL
	Qf	FLOOD PLAIN DEPOSITS
	Qg_3	NUMBER 3 FAN GRAVEL
	Qg_2	NUMBER 2 FAN GRAVEL
		PRECAMBRIAN TO PLIOCENE ROCKS, UNDIVIDED

QUATERNARY — RECENT — PLEISTOCENE

N

0   10   20 km

of Death Valley (E7 and E8) correspond to a floodplain whose brine-water table may contribute to the radar return. Further east lies the disorganized Amargosa Range (E1 to G1 through F8 to G8), cut by the Furnace Creek and Keane Wonder fault zones. The lower right of the scene (G8 to J8 and G9 to J9) contains the Amargosa River drainage and the low ranges of western Nevada.

(Seasat image from Rev. 1140.)

(viii)   Dissected Plateau

23. Grand Canyon, Arizona

ILLUMINATION
DIRECTION →

↗ N

0   10   20 km
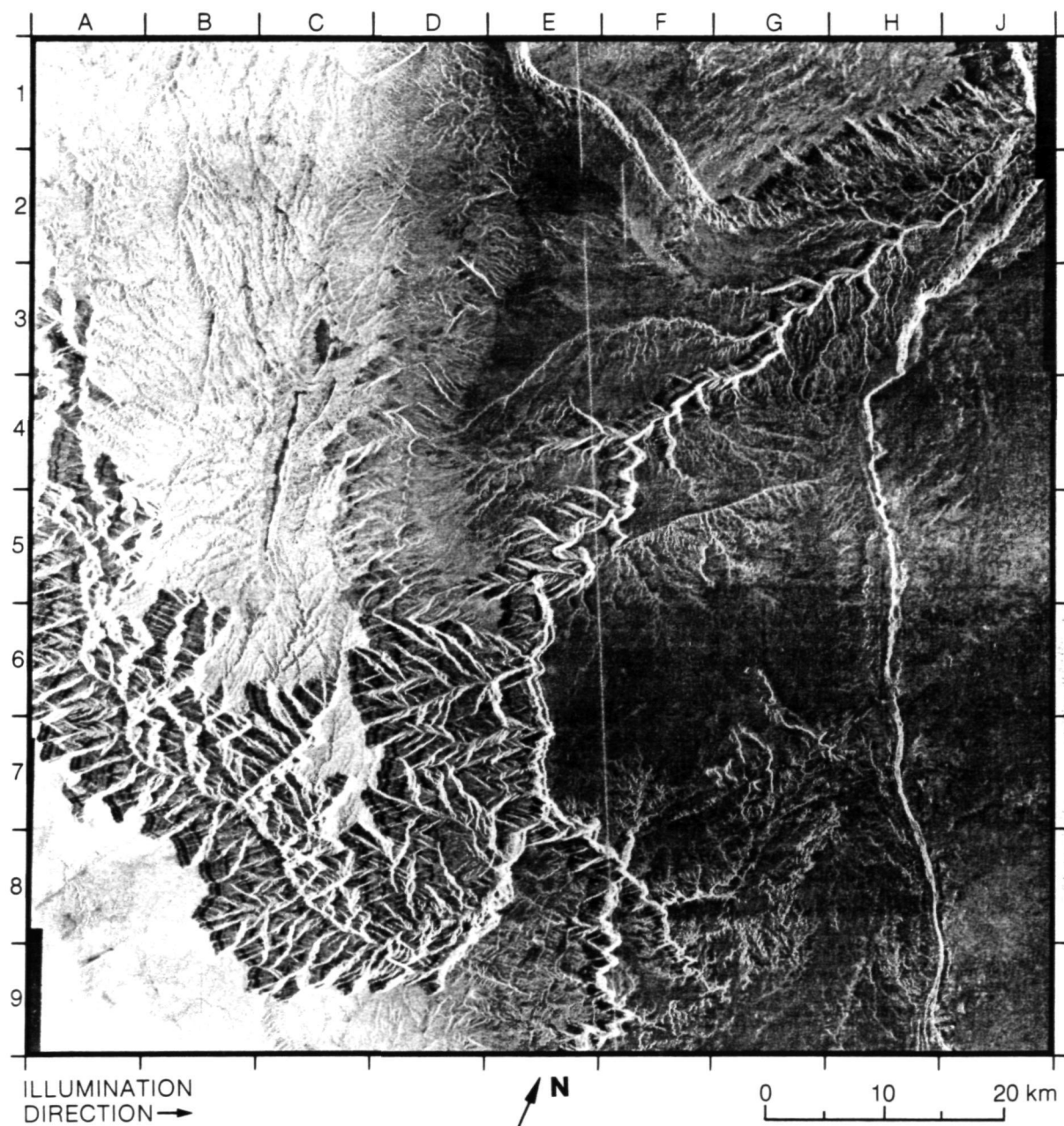
The Colorado River cuts deeply into the uplifted Colorado Plateau forming a canyon nearly 1600 meters deep. Exposed in the canyon walls are thick, nearly flat-lying sedimentary units. More resistant units form cliffs that cast shadows (B8 and D7). Parallel lineaments (B3, B4, C3, and C4) are small
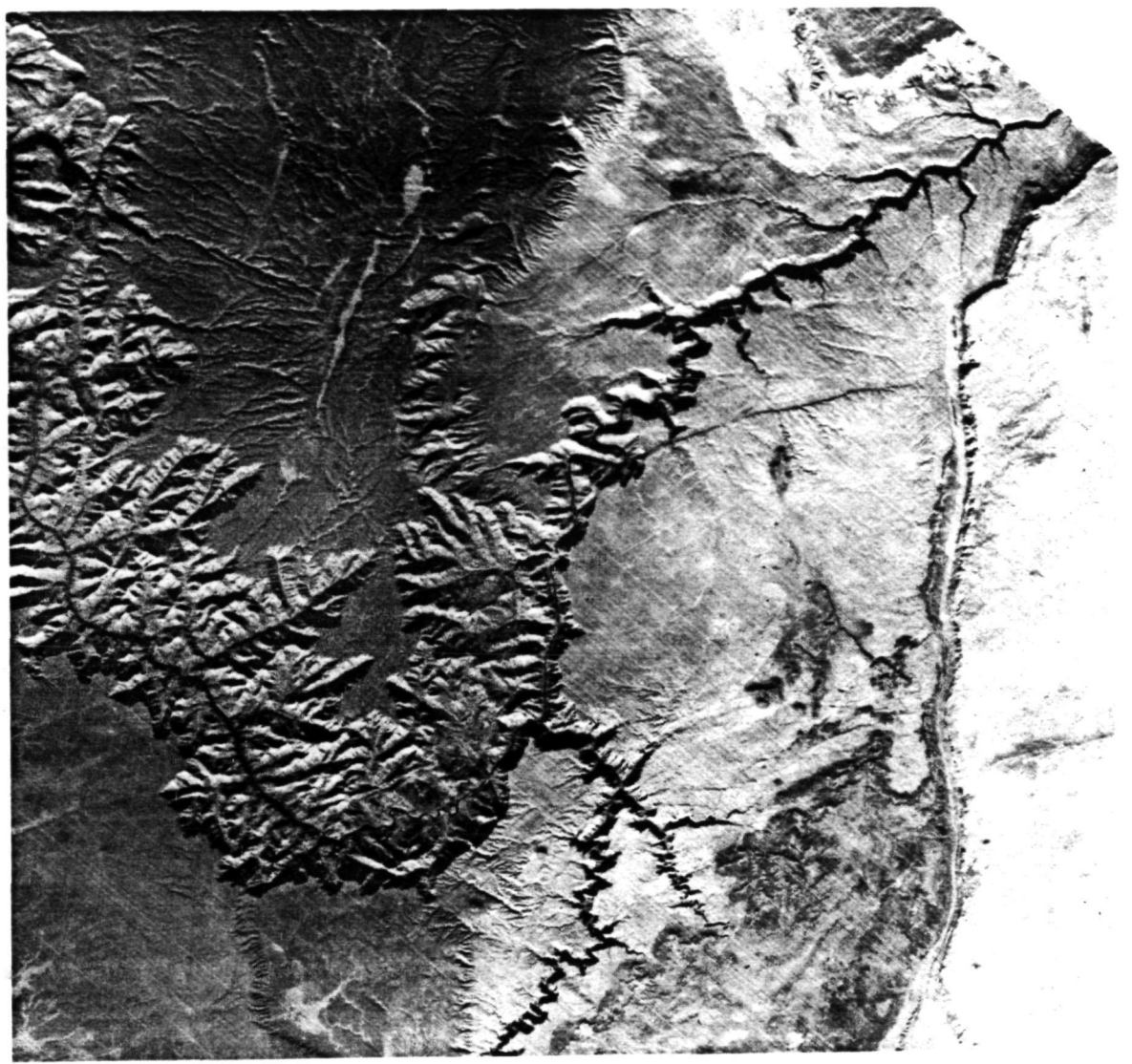
N   0   10   20 km

displacement faults associated with the Kaibab upwarp. The doubled features
(F2) result from a change in the radar settings.
(Seasat image from Rev. 322; Landsat scene ID: 1464-17354.)

(ix) Coastal Features

75

24. Camden Bay, Alaska

ILLUMINATION DIRECTION →

N

0   10   20 km
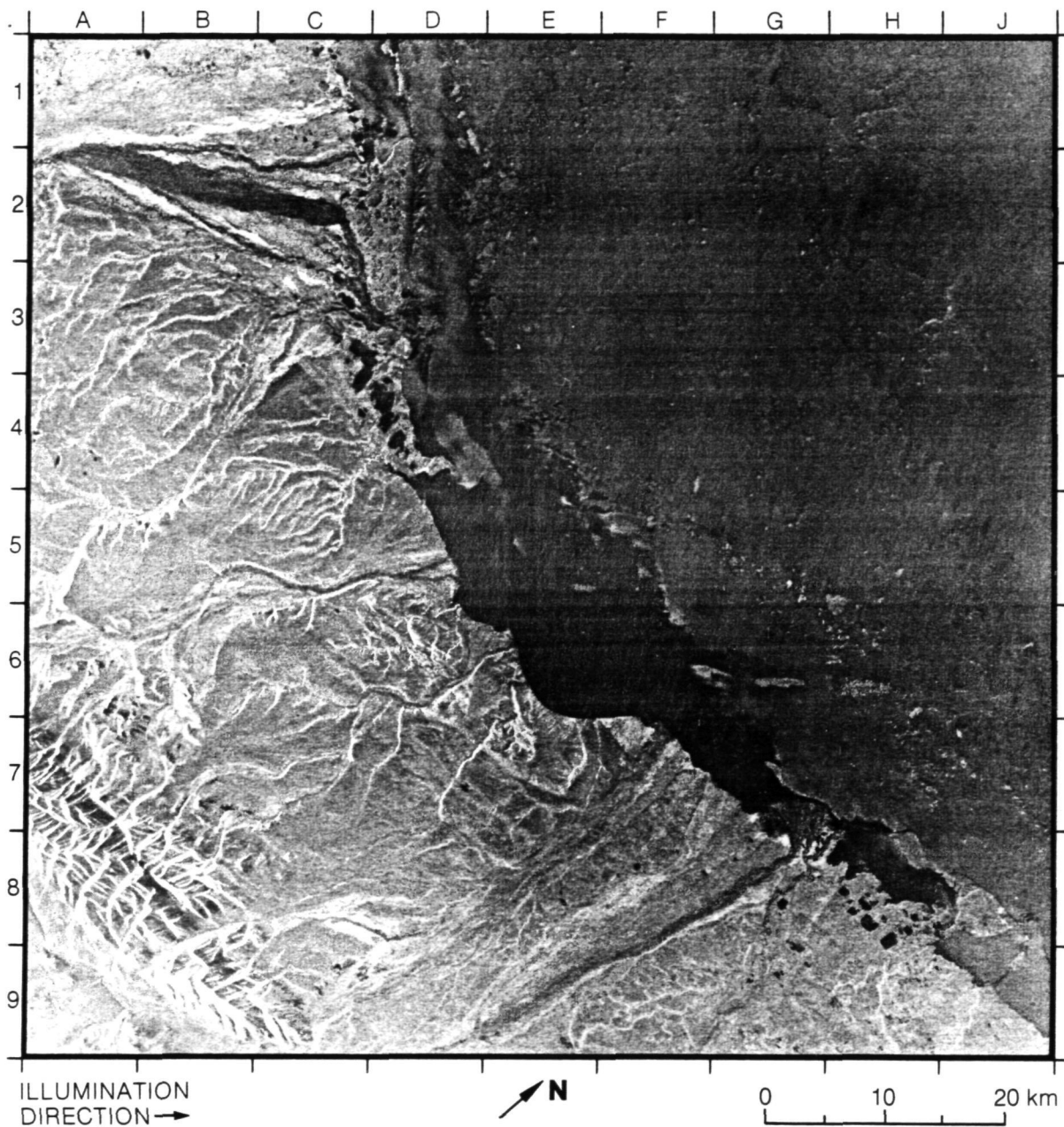
Camden Bay is on the Arctic north shore of Alaska, approximately 150 kilometers east of the giant oil fields at Prudhoe Bay. The coastal plain in this scene is covered by older moraines and glacial outwash. It is traversed by numerous braided streams that drain northward to the Beaufort Sea where they form deltas of varying magnitude (e.g. Staines River, C1; Canning River, D3; Hulahula River, G7 to G8). The braided river channels are more clearly defined on the facing Landsat MSS image. The barren rugged Sadlerochit Mountains,

N

0   10   · 20 km
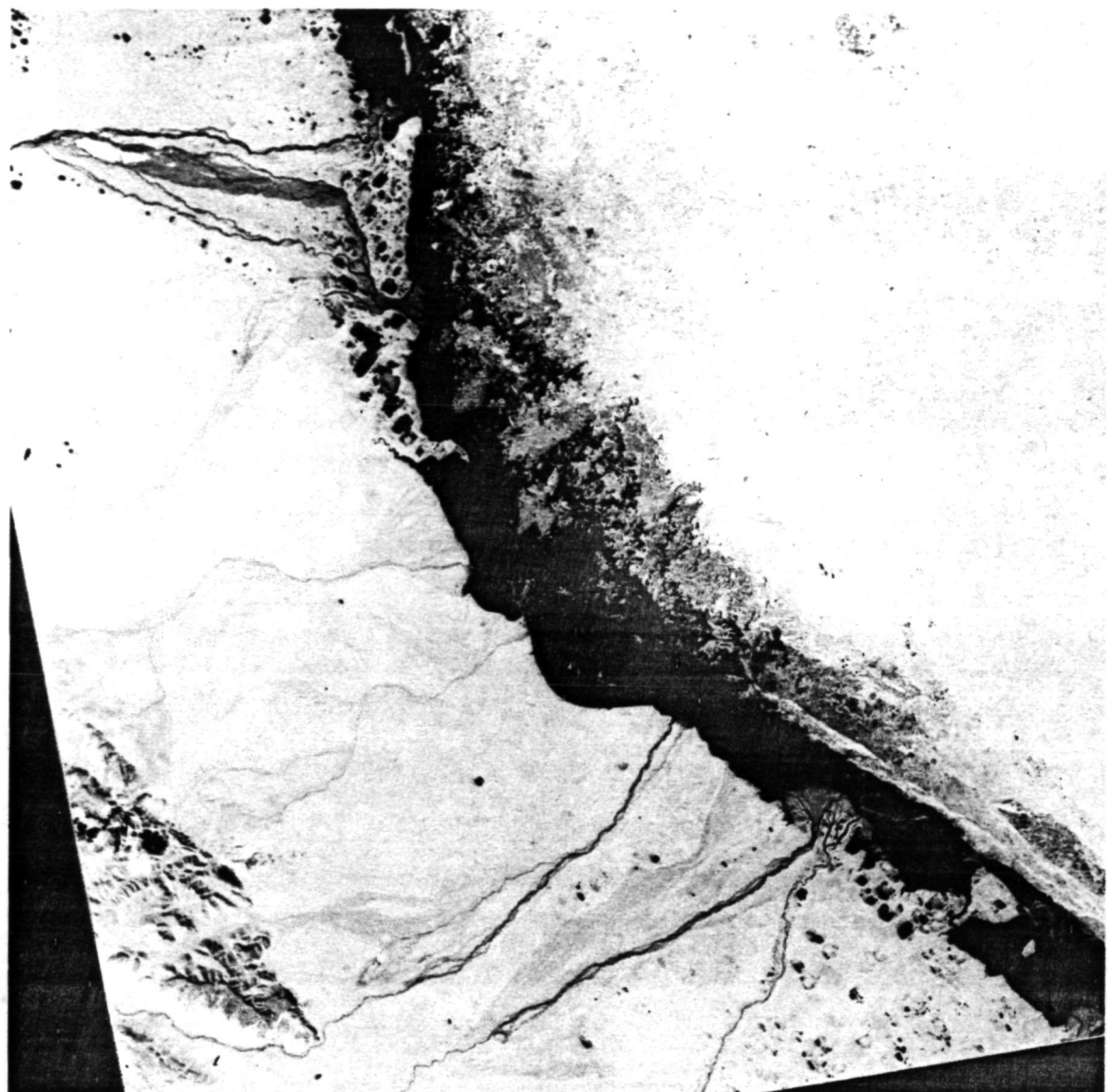
with elevations in the range of 1000 to 1300 meters are at lower left (A7 to C9).

The coastline is characterized by barrier islands, as from D1 to D3. Oriented lakes are present, but in much fewer numbers than further west (see Dease Inlet). Coastal waters are black on the radar and the facing Landsat image. Both images were acquired about midsummer. Both show ice floes and sea ice in the Beaufort Sea, across the upper right.

(Seasat image from Rev. 781; Landsat scene ID: 21633-20531.)

25. Southern California Coast

The coastline from Huntington Beach (B3) to Oceanside (G5) is shown in this SAR image. Marine terraces, or raised beaches, provide a record of tectonic uplift. Three major lagoons (H6) are also visible in this portion of the image. Lake Elsinore (G1) marks one location on the Elsinore Fault (F1 to J2). This is an active fault zone that is an offshoot of the San Andreas system. Major freeways (B1) appear as a series of dark linear patterns in the Orange County
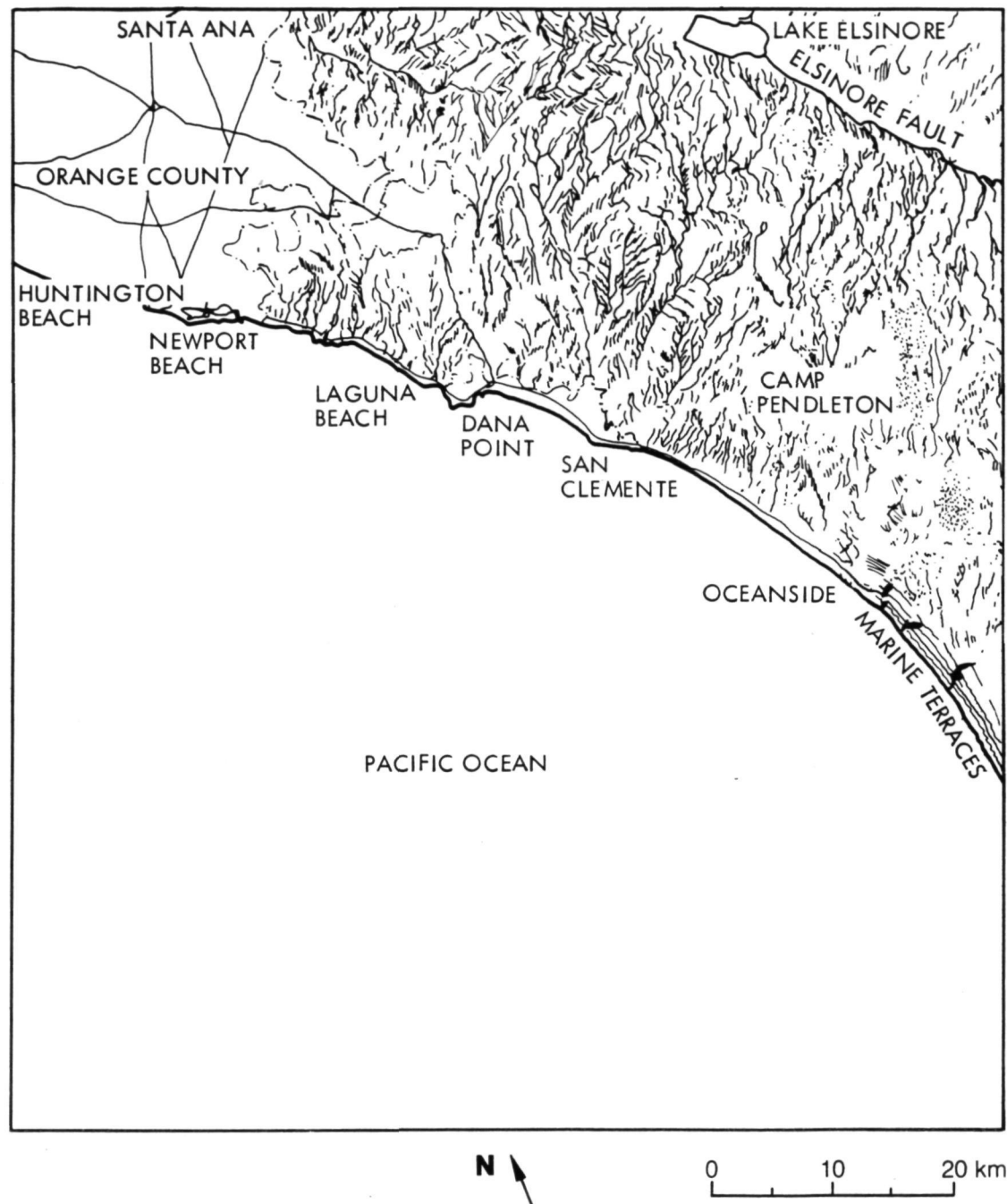
area. Long-wavelength ocean swells are prominent on the Pacific Ocean surface. The contrasting regions of light and dark on the ocean surface represent differences in roughness caused by local wind effects. The line crossing the center portion of the image is a result of a radar calibration pulse.
(Seasat image from Rev. 1291.)

B. Hydrology – Water Resources

(x) Drainage Networks

83

26. Wabash/Ohio Rivers, Kentucky-Indiana-Illinois

ILLUMINATION
DIRECTION →

N

0   10   20 km
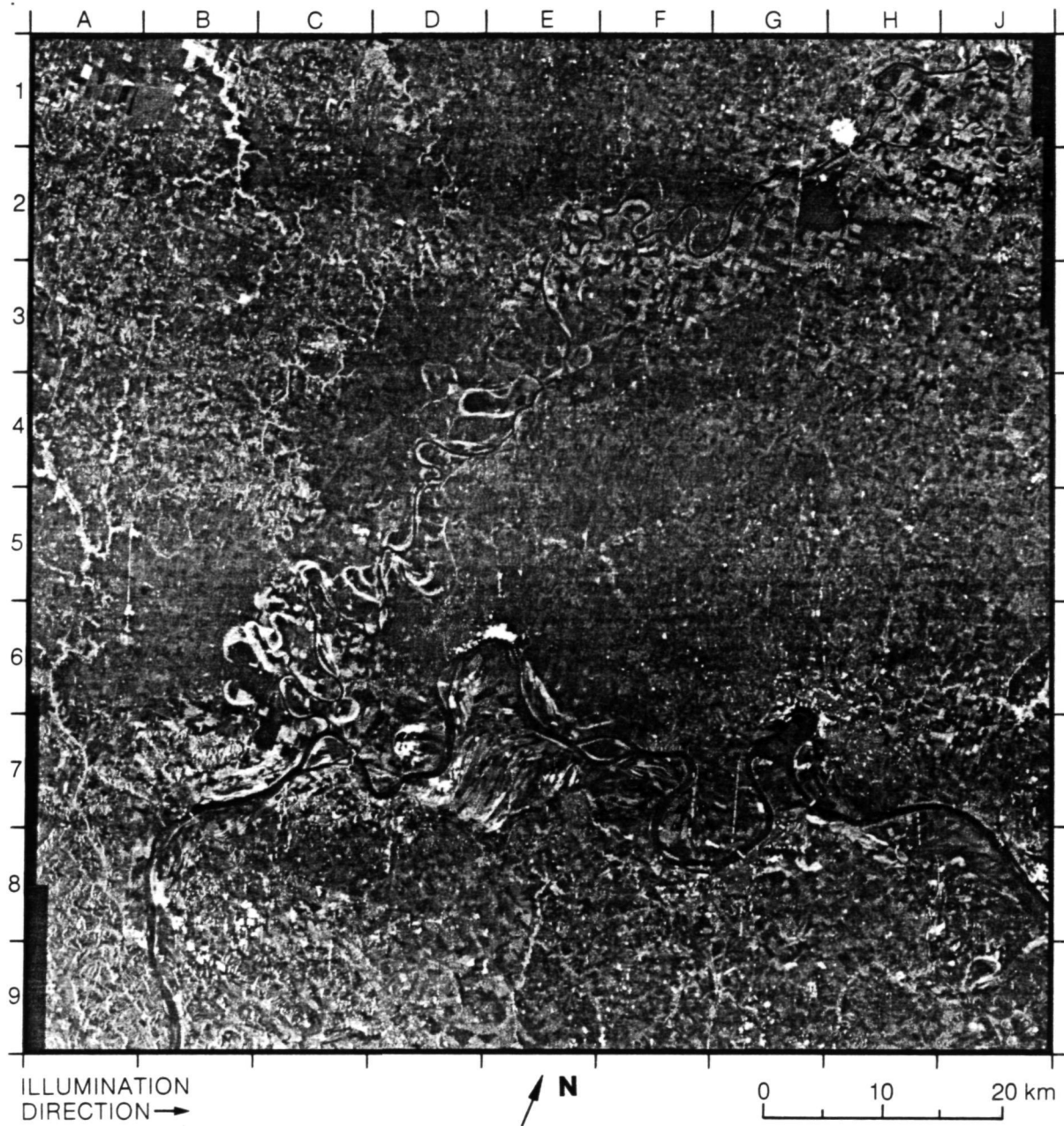
This radar image shows the confluence of the Wabash and Ohio Rivers in the tristate area of Kentucky-Indiana-Illinois. It is a petroleum producing region situated at the southern margin of the Illinois Basin. Many of the oil- and gas-well pumps act as point-target reflectors to the radar, and they appear as bright points on the image.

Numerous cutoff meanders and meander scars yield bright returns along the floodplain of the Wabash River from C7 to E3, probably because of associated vegetation. The Wabash River channel served to mark the Indiana-Illinois state line in this area over a century-and-a-half ago. The river has since changed its course and portions of the former course are now marked by cutoff meanders. The cutoff meanders on the facing sketch map shown by dashed lines west of the present channel are part of Indiana; the one shown by a dashed line east of the present channel is part of Illinois.

A large point bar with a succession of concentric depositional ridges occurs in the floodplain of the Ohio River, south of Mount Vernon, Indiana, from E6 to

I L L I N O I S

Oil Wells

MOUNT CARMEL

WHITE RIVER

GRAYVILLE

RIVER

PRINCETON

ENFIELD

WABASH

CARMI

Numerous Oil and Gas Wells

NORRIS CITY

LITTLE WABASH RIVER

NEW HARMONY

I N D I A N A

RIDGWAY

MOUNT VERNON

EVANSVILLE

OHIO RIVER

SHAWNEETOWN

Numerous Oil Wells

Ridges on Point Bar

HENDERSON

GREEN RIVER

ILLINOIS

K E N T U C K Y

↑ N

0   10   20 km
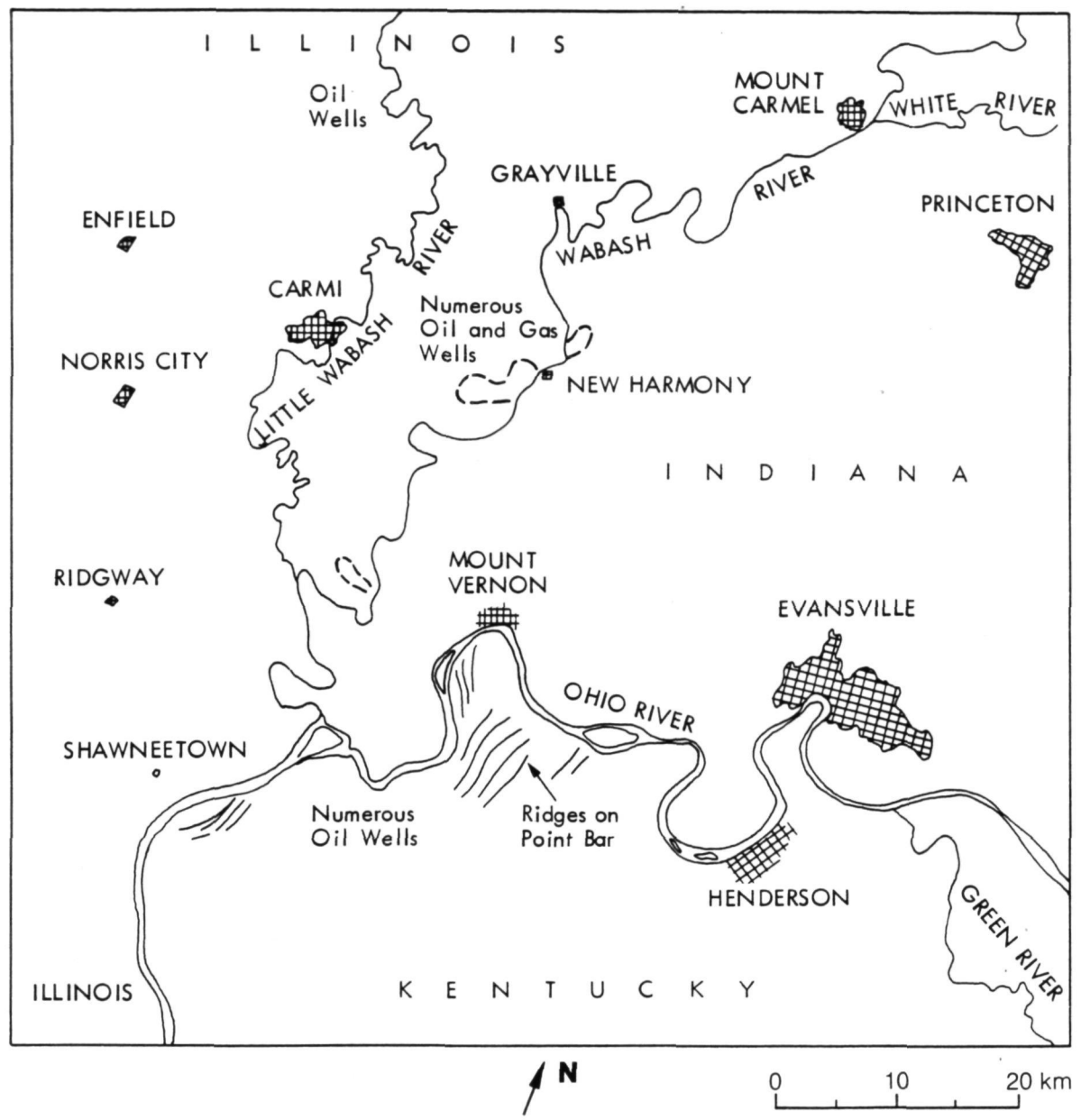
D6 and E7 to D7. Checkered patterns on the bottomlands between Evansville, Indiana, and Henderson, Kentucky, suggest extensive cultivation.

Mount Vernon appears much brighter on the image than Evansville, though it is many times smaller in area. Likewise Mount Carmel, Illinois, appears much brighter than Princeton, Indiana, though it is the smaller of the two cities. In both instances, the explanation for this lies in the orientation of the major streets relative to the direction of radar illumination. The streets of both Mount Vernon and Mount Carmel are mostly near-parallel or near-normal to the direction of radar illumination, and, consequently, the respective cities appear very bright. The streets of both Evansville and Princeton are mostly oriented approximately north-south or east-west, sufficiently divergent from the radar illumination direction to be barely perceptible on the image. Thus the respective cities appear obscure.

(Seasat image from Rev. 565.)

27. Sierrita Mountains, Arizona

ILLUMINATION DIRECTION →

↗N

0   10   20 km
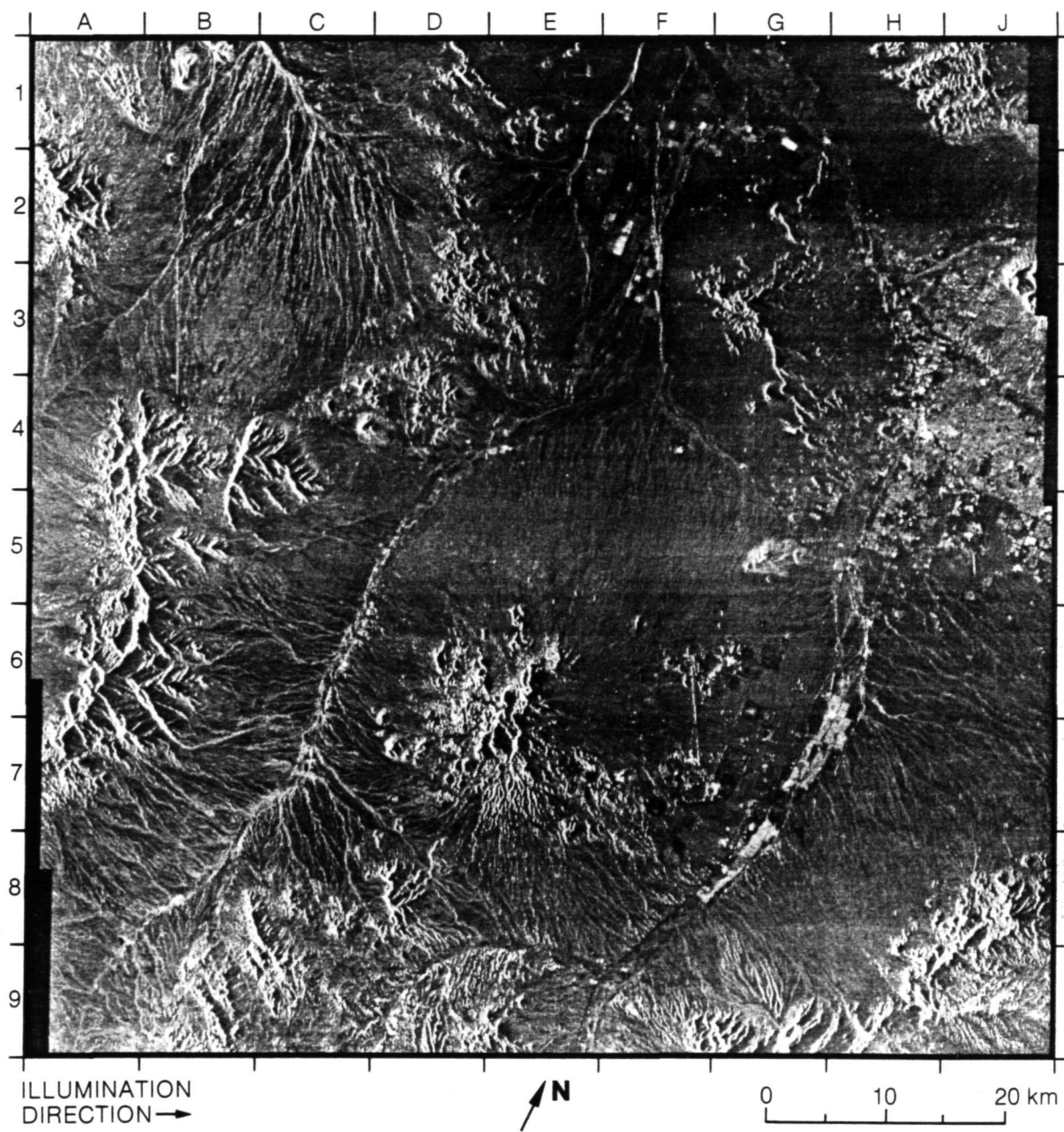
The Sierrita Mountains (D6 to D7 and E6 to E7) are an erosional remnant flanked by two drainages, Brawley Wash (E4 to C7) and the Santa Cruz River (H6 to F8). The radar image strongly highlights subtle desert drainage features (C2 and E8) and small rock outcrops (D4 and E9).

In contrast, the Landsat image (right) provides better lithologic discrimination based on tone, as at Black Mountain (G5). Major mountain features in the
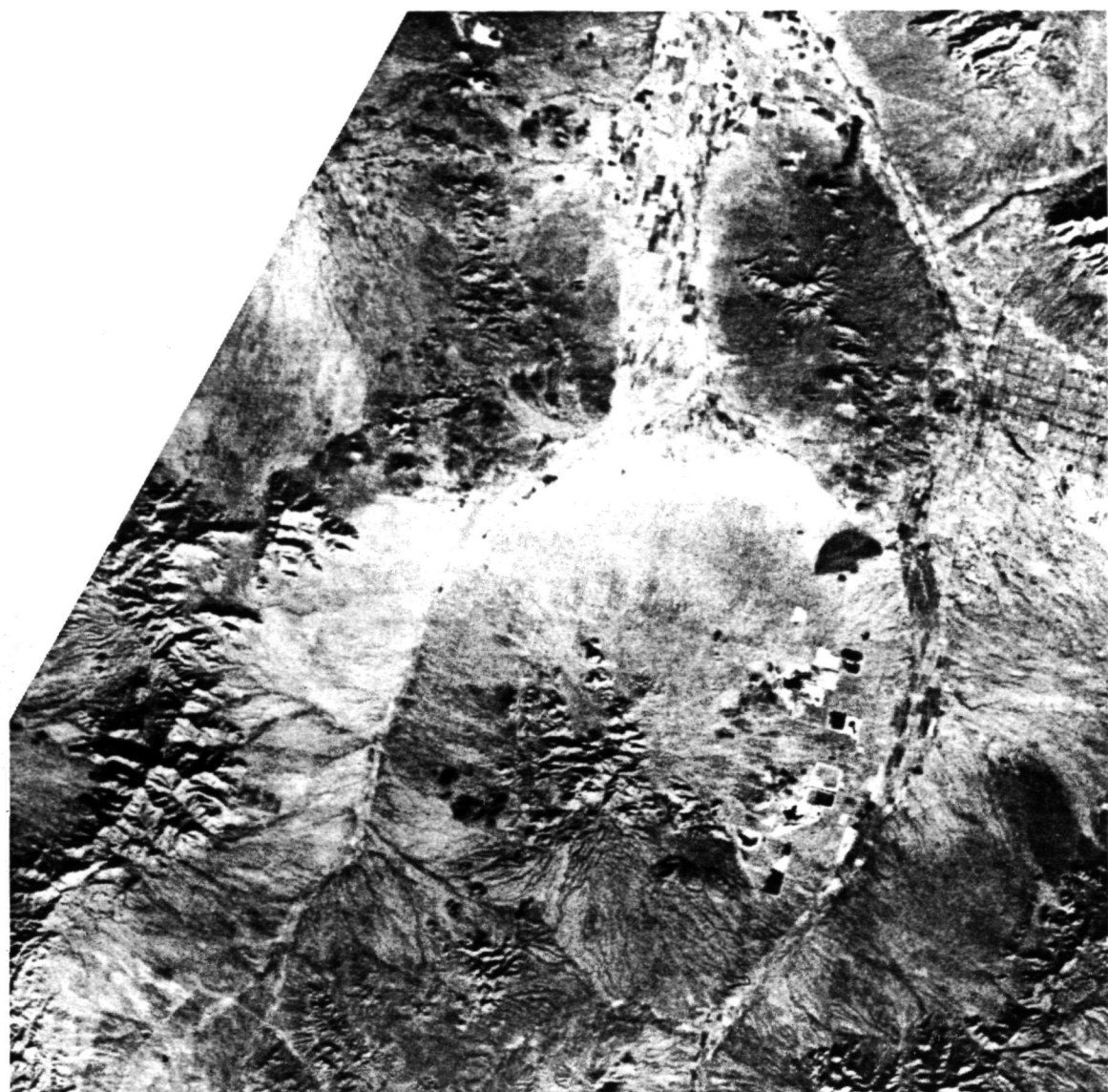
/N   0   10   20 km

scene include the Baboquivari Mountains (B4 to A7) and the Santa Rita
Mountains (H9 to J9). The city of Tucson is visible at J3 to J4.
(Seasat image from Rev. 523; Landsat scene ID: 10516–17250.)

(xi) Coastal Wetlands

28. Everglades National Park, Florida

ILLUMINATION
DIRECTION ➞

↗ N

0   10   20 km
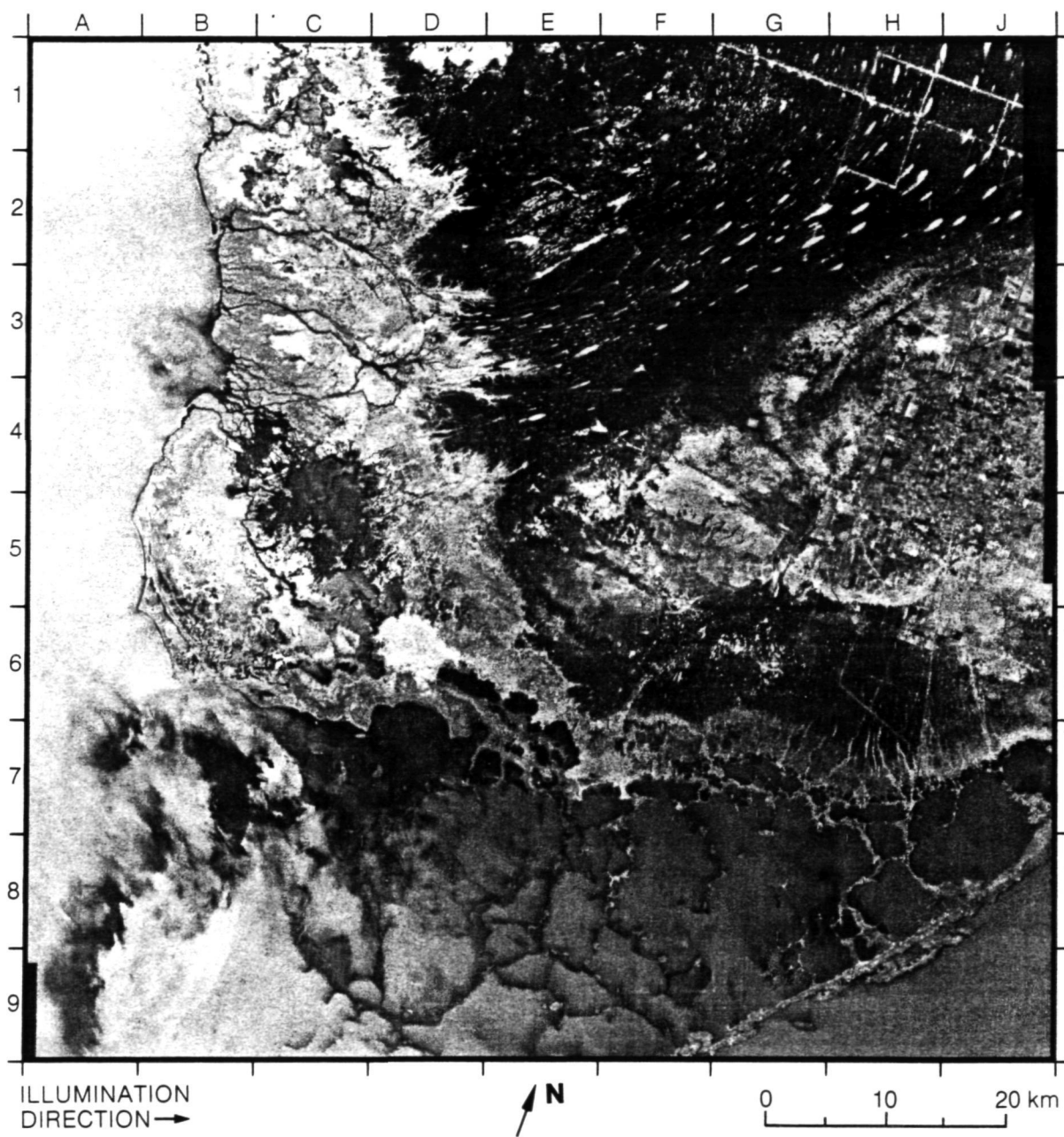
Bright teardrop shapes are hardwood "hammacks" aligned with the overall drainage pattern from Lake Okeechobee. The islands form by the buildup of rafted vegetation during repeated drying and flooding cycles. They are slightly elevated above the surrounding marshland, allowing

N
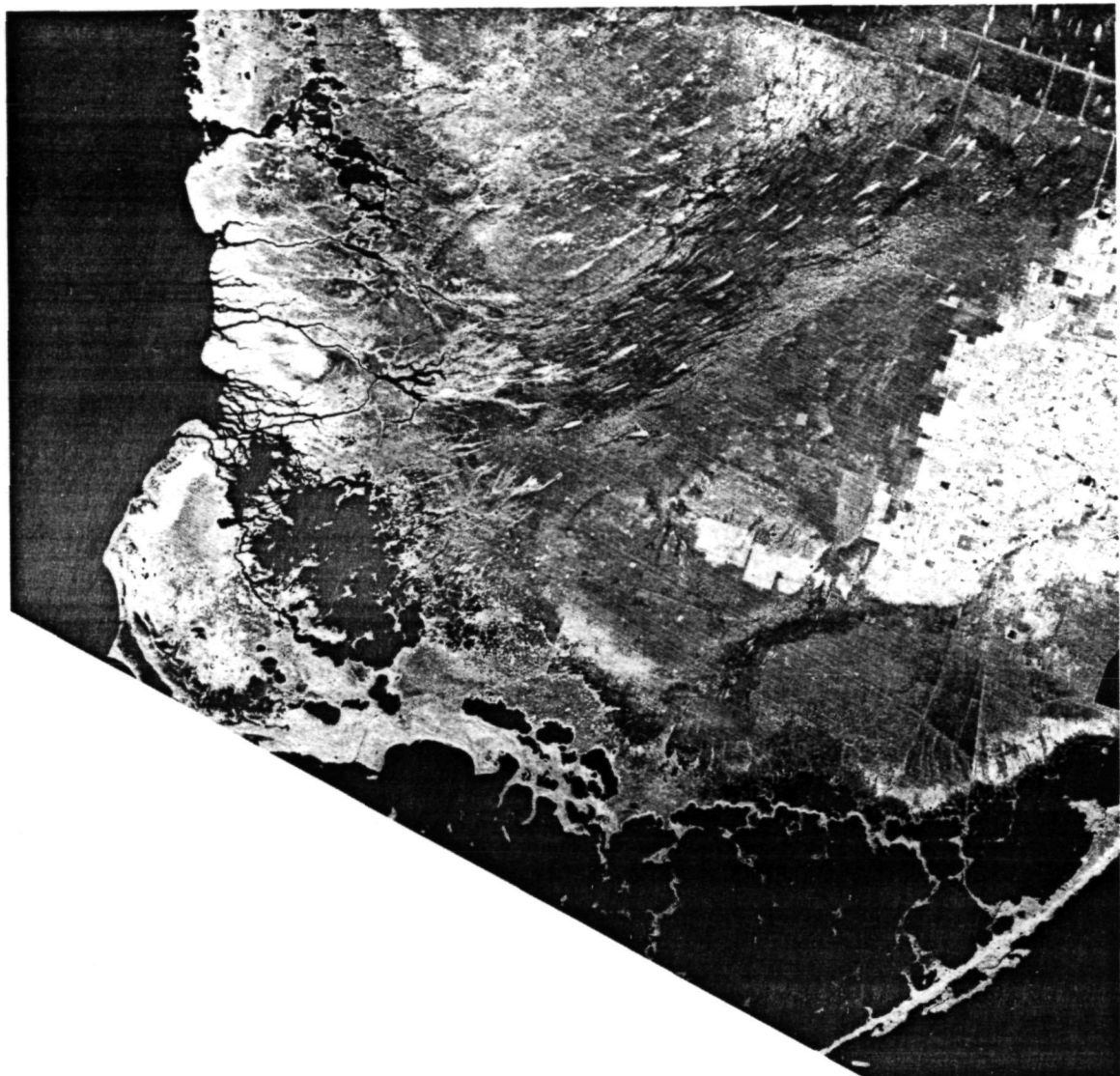
0   10   20 km

hardwood vegetation to thrive and making them highly reflective of the radar
signal.
    (Seasat image from Rev. 809; Landsat scene ID: 21210-14475.)

29. Gulf Coastal Wetlands, Louisiana

ILLUMINATION DIRECTION→

↗ N

0   10   20 km
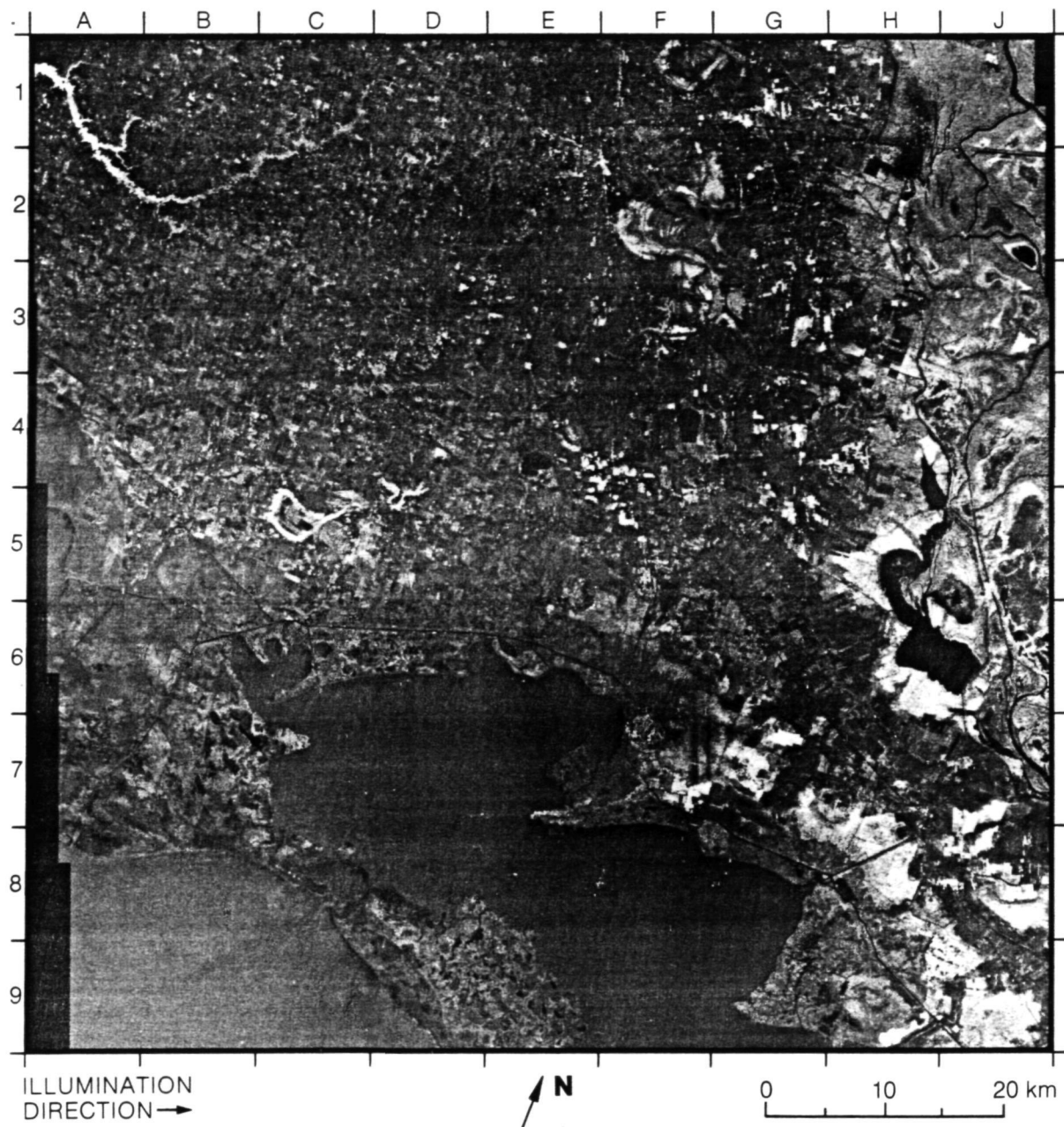
This scene of the Louisiana coast is located approximately 185 kilometers west of New Orleans. The image shows three major types of land cover. Coastal wetlands of Marsh Island (E9), Belle Isle (B7) and areas surrounding Vermilion Bay (D7), and West Cote Blanche Bay (F8) occur in the south. These areas of very low elevation (less than 2 meters) are designated as marsh and swamp on the U.S. Geological Survey 1:250,000 topographic sheet. The eastern portion of the image shows the Atchafalaya Basin Floodway. Lake Fausse Pointe (H4 to H6) is easily defined at the western edge of this zone. The entire zone is characterized by bright returns that coincide very closely with the areas of marsh-swamp on the U.S. Geological Survey 1:250,000 maps that are shown by

Legend:
- POPULATED AREAS
- RIVERS
- OPEN WATER
- INTRACOASTAL WATERWAY
- N
- 0 10 20 km
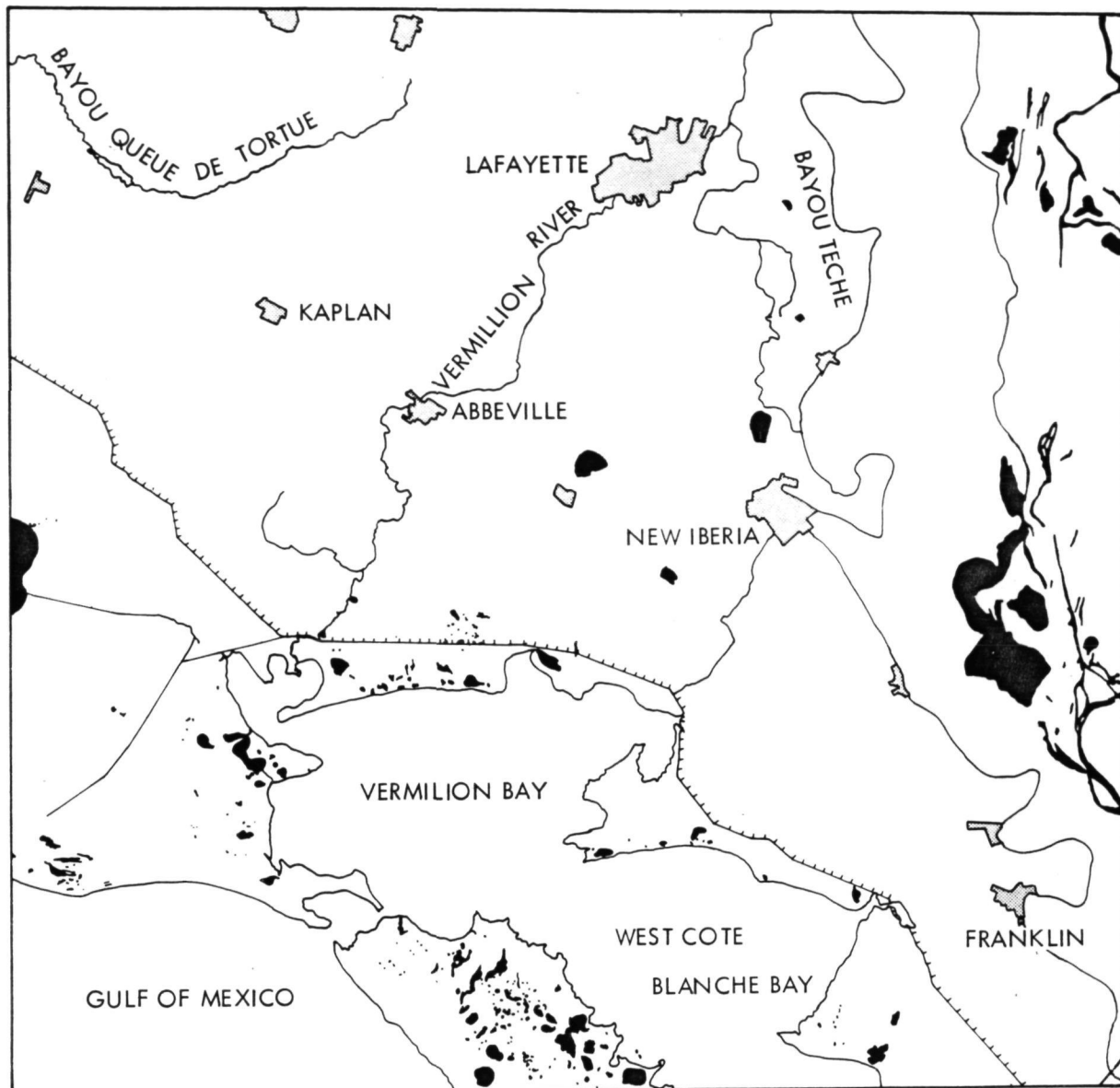
a green ("woods-brushwood") overprint. The same relationship of bright radar returns and woods-brushwood overprint on U.S. Geological Survey maps of the 1:250,000 series is noted on the Denver, Colorado, image in this atlas.

The northwest quarter of the present image consists of fairly well-drained uplands, with elevations up to 10 meters. The woodland along the rivers (e.g., Bayou Queue de Tortue, B2) appears bright as do the wooded areas of the Little Bayou (C5). Cultural features such as the intracoastal waterway, oil rigs (F8 in West Cote Blanche Bay), urban areas (Lafayette, New Iberia), and levees (J6 south from Lake Fausse Pointe) are also recognizable.

(Seasat image from Rev. 795.)

30. Lower Chesapeake Bay, Virginia

ILLUMINATION
DIRECTION→

N

0   10   20 km
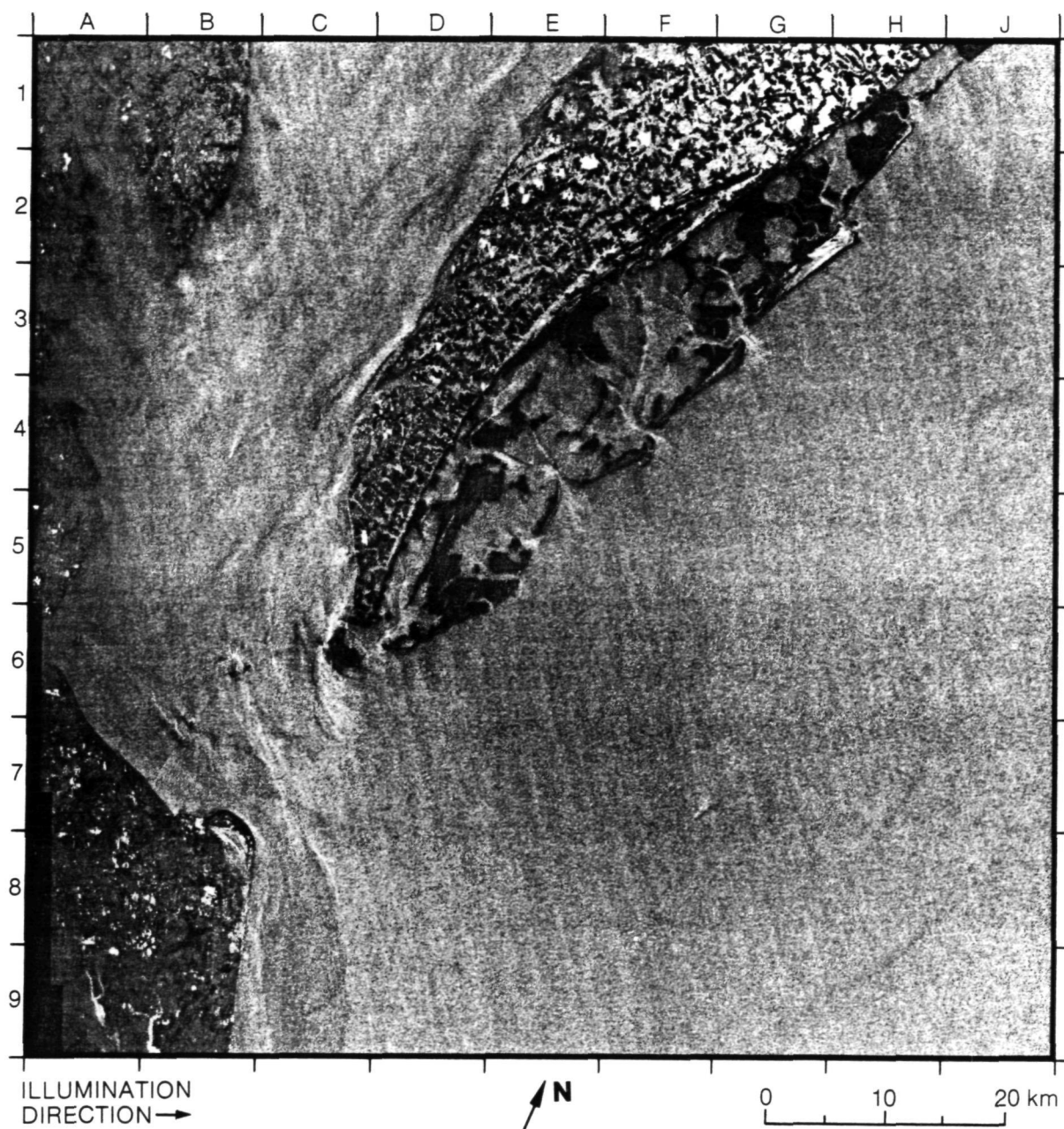
There is a sharp boundary between the marshy tidal flats on the east side of the peninsula, and the more elevated land to the west. The marsh-water interface is also clearly visible. Marshy areas have very flat surfaces and appear black on the radar image. Open water has a wavy surface that returns a higher portion of the radar signal.

CHESAPEAKE BAY

HOG ISLAND BAY

CAPE CHARLES

ATLANTIC OCEAN

CAPE HENRY

N

0   10   20 km
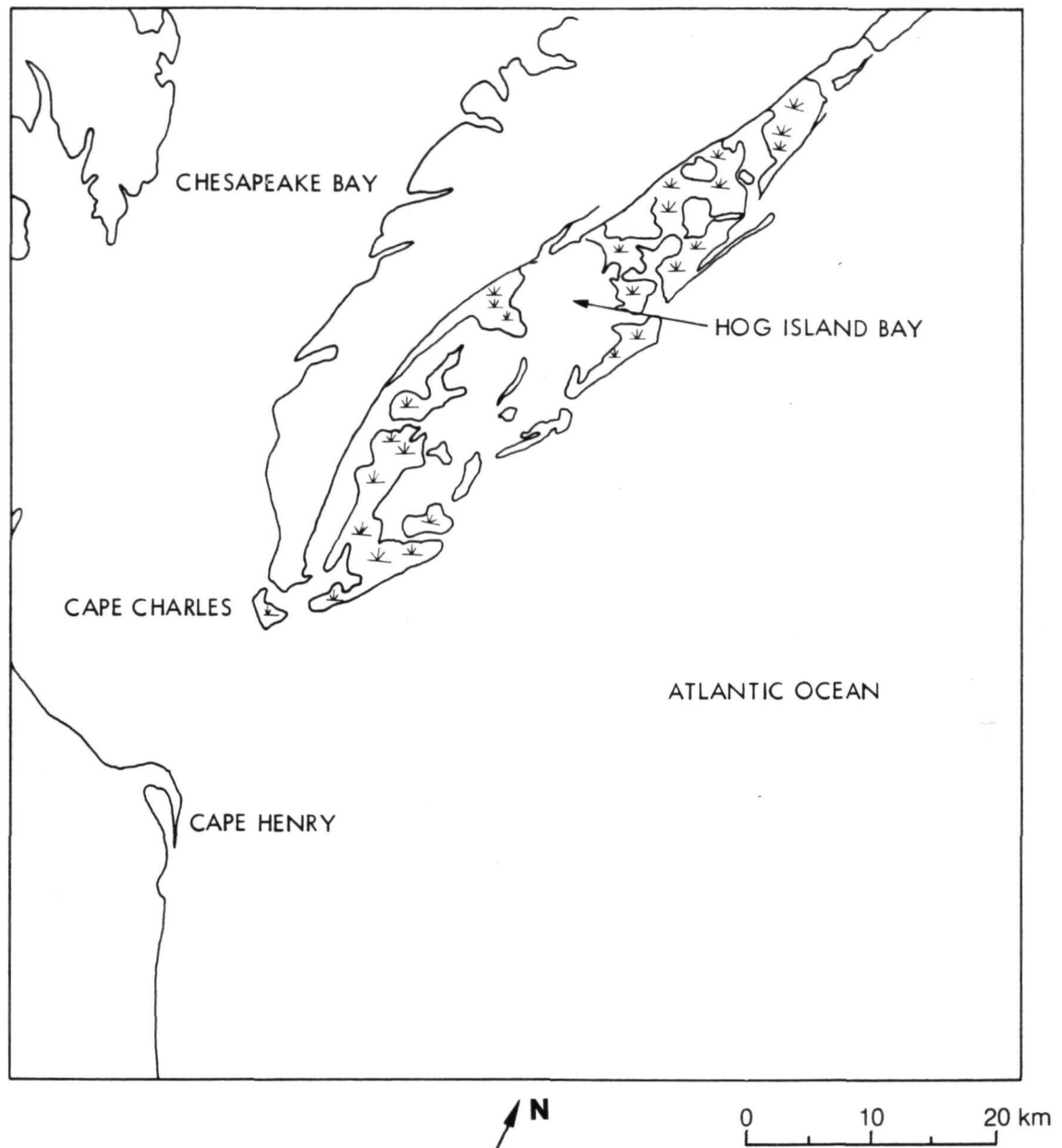
Radar is a powerful tool for mapping the subtle land-water interface in tidal wetlands. Such areas are critical to the overall productivity of the continental shelf, since many fish and fowl occupy them during important stages of their life cycle.

(Seasat image from Rev. 1468.)

(xii) Glaciers

31. Mount McKinley National Park, Alaska

ILLUMINATION DIRECTION ⟶

↗N

0   10   20 km
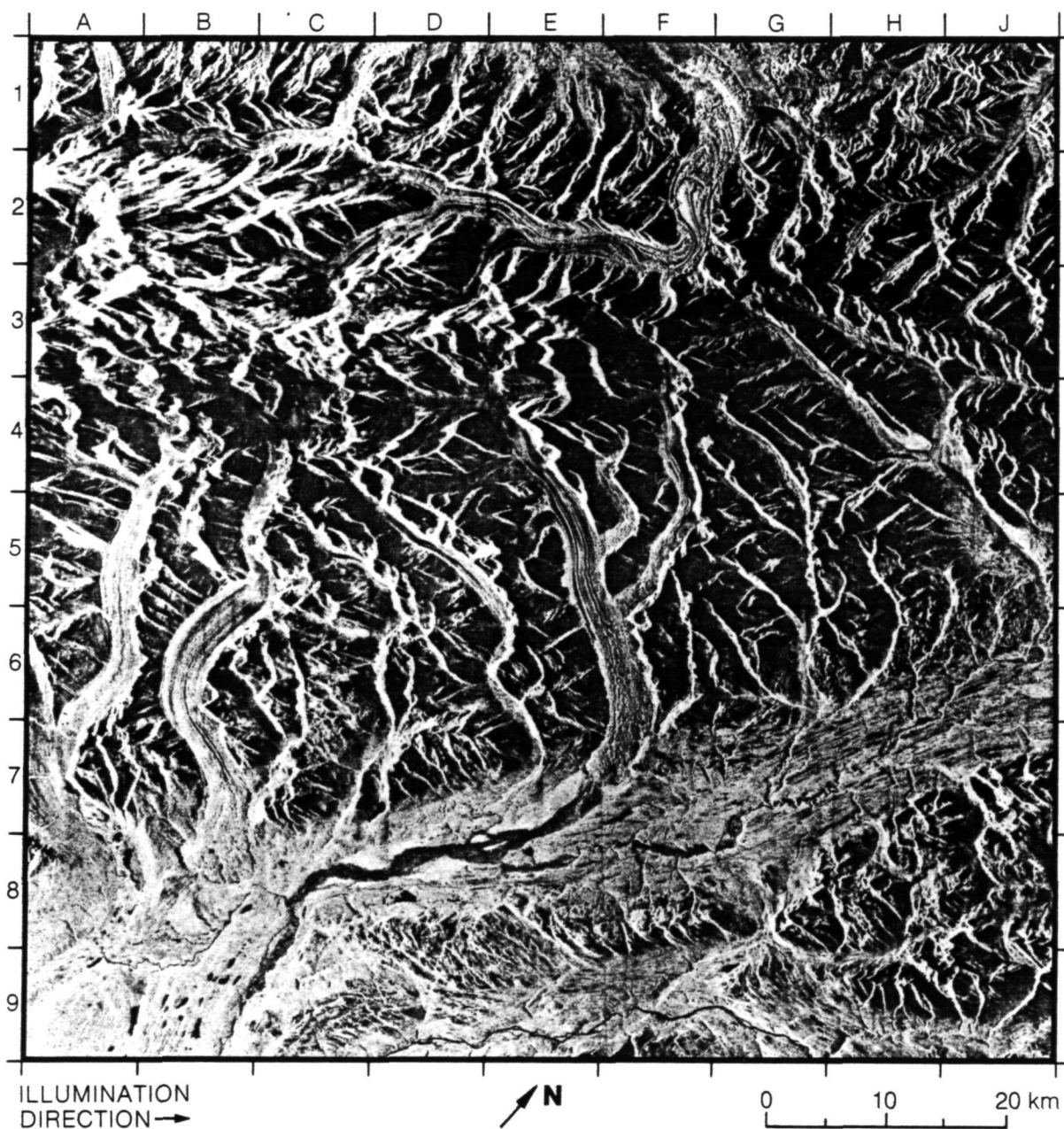
The rugged Alaska Range shown in this image contains the loftiest peaks in North America, including Mount McKinley (B2), which reaches the highest elevation in the range (6194 meters). The mountains are glaciated and largely snow-covered. Alternating light and dark stripes seen on many of the glaciers represent accumulations of broken rock that form moraines along the length of the glaciers as they move. Glaciers such as the Ruth (B5 to B7) flow at uniform rates of a few centimeters per day, and the moraines are relatively straight and uniform. Glaciers such as the Tokositna (A5 to A6) alternate between periods of stagnation that last up to 50 years, and periods of extremely high flow rates over 1 meter per hour that last from 1 to 3 years. The surges produce wavy folded patterns along the moraines at the surface.

Geometric distortion due to layover causes some of the steep mountains to be so strongly displaced toward the near range of the radar image that they

MULDROW GLACIER

△
MOUNT
McKINLEY
(6194 m)

DENALI
FAULT

BUCKSKIN GLACIER

ELDRIDGE GLACIER

TOKOSITNA GLACIER

GLACIER

RUTH

CHULITNA RIVER

RIVER

SUSITNA RIVER

↗N

0   10   20 km
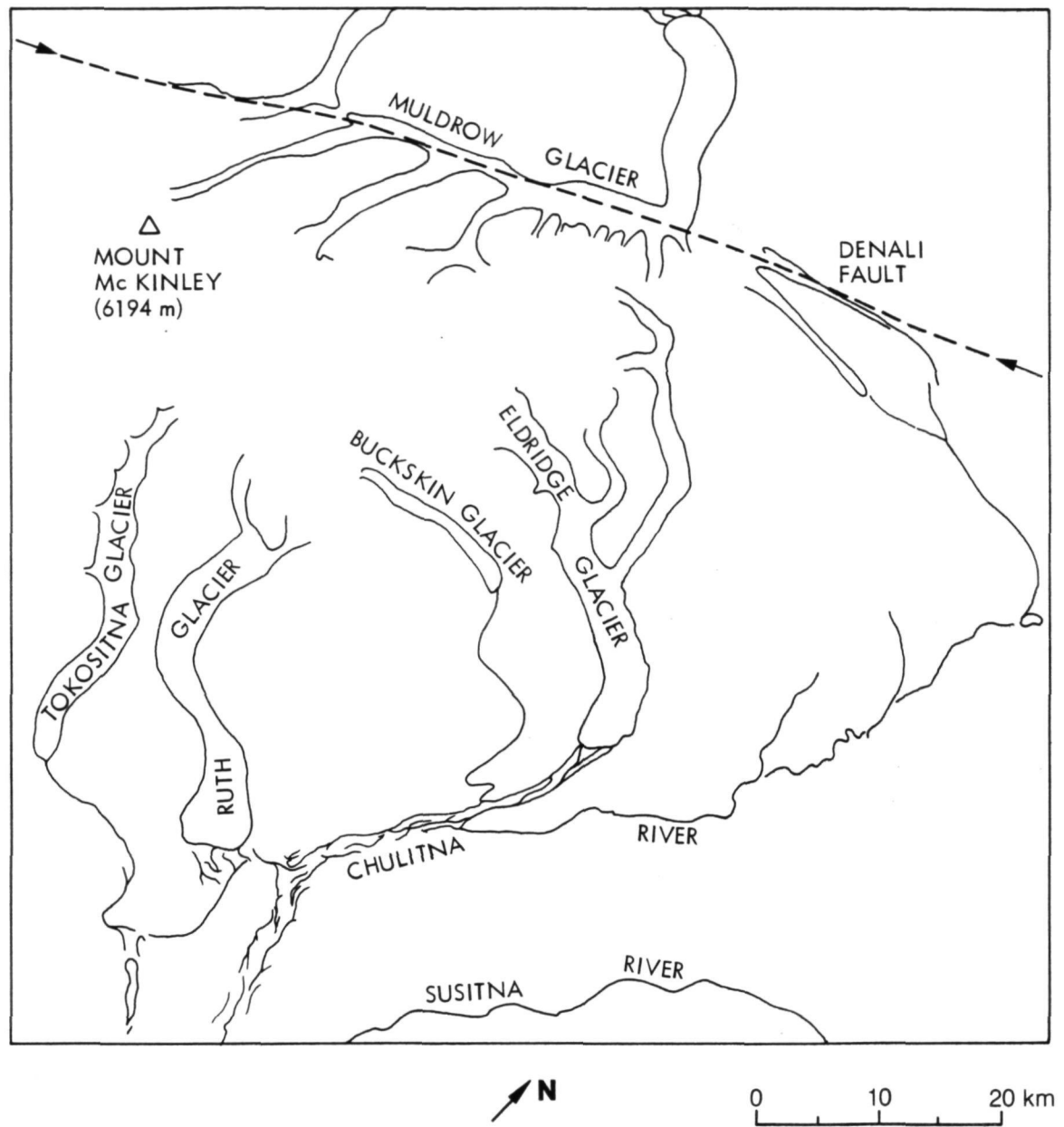
appear to be superimposed on the glaciers. A notable example of this is in the Ruth Glacier at B6 where a bright return from a single peak is displaced almost one third of the way across the glacier. Finely braided streams at the terminus of the Muldrow Glacier (F1), and the Eldridge Glacier (E7) yield low radar backscatter and appear dark on the image.

The trace of the Denali Fault extends across the image from A1 to J4. The Denali Fault is presently active in southern Alaska, producing earthquakes frequently. The Muldrow Glacier follows the Denali Fault from D1 to F2, where it makes an abrupt right-angle bend northwestward, away from the fault trace.

(Seasat image from Rev. 380.)

32. Godthåbsfjord-Isua Region, Southern West Greenland
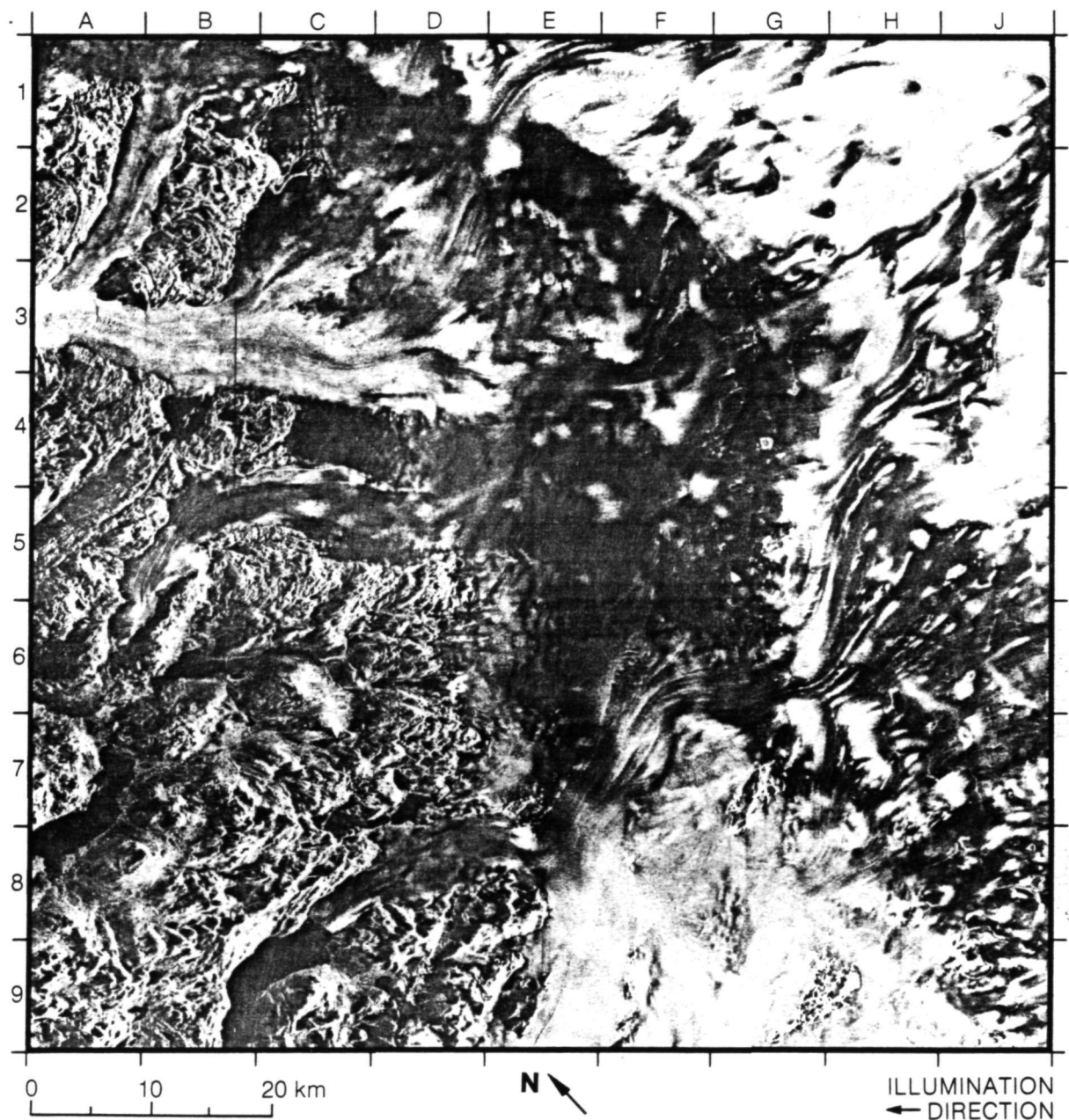
This scene in southern west Greenland is about 60 kilometers from the coast at Godthåb, and about 60 kilometers south of Isua. It depicts the boundary between inland ice of the Greenland icecap to the east, and exposures of very ancient rocks in coastal and near-coastal areas to the west. The rocks are mostly a complex of granodioritic gneiss. Rocks from the Isua area have yielded a radiometric age of approximately 3700 million years, and thus they represent the oldest supracrustal sequence known on Earth.
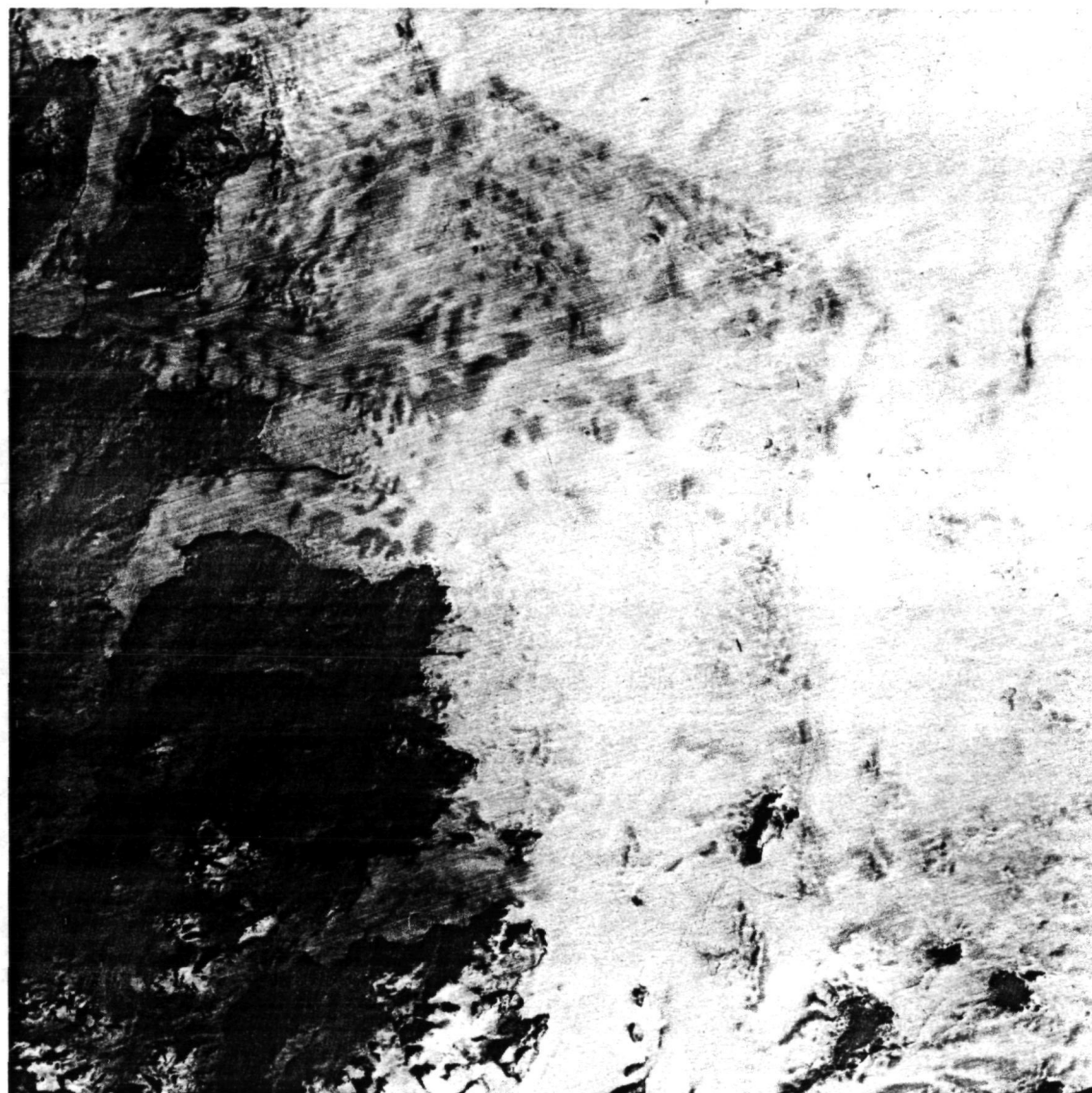
N ↖   0   10   20 km

The Seasat radar image clearly shows flow patterns in the ice. The flow patterns are conspicuous where the ice passes from the icecap into valley glaciers and fjords (e.g., from E1 to A3, and from J4 to C8). Several bare-rock promontories (nunataks) that project through the ice in the lower right of the image are more clearly distinguished from surrounding ice on the Landsat image above.

(Seasat image from Rev. 1490; Landsat scene ID: 1448-14124.)

C. Urban Landcover

33. The Nation's Capital

The physical geography of the Potomac River (flowing southward from A4 to F9) and the Anacostia River (junction with the Potomac at E6) dominates this scene. Two large structures, the Pentagon (D6) and the R. F. Kennedy Stadium (F4), are easily identified primarily because of the strong returns that outline their distinctive shapes. (Compare, for example, with the Dodger Stadium at C5 on the Los Angeles (II) image.) Several large features including Andrews Air Force Base (AAFB, J5) and the Washington National Airport (WNA, E6) are conspicuous because of the nearly specular reflections of the radar signal. East Potomac Park, the knife-shaped island at the junction of the Potomac and Anacostia Rivers (E5), the adjacent tidal pool, and the area across the river and surrounding the Pentagon also produce very low radar returns, due primarily to the relatively smooth surfaces. However, they can be distinguished from the smooth waters of the rivers. The Beltway (Highway I-495) that surrounds the

BALTIMORE – WASHINGTON PARKWAY

Mc MILLAN RESERVOIR

DALECARLIA RESERVOIR

MALL

GEORGETOWN RESERVOIR

SUITLAND PARKWAY

AAFB

WNA

LAKE BARCROFT

POTOMAC RIVER

I-495
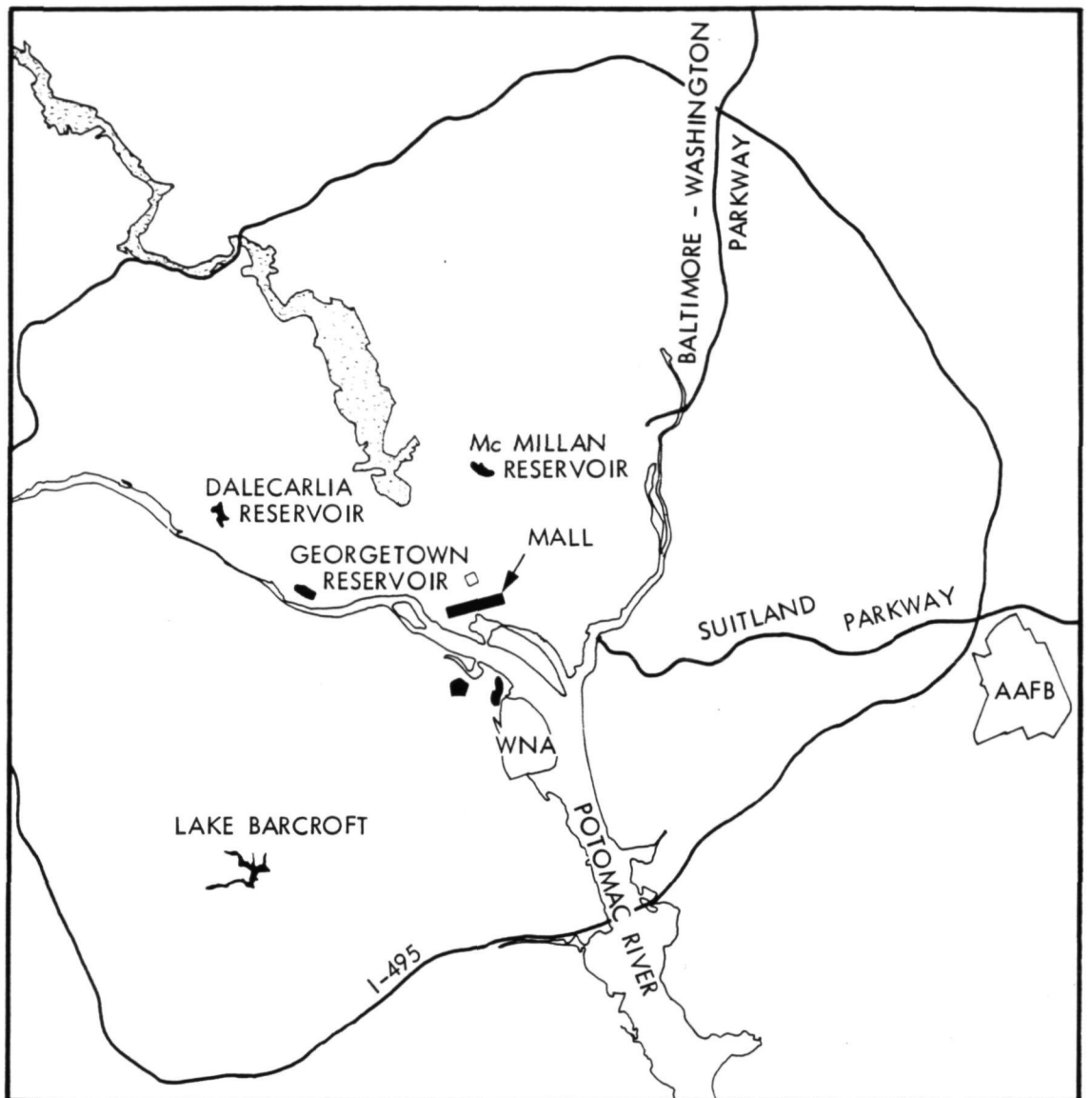
Symbol	Legend	Symbol	Legend
🐾	OPEN WATER	———	MAJOR HIGHWAYS
▨	IMPROVED OPEN SPACE	☐	WHITE HOUSE
		⬟	PENTAGON

0   5   10 km

N

entire urban area can be traced except for the small western portion that was not within the radar swath. Similarly, other major routes for vehicular traffic (e.g., the Suitland Parkway) can be traced. Within the improved open space (Rock Creek Park and the National Zoo to the south), Rock Creek appears very similar to the Suitland Parkway with respect to radar responses. Detailed comparison of this image with maps of Washington, D.C. (U.S. Geological Survey, 1973) helps to identify numerous other features such as the Mall, which consists of an elongated parkway lined with major government buildings. It is identified as an east-west trending dark band in the center of the image. The Capitol is located at the eastern end, Lincoln Memorial at the western end, and the Smithsonian Institute, NASA Headquarters, and the National Art Gallery along the length of the Mall.

(Seasat image from Rev. 558.)

105

34. Los Angeles, California (I)
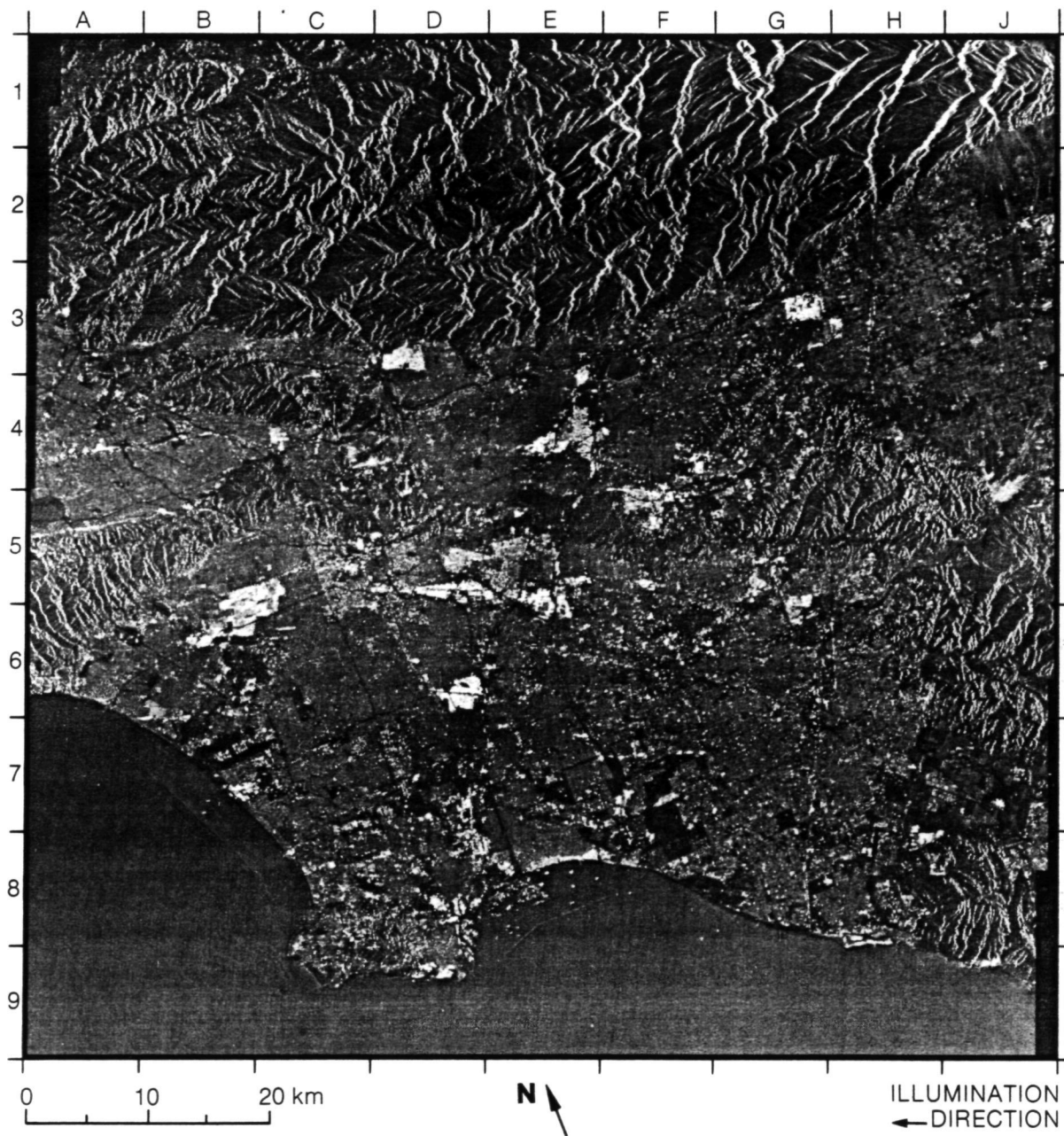
Large areas of very dark tones on the Seasat image are generally smooth (e.g., Los Angeles International Airport at B7, Los Alamitos Naval Weapons Center at F8, Sepulveda Flood Control Basin at A5, and Santa Fe Dam Recreation Area at F4). Topographically rough areas such as the San Gabriel Mountains to the north (A1 to J1, A2 to H2), the Santa Monica Mountains (between Hollywood and the San Fernando Valley at A5 to B5), and the Palos Verdes Hills (C8 to D8) generally have oriented and alternating black and white patterns. Very bright tones that cover several square kilometers occur within the urban areas. The bright tones result generally from the orientation of the buildings and structures relative to the direction of radar illumination.

N↑   0   10   20 km

Examples in Altadena (D3), western Los Angeles (B5), Lynwood (D6), and LaVerne (G3) are easily seen. On the Landsat image, the problems of building orientation are not encountered. Major marina (Marina Del Rey, B7) and harbor facilities (San Pedro Harbor, E8) seen on the Landsat image show additional details on the Seasat image. The bright areas along the shore in the Landsat scene are the sand beaches, whereas on the Seasat image such beaches are generally dark. The brightness of the near-beach area in southern Long Beach and Belmont Shore (E8) is the result of building orientation relative to the direction of radar illumination.

   (Seasat image from Rev. 660; Landsat scene ID: 1090-18012.)

35. Los Angeles, California (II)

ILLUMINATION DIRECTION →

↑ N

0   10   20 km
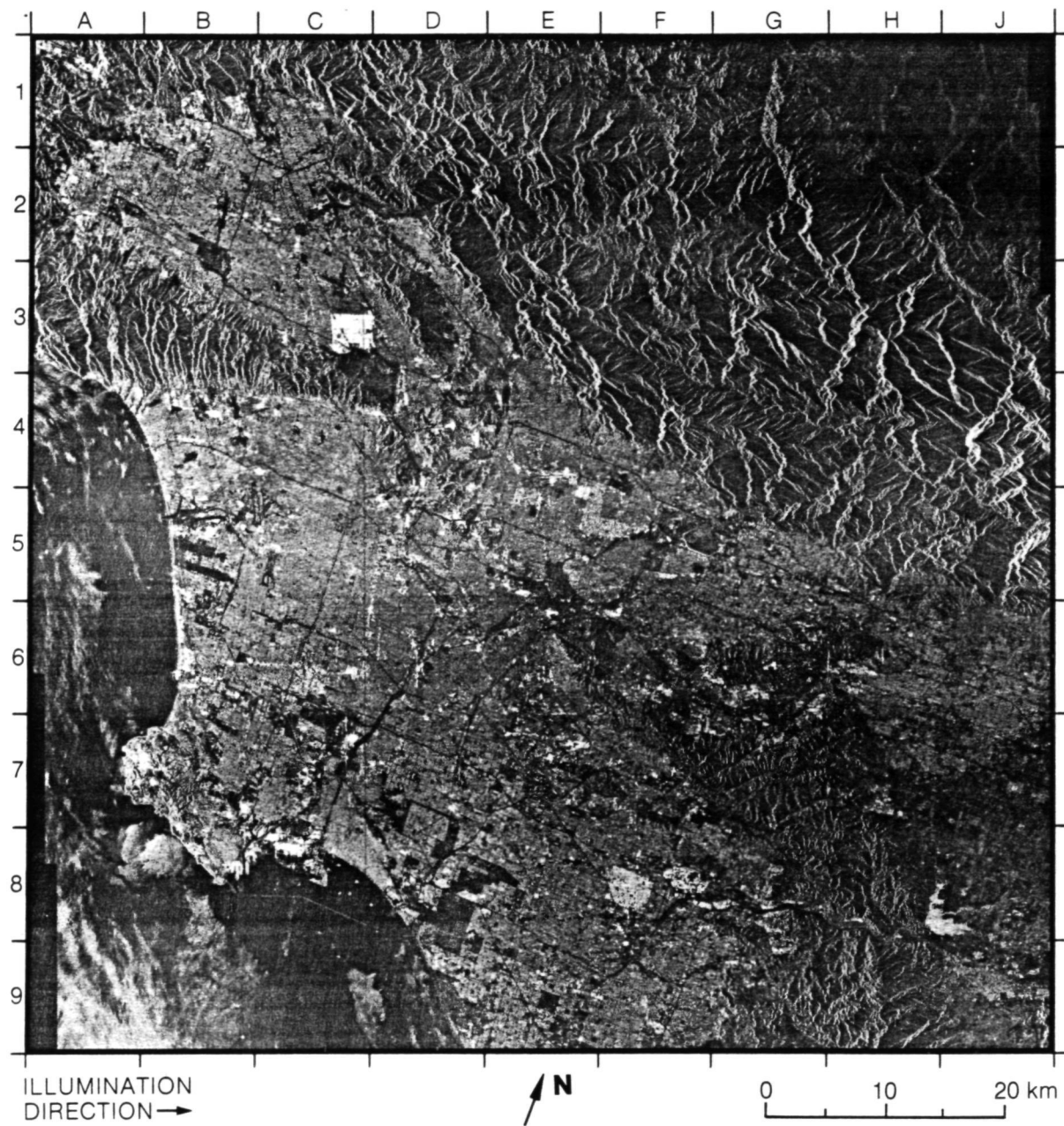
This image covers essentially the same geographical area as that shown on Los Angeles (I), though it is viewed from a different look direction. Comparing the two Seasat images of Los Angeles, it is evident that areas of bright returns do not correspond where the brightness is dependent on the radar look direction, while certain areas of low backscatter are common to both images. Part of the City of Burbank (C3) forms an excellent example of the first instance. It appears bright on this image, but shows no differentiation from the surrounding area on the Los Angeles (I) image (B4). A corresponding relationship occurs in part of Altadena, which appears bright on the Los Angeles (I) image (D3), but is undifferentiated on this image (E3). In the second instance, areas of low backscatter that are common to both Seasat images include the Los Angeles International Airport (B5), Los Alamitos Naval Air Station (D8), and the Sepulveda Flood Control Basin (B2).
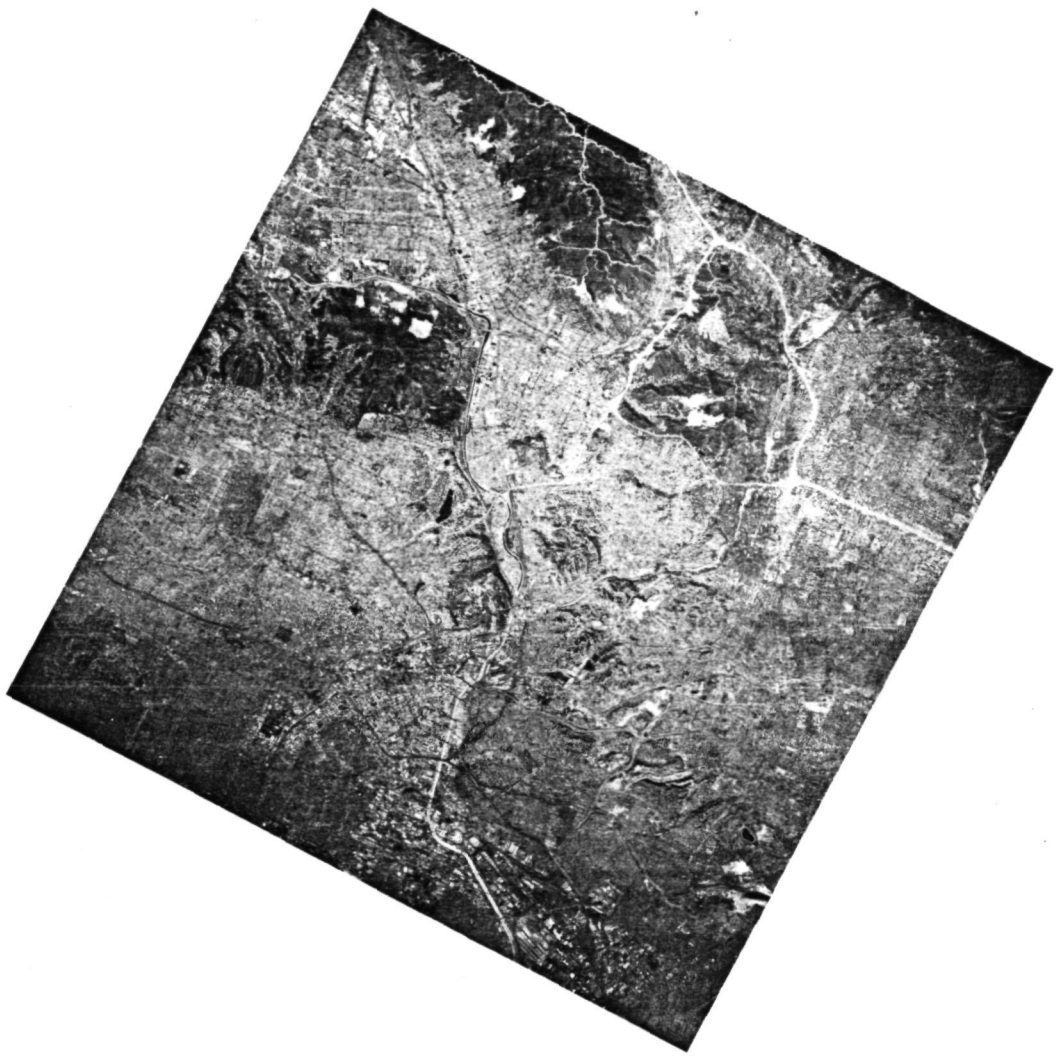
N   0   5   10 km

The aerial photograph above, obtained at approximately 18,000 meters altitude, presents more detail of the area between Burbank (C3), Pasadena (E4), and Los Angeles (C5). On the aerial photo a distinction can be made between rivers that contain water (dark) and rivers that are dry (light). Freeways are generally light in tone and may be confused with dry river beds. Although freeways are commonly identifiable on the radar imagery, they appear quite similar to the rivers that are channeled in concrete.

The dark area in the center of the aerial photo is Silver Lake, located at D4 on the Seasat image.

(Seasat image from Rev. 351.)

36. Denver, Colorado

ILLUMINATION DIRECTION →

N

0   10   20 km
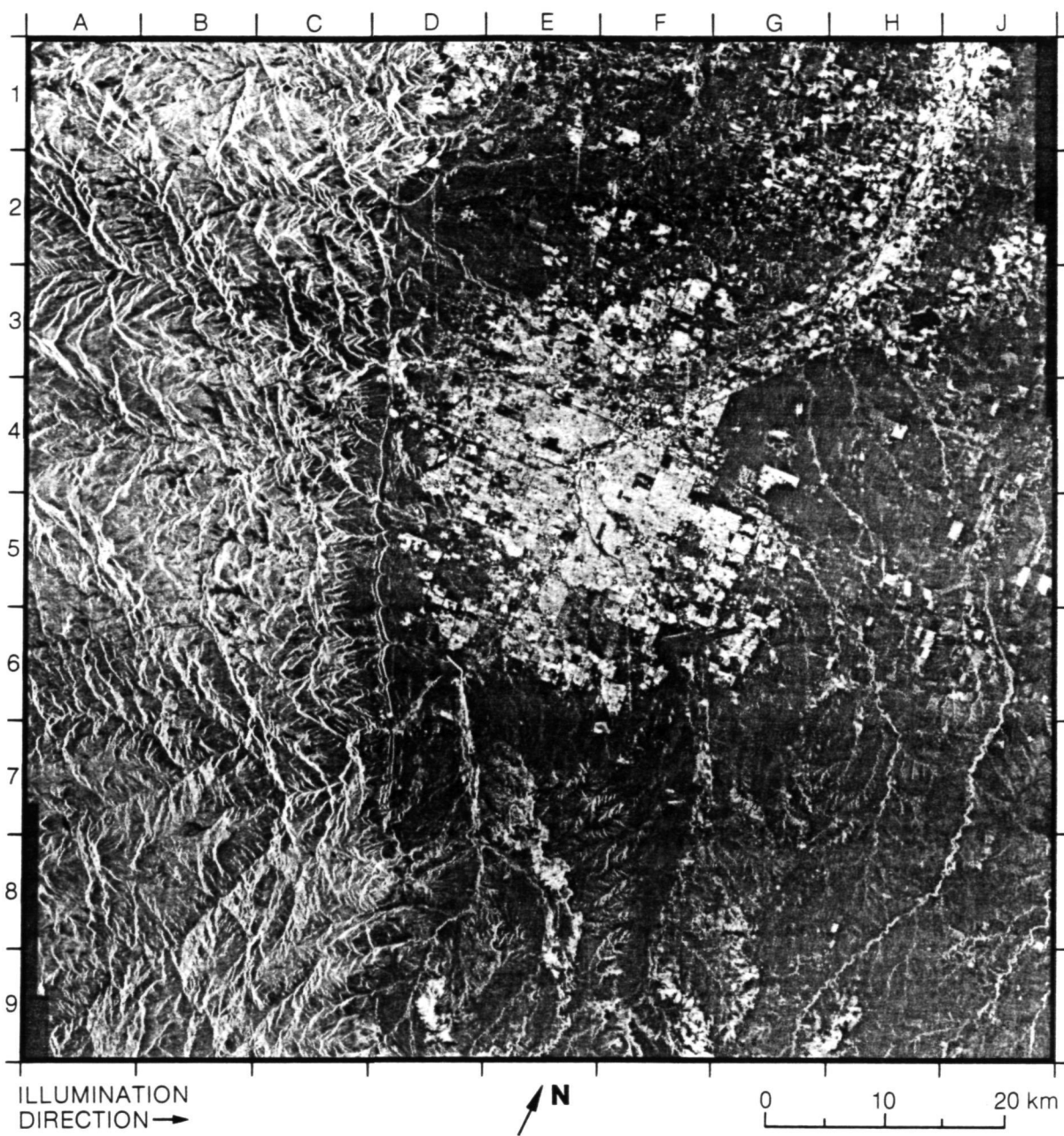
The 1978 revision of the 1:250,000 map (U.S. Geological Survey) of this scene coincides closely with the time of collection of the Seasat SAR data. Centered approximately in the neighborhood of Englewood (a suburb of Denver), Colorado, the scene is the subject of a recent urban mapping study by Henderson, et al. (1980). The Front Range of the Rocky Mountains dominates the entire western one-third of the image. At the eastern edge of the Front Range (trending from B1 to C9) a series of hogbacks that are aligned roughly parallel to the ground track of the satellite appear as a set of bright, crenulated double lines. Within the eastern two-thirds of the image, the City of Denver and environs present the characteristic gray tones displayed by such urban scenes. Of special interest, however, are several linear features that are conspicuous, as are the hogbacks, because of their orientation rather than their size. Bright linear features include a power line (D2), a section of Interstate Highway I-25

LAKES, RESERVOIRS   --------- POWER LINE

◫◫◫ WOODS-BRUSHWOOD   ═══ RUNWAYS

++++ RAILROADS   ├──┤ CANAL

── MAJOR HIGHWAY   ～～ INTERMITTENT STREAM

0   10   20 km

N
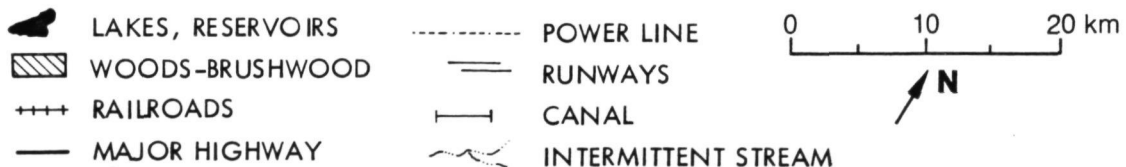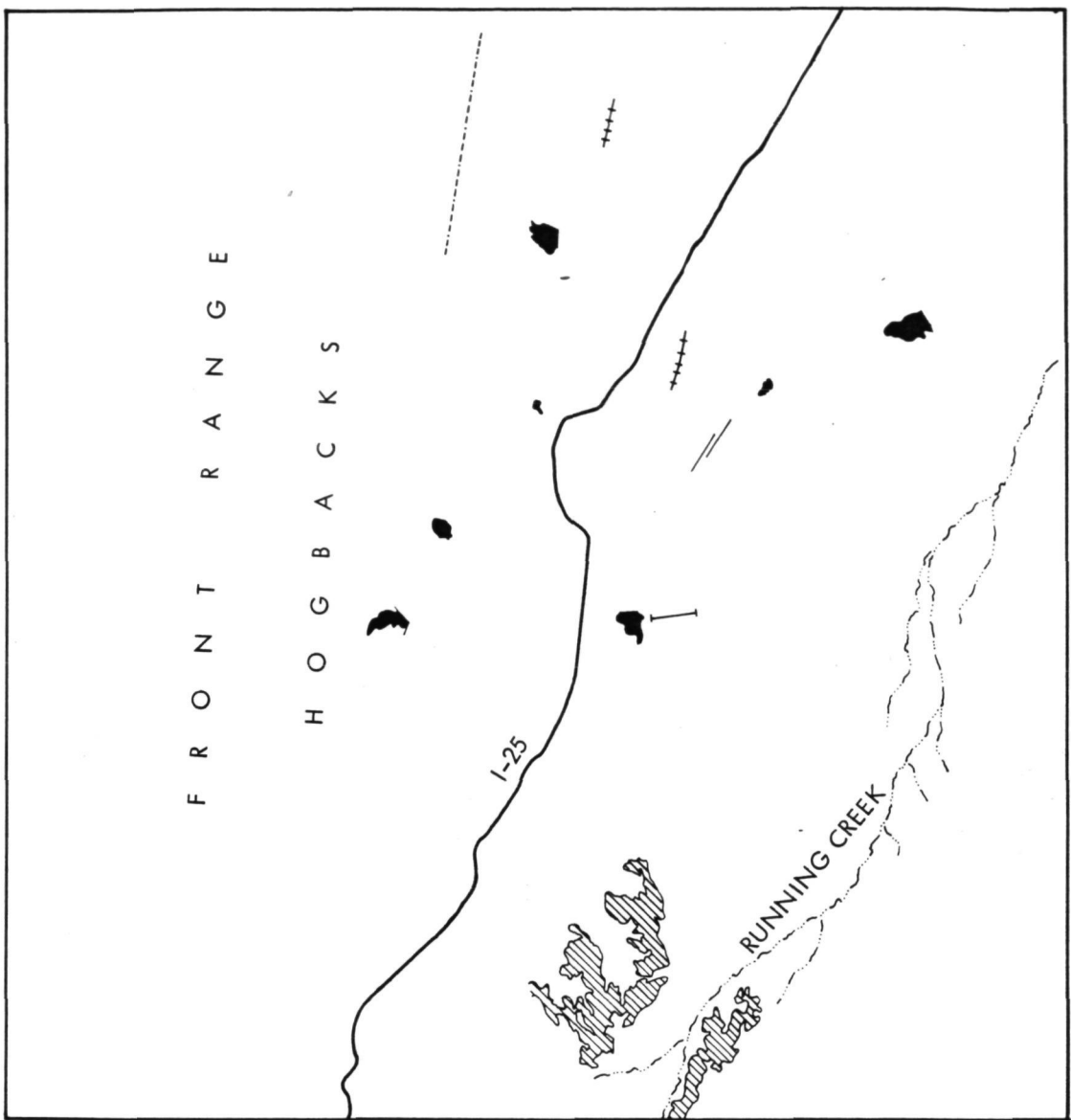
(F6), portions of a railroad track (E2 and F3), and lake dams (D6). Other linear features of cultural origin, such as the runways at Stapleton International Airport (G4) and a canal (F6) produce very low returns. Numerous areal features of low return include several lakes (e.g., G4 and E4), city parks (F4) and cemeteries (E4). The course of the South Platte River, northward from Denver, is easily traced primarily because of the transportation, urban, and agricultural development that follow its route. Other more intermittent water courses (e.g., Running Creek at G9 to J5) are identified primarily because of the riparian vegetation. There is a relatively high correlation between the bright returns at the southern end of the image with the areas identified as "woods-brushwood" on the revised U.S. Geological Survey map (1974).

(Seasat image from Rev. 580.)

111

37. New Orleans, Louisiana
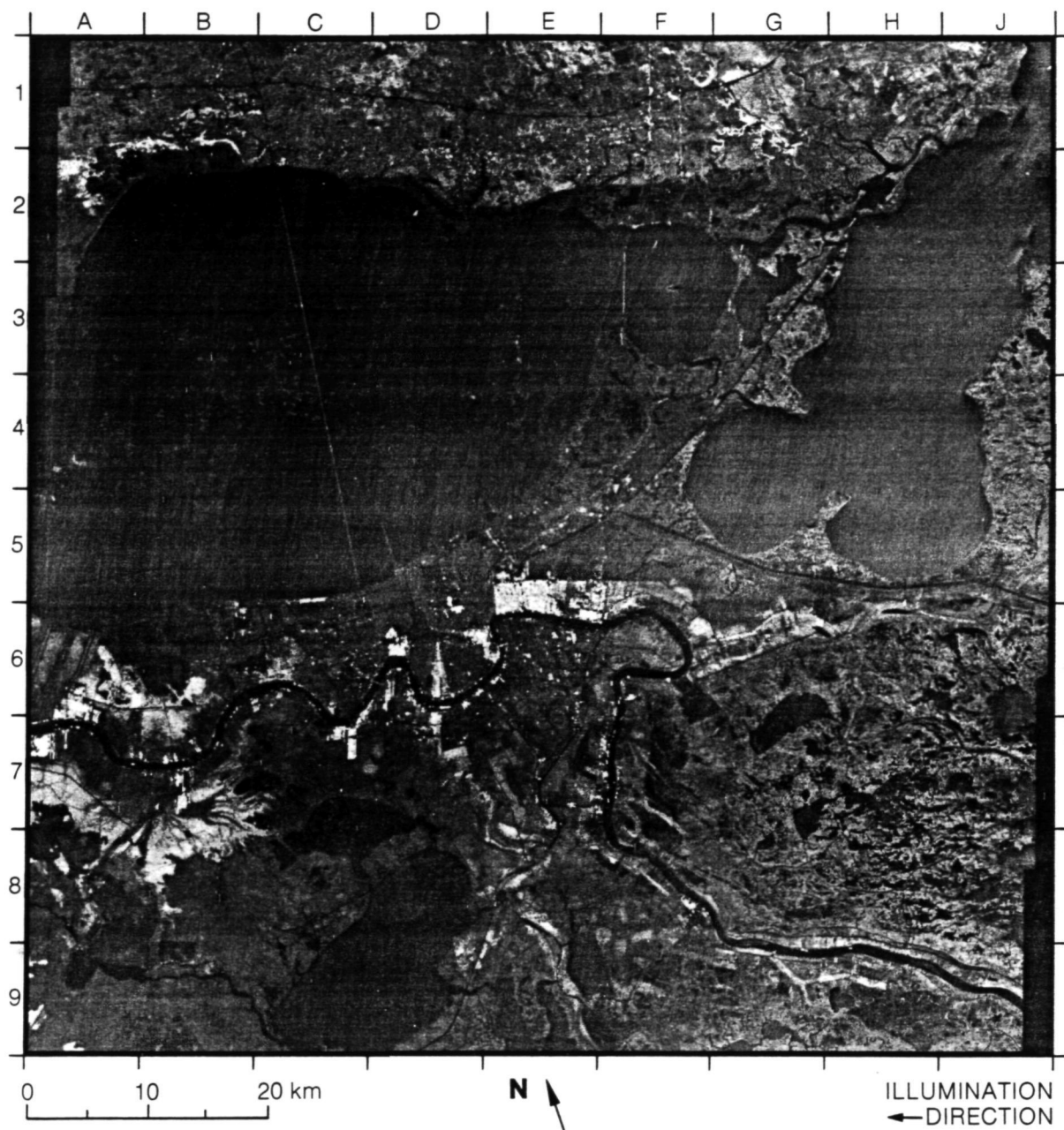
The two radar images shown here were acquired from different look directions. The effect of the look direction on the radar return is seen by comparing the Arabi area (E5 on the left and E7 on the right) and the several causeways across the eastern end of Lake Pontchartrain (F3 on the left and G5 on the right). Both Lake Pontchartrain and Lake Borgne (H3 on the left and H7 on the right) appear similar on the two images because of the general smoothness of the lake surfaces. However, some variations occur due to wave structure (compare with the Salton Sea on the Imperial Valley, California, image). On the right Seasat image, the Matairie area, adjacent to the southern

ILLUMINATION
DIRECTION→

N

0   10   20 km
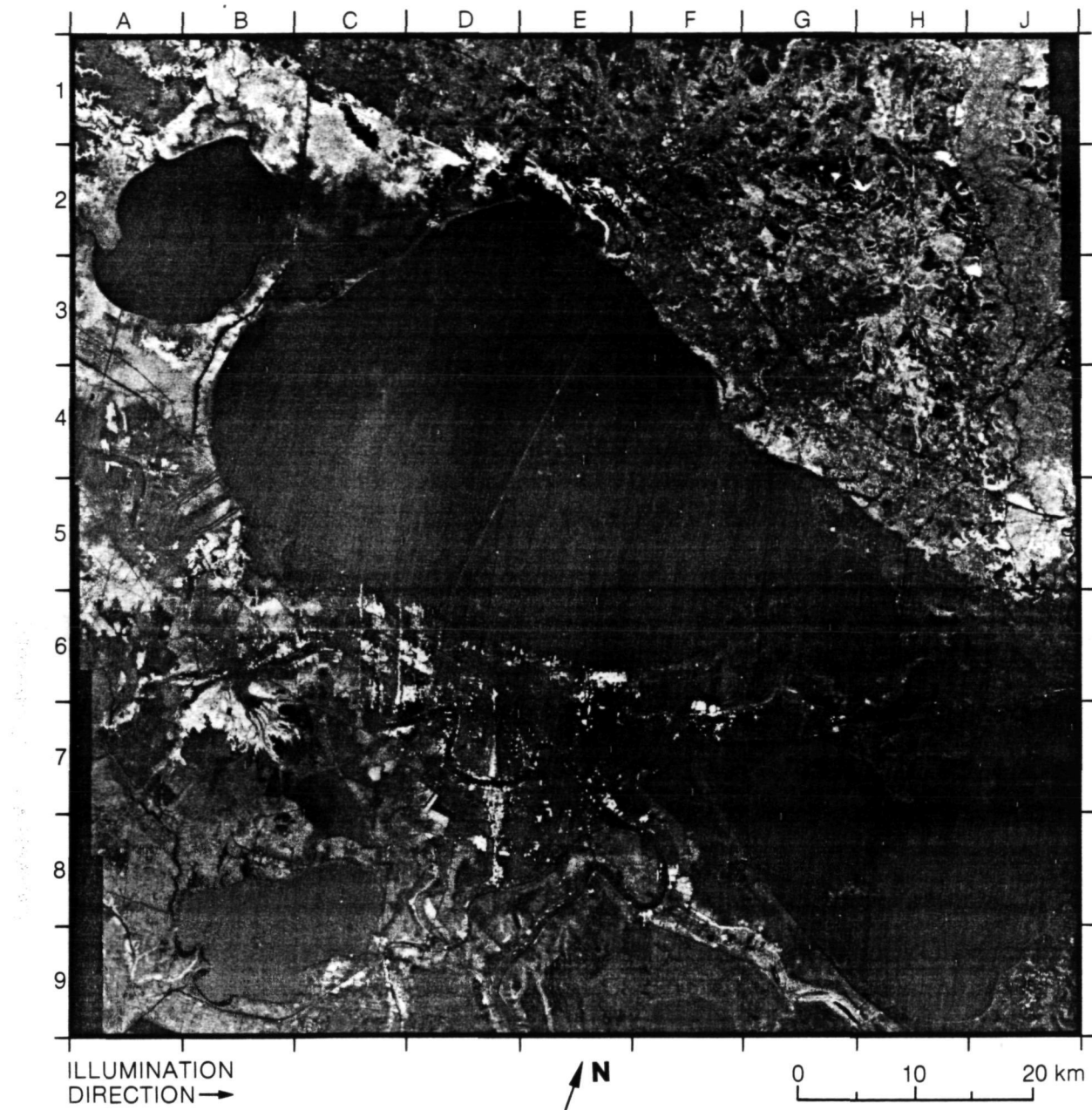
terminus of the Lake Pontchartrain Causeway (C6), appears twice, with an offset of approximately 4 kilometers. This type of offset occasionally appears due to an STC change at the time of image acquisition. A more subtle processing defect occurs on this image in the form of a small square approximately 18 kilometers on a side, with its northern edge between D6 and F6. This occurred because the data are digitally correlated in small sections and recombined to form the entire image.

(Left Seasat image from Rev. 788; right Seasat image from Rev. 838.)

38. Geneva, Switzerland

ILLUMINATION
DIRECTION→

N

0   10   20 km
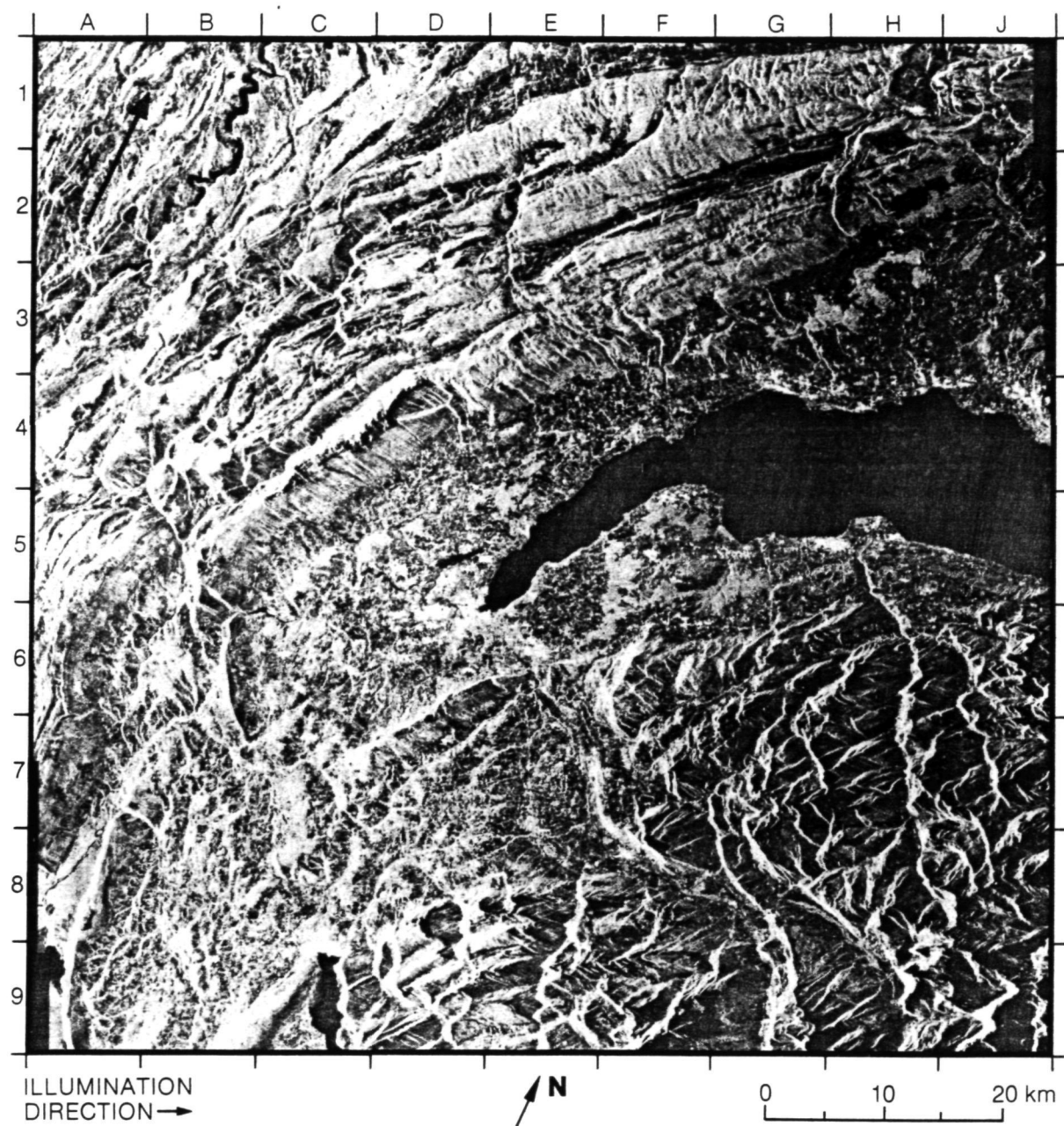
This scene of western Switzerland and the adjacent parts of France shows an interesting combination of different landscapes, with their individual relief characteristics enhanced on the radar image. The upper left part of the image is dominated by the elongated mountain chains of the Jura. They contrast sharply with the different type of relief in the Alps at the lower right. Between these two mountainous areas lies the Geneva basin with the Lake of Geneva extending to the right. Settlements are easily identified along the lakeshore as clusters of bright spots. Since streets and buildings that are oriented perpendicular to the direction of radar illumination reflect a large part of the

TOWN, CITY   ~~ RIVER

LAKE   ---- FREEWAY

AIRPORT

↗ N   0   10   20 km
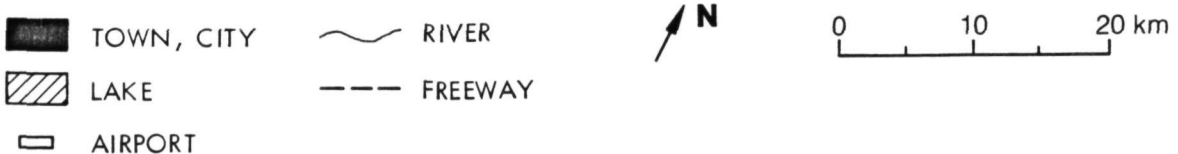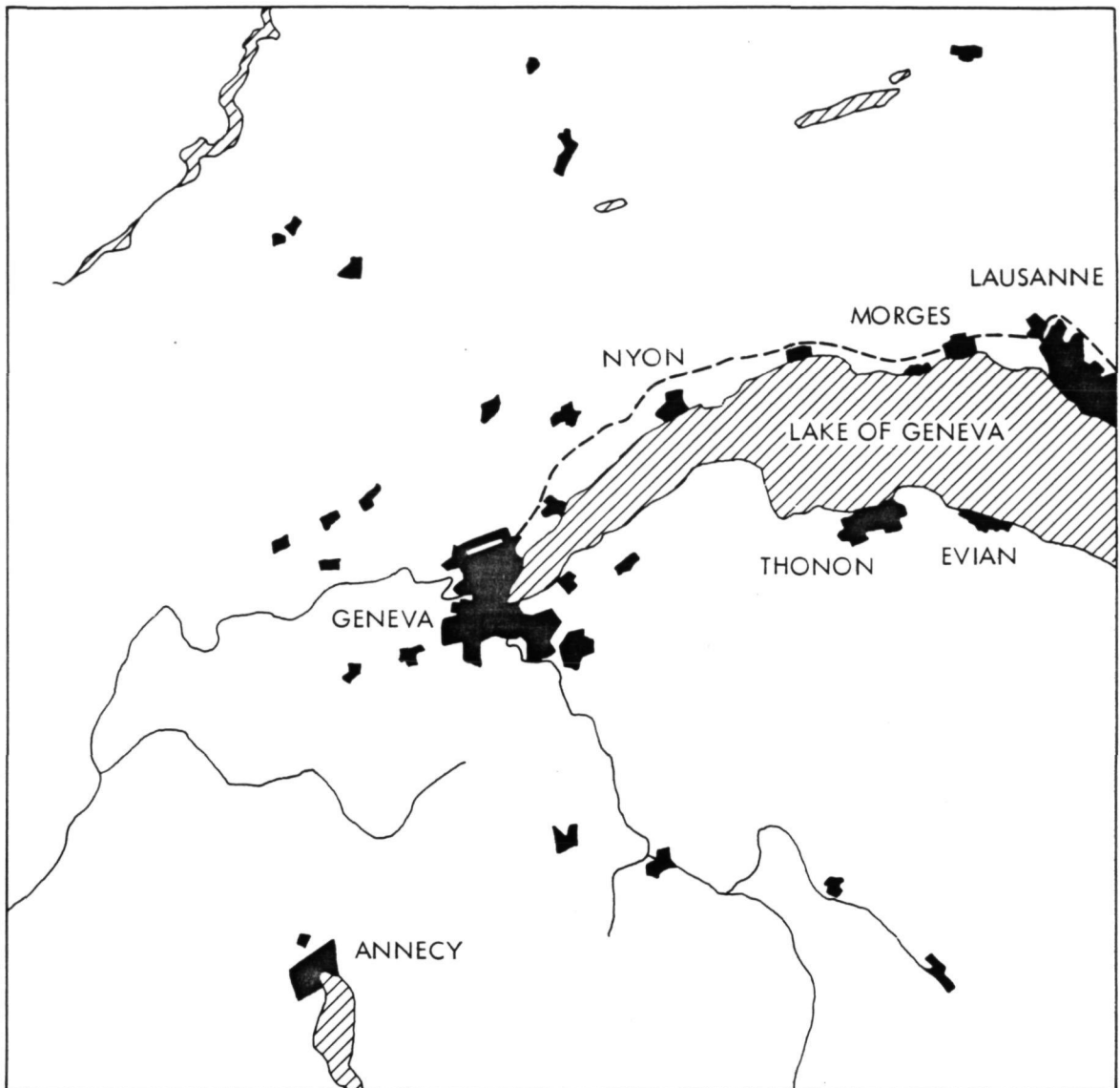
radar signal back to the antenna, and since most settlements have a broad variation of street directions, even relatively small towns and villages may produce bright returns. This effect is seen best, however, in the larger urbanized areas of Geneva (D5 to D6 and E5 to E6) at the lower end of the lake and Lausanne (J4).

(The caption is by courtesy of Dr. Fritz Fasler, Resident Research Associate, Jet Propulsion Laboratory.)

(Seasat image from Rev. 762.)

D. Agriculture

39. Plains of Central Iowa

ILLUMINATION
DIRECTION→

↑ N

0   10   20 km
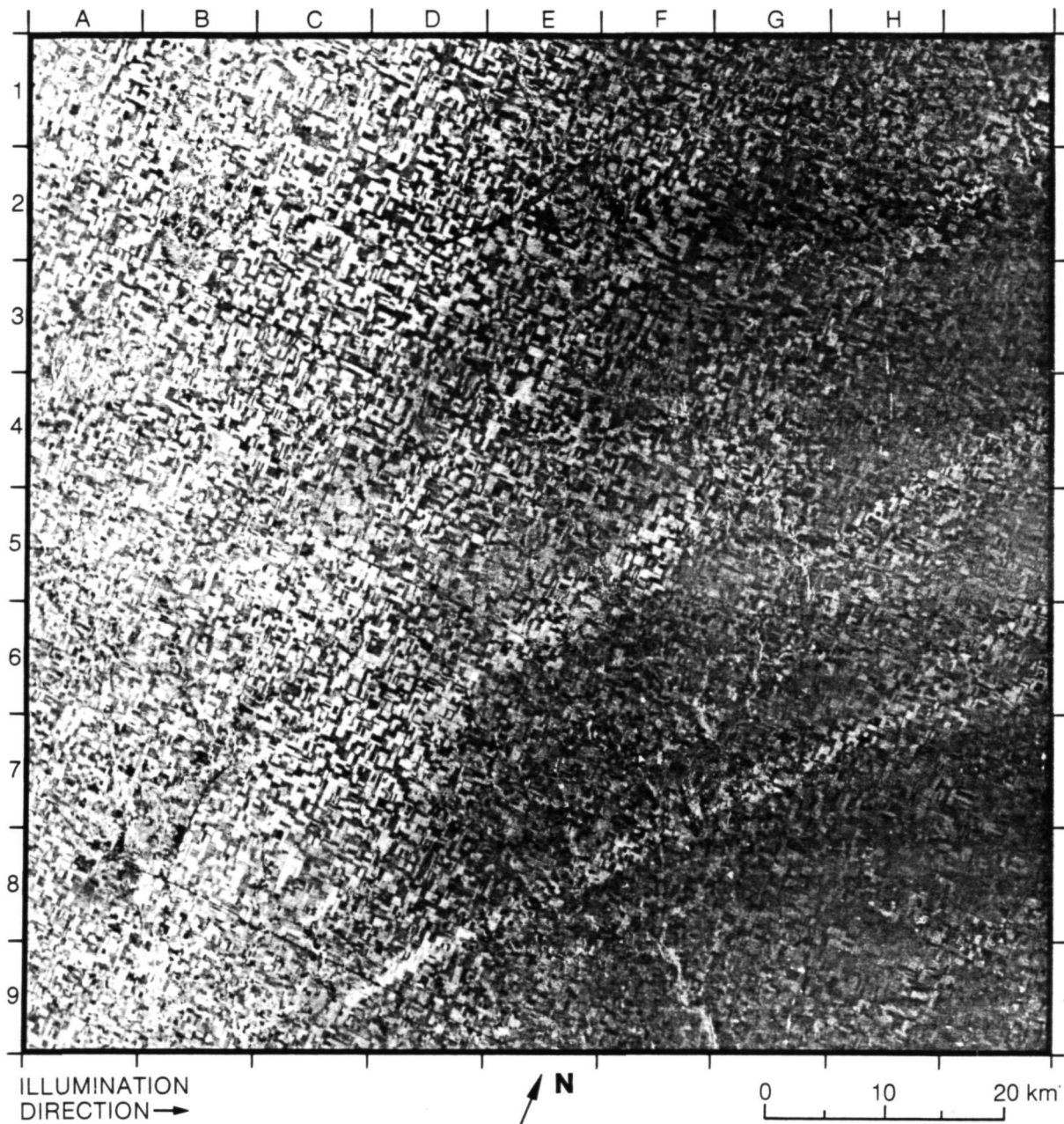
On August 16, 1978, the Seasat satellite passed over central Iowa in the vicinity of Ames (A7) and obtained this image. During the late evening of the previous day, a large frontal storm moved into the vicinity from the west and northwest. Typical midlatitude frontal convective storms occurred for several hours approximately 10 to 12 hours prior to the acquisition of the image. Prior to the passage of the satellite, the storm broke up and several isolated cells moved to the east and northeast, distributing rain along the respective ground tracks. The result is seen in this image where the light areas to the west reflect the general location of the major frontal precipitation activity and the several

118

Legend:
- ■ URBAN AREAS
- ▭ RAINFALL AREAS
- —— HIGHWAYS
- —·—·— INTERMITTENT STREAMS
- ++++ RAILROADS

0   10   20 km

N
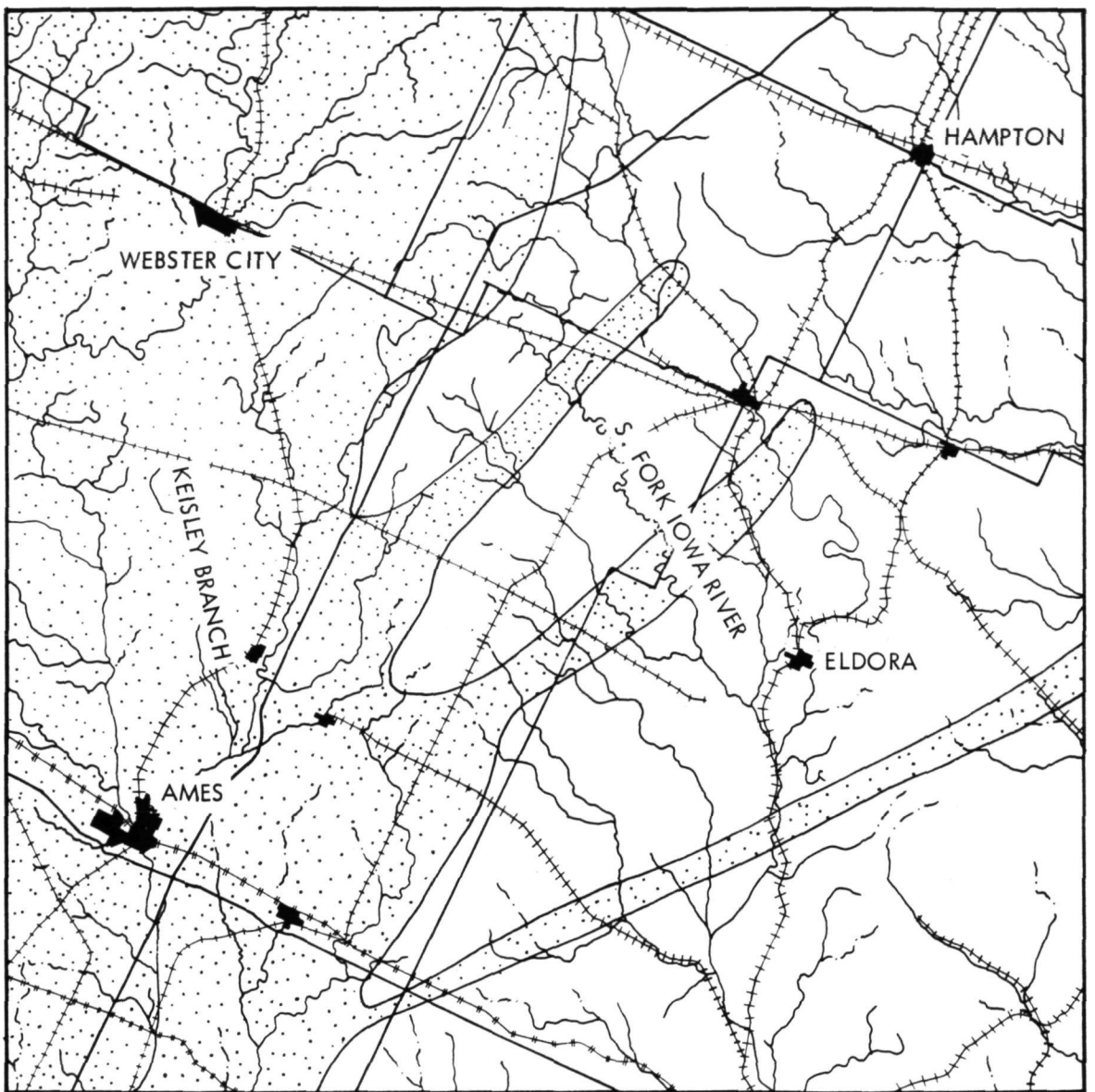
bright paths across the Iowa farmland denote the tracks of the isolated convective rain cells. The several dark areas are those where precipitation was very light or absent. Other items of interest are the patchwork pattern on the rolling topography, which is intensely farmed, and the rough texture of the more steeply inclined and unfarmed river courses (e.g., A3 and G5). Although many railroads crisscross the imaged area, the few that are readily perceptible are those whose orientation parallels the ground track of the satellite (e.g., H4).

(Seasat image from Rev. 723.)

40. Imperial Valley, California

ILLUMINATION
DIRECTION →

N

0   10   20 km
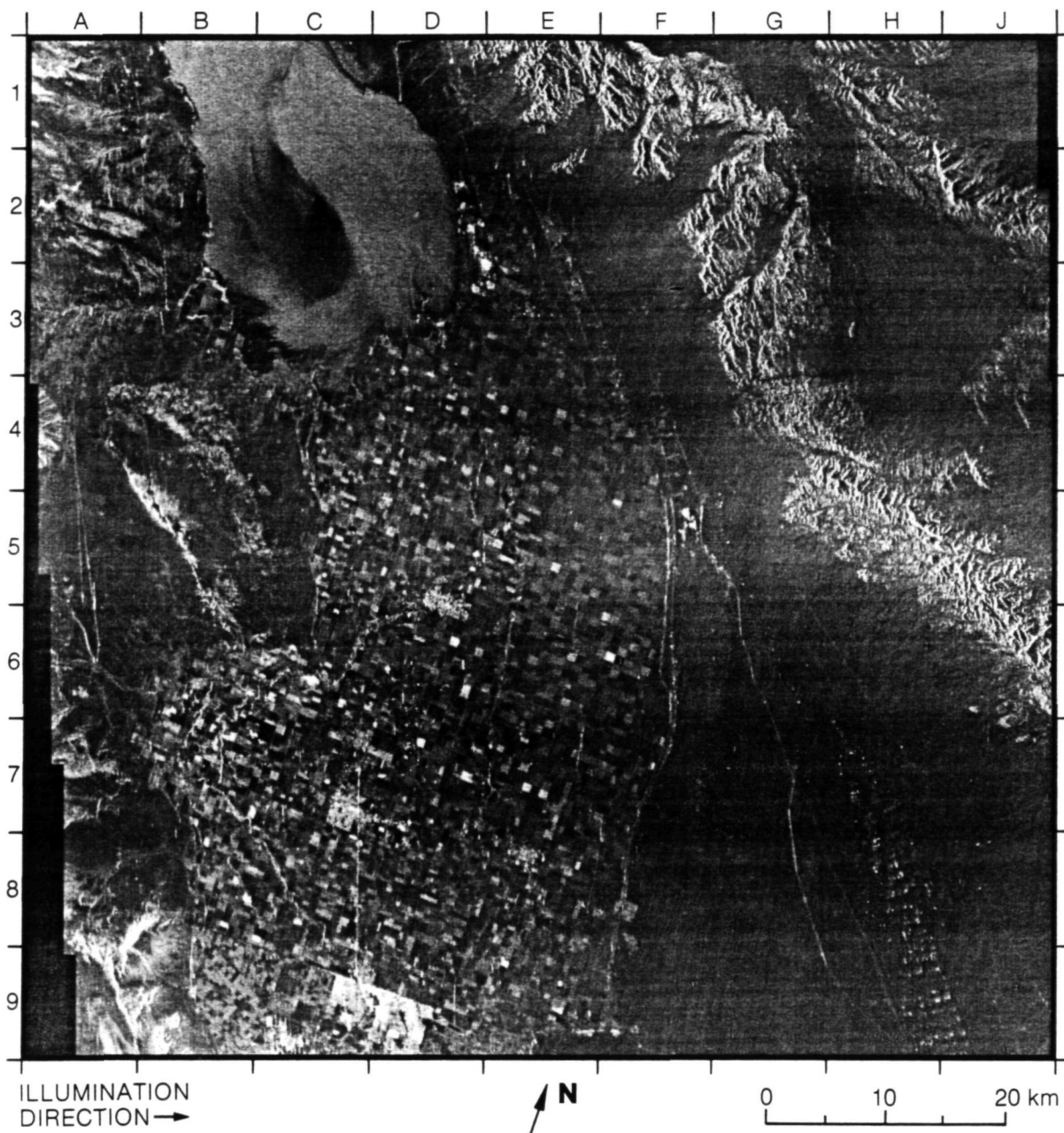
The Imperial Valley of California is one of the richest agricultural areas in the state. Approximately 1000 square kilometers are irrigated by 4800 kilometers of canals and ditches, of which the major ones are evident on the radar imagery. At the time this image was obtained, the fields that show the checkerboard pattern were growing alfalfa and cotton, and many were fallow. Accurate distinction of the respective ground cover is not possible from the SAR image. The Salton Sea is located in the upper left portion of the image. The water in this salt lake has a surface elevation of approximately -70 meters. The level fluctuates, but inflow is maintained from the drainage of irrigated areas and from the Alamo River and the New River. The patterns on the surface of the Salton Sea result from variations in the surface roughness due to wind. Several of the populated areas are easily identified by their light gray tone and distinctive

SALTON SEA

COACHELLA CANAL

EAST HIGHLINE CANAL

CHOCOLATE MOUNTAINS

BRAWLEY

NEW RIVER

ALAMO RIVER

Naval Air Facility

IMPERIAL

EL CENTRO

HOLTVILLE

UNITED STATES
MEXICO

CALEXICO

MEXICALI

BAJA CALIFORNIA

CALIFORNIA

ALL AMERICAN CANAL

Legend:

- URBAN AREAS
- SAND HILLS
- RIVERS
- – – – INTERNATIONAL BOUNDARY
- – – – – CANALS
- ++++++ RAILROADS

N

0   10   20 km
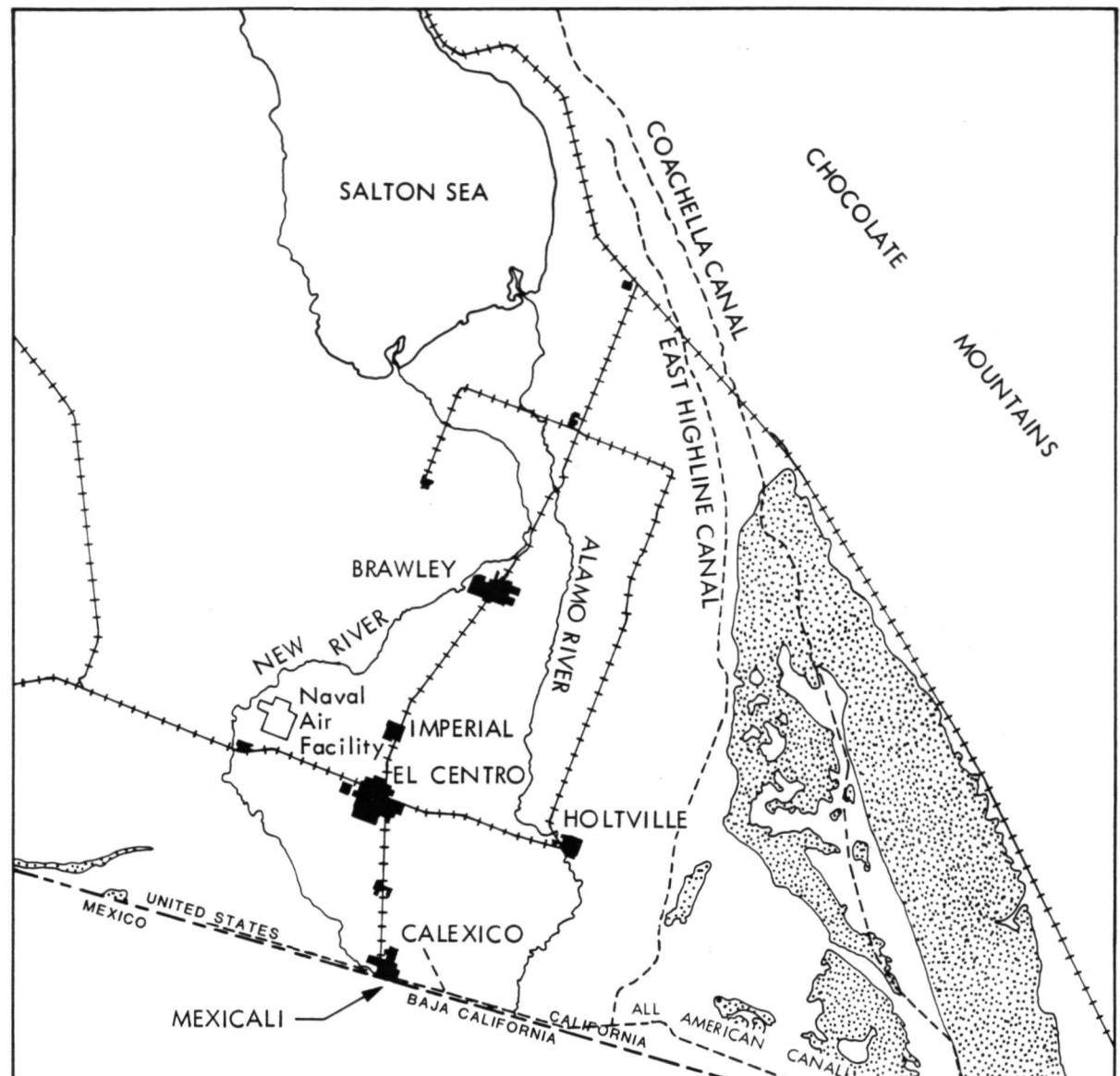
image texture. These include Imperial, El Centro, Calexico, and its Mexican counterpart, Mexicali. Several of the railroads and canals (specifically the railroad between Calexico and Imperial and the Coachella Canal through the Sand Hills) are emphasized on the SAR image because of their orientation relative to the radar illumination direction. The very dark area at B6 is the smooth surface of the Naval Air Facility at El Centro, and the extremely bright dot at C6 is the Holly Sugar Refinery, which forms an exceptionally good metallic reflector. The Sand Hills to the southeast are discussed in detail under Algodones Dunes, California. An offset of the image at E3 and F3 is the result of an STC change during image acquisition.

(Seasat image from Rev. 882.)

121

41. Plains of Southwest Kansas

ILLUMINATION
DIRECTION→

N

0   10   20 km
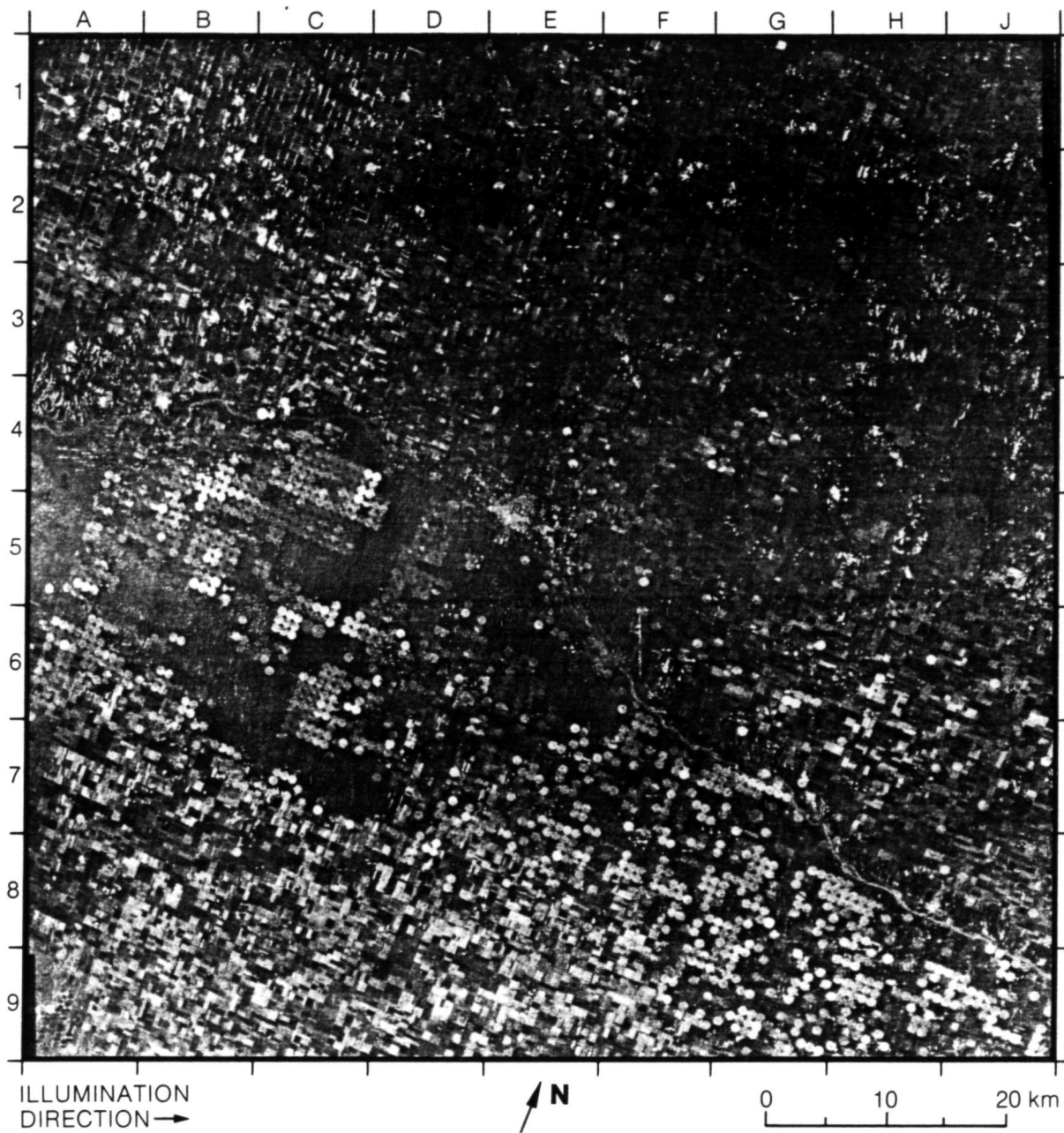
This area of southwest Kansas, centered approximately on Garden City, Kansas, (E5) has four major features that are identifiable on the radar image. In the center is Garden City, the only major urban area within the scene. The Arkansas River traverses the area from west to east (A4 to J9) across the image and to the south of Garden City. Other drainage features are seen along the northeastern portion (e.g., J3) of the image and to the west of Garden City (e.g., B2) where the gently rolling topography is dissected by the dendritic drainage. Thus randomly oriented slopes provide strong returns to the radar antenna. Portions of the Cimarron River drainage (A9) are also clearly identified in the southwestern portion of the image. South of the Arkansas River there are

MB

URBAN AREAS ———— HIGHWAYS

SAND HILLS –·–·– INTERMITTENT STREAMS

———— COUNTY BOUNDARIES

↗N 0   10   20 km
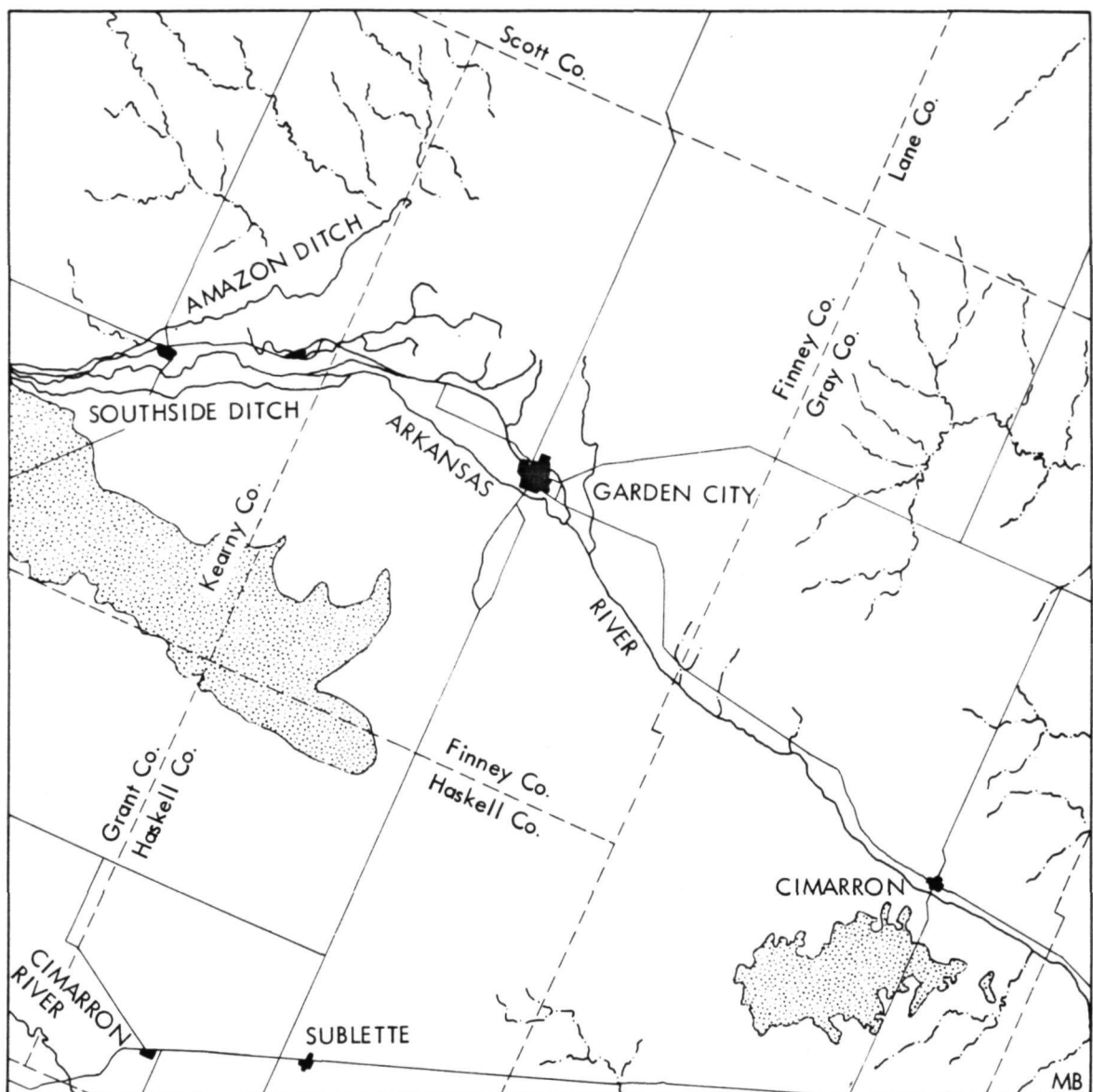
numerous features that reflect the use of circular irrigation (e.g., C5). Most of the circular features are centered on quarter-section fields with approximately three-quarters of each field being irrigated. A discussion of circular irrigators used on the American Great Plains is given by Splinter (1976). Southwest of Garden City is a large area composed primarily of randomly spaced, small white spots (A5). This area is of sand hills (compare, for example, with the image of the Algodones Sand Dunes). This area lacks the patterns of either the irrigation or the drainage networks. The remainder of the image is dominated by rectangular patterns common in the agricultural areas of the Great Plains.

(Seasat image from Rev. 1254.)

123

Appendix A
Characteristics of the Seasat SAR

The main characteristics of the Seasat SAR are summarized in Table A-1. Figure A-1 is an artist's sketch of the Seasat satellite showing the locations of the different sensors.

The Seasat SAR is an L-band (23.5-cm wavelength) synthetic-aperture system that generated two-dimensional radar-reflectivity images of the Earth's surface. For details on the principle of the synthetic-aperture formation, the reader is referred to the literature by Jensen, et al. (1977), Tomiyasu, (1978), and Elachi (1980).

The functional diagram of the Seasat SAR is shown in Figure A-2. The antenna consists of a phased-array system, 10.74 meters long by 2.16 meters wide, that was deployed after orbit insertion. The long dimension is parallel to the spacecraft velocity vector. The antenna beam width in elevation is 6.2°, centered at a boresight angle of 20° from vertical. It illuminates a 100-kilometer swath on the Earth's surface that

Table A-1. Characteristics of the Seasat SAR

Parameter	Value
Satellite altitude	800 km
Radar frequency	1.275 Ghz
Radar wavelength	23.5 cm
System bandwidth	19 Mhz
Theoretical resolution on the surface	25 × 25 m
Number of looks	4
Swath width	100 km
Antenna dimensions	10.74 × 2.16 m
Antenna look angle	20° from vertical
Incidence angle on the surface	23° ±3° across the swath
Polarization	HH
Transmit pulse length	33.4 μsec
Pulse repetition rate	1463 to 1640 pps
Transmitted peak power	1000 W
Time-bandwidth product	634
Data recorder bit rate (on the ground)	110 Mbits/s (5 bits per word)

extends from 240 kilometers to 340 kilometers to the right of the subspacecraft point. The antenna elements are weighted to reduce the sidelobes in the elevation direction. The antenna length is dictated by the requirement to keep the azimuth sampling ambiguities to an acceptably low level (less than −18 dB). The antenna consisted of eight mechanically deployed, electrically coupled, flat microstrip honeycomb panels.

The radar sensor consists of four subassemblies: transmitter, receiver, power converter, and logic and control. To provide the required transmitter average power, a chirped pulse was used to reduce the peak power requirements. The linearly-swept, frequency-modulated (i.e., chirp) pulse had a compression ratio of 634:1. It was generated in a surface acoustic wave (SAW) device. The output power stage consists of three parallel power amplifiers that provided a total peak power of 1000 watts to the antenna.

The echo returns were coupled into the receiver through the output network. To compensate for the variation of the antenna gain with the elevation angle, a sensitivity time control (STC) was incorporated in the receiver. The receiver output was sent directly to the data link along with timing- and frequency-reference signals.

The data-link subsystem translated the received L-band echo up to S-band (2.265 GHz), orthogonally combined the offset video with both PRF and stable reference, and transmitted the resulting signal to the ground.

On the ground, the data link signal translated down to an offset video frequency centered at 11.25 MHz, coherently demodulated the received signal with the reference signal, removed the link-induced doppler, and reconstructed the PRF and local oscillator signals from the video. The echo data were then digitized, buffered, formatted, and recorded on a high-density digital recorder (HDDR) at a rate of 100 Mbits/s.

BUS

SOLAR
ARRAY

FLIGHT PATH

TELEMETRY, TRACKING,
AND COMMUNICATION
ANTENNA No. 2

SCATTEROMETER
ANTENNAS

SYNTHETIC APERTURE
RADAR ANTENNA

SENSOR
MODULE

TELEMETRY, TRACKING,
AND COMMUNICATION
ANTENNA No. 1

VISIBLE-INFRARED
RADIOMETER

MULTICHANNEL
MICROWAVE RADIOMETER

LASER RETROREFLECTOR

SAR DATA
LINK ANTENNA

ALTIMETER
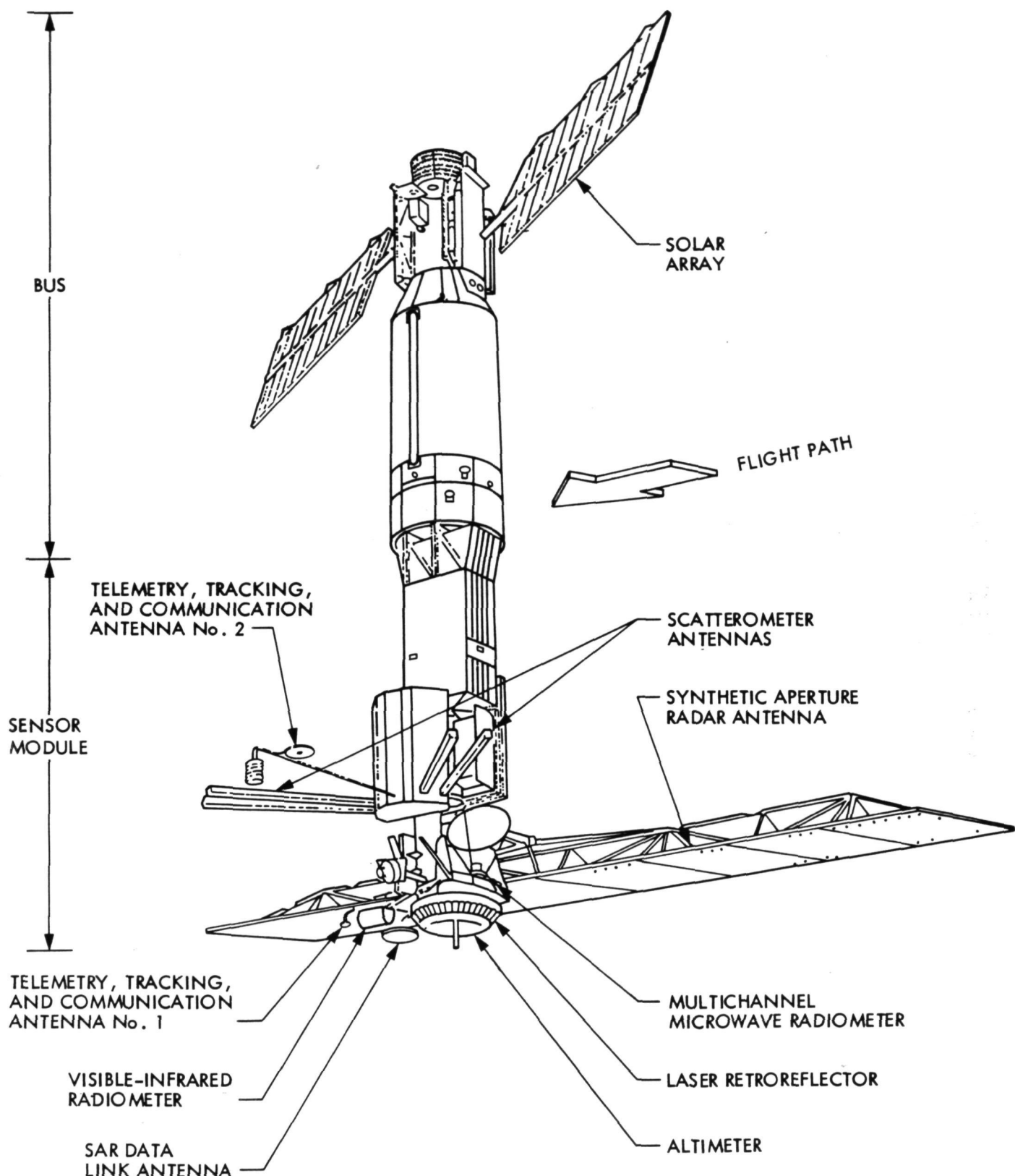
Figure A-1. Seasat bus and payload configuration

127
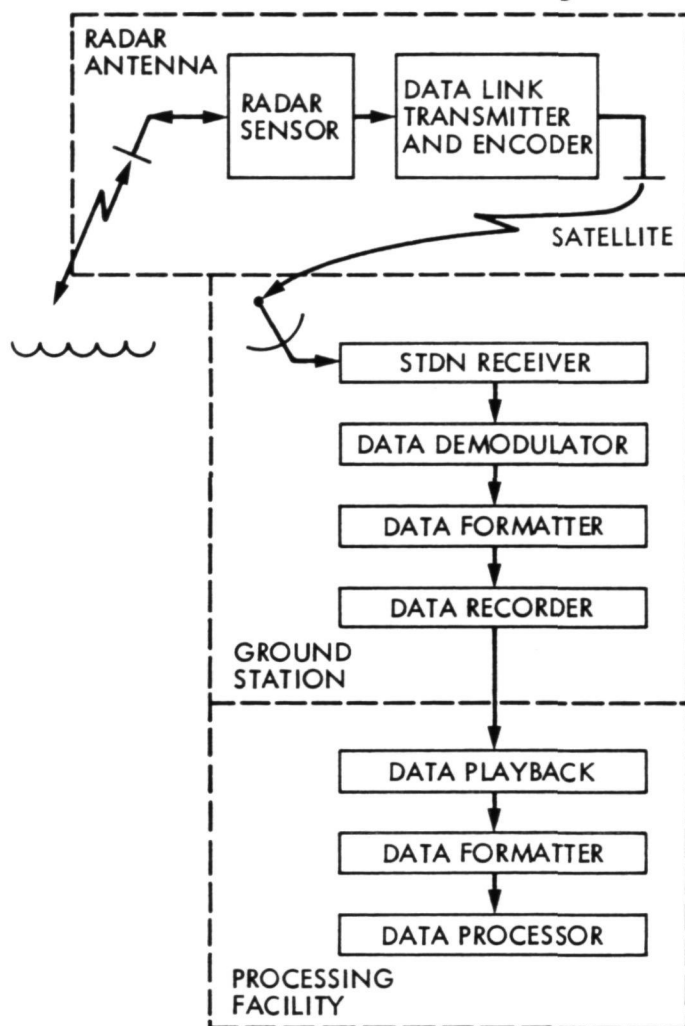
Figure A-2. Seasat SAR system functional block diagram

Appendix B
Glossary of Acronyms and Technical Terms

aa	basaltic lava flow with rough, splintery surfaces
aeolian features	formed by wind action
alluvial fan	cone-shaped deposit formed where a stream issues from mountains onto lowlands
anticline	folded-rock structure whose limbs dip away from the fold axis
azimuth	bearing of a line measured clockwise from geographic north
azimuth (radar imaging)	along-track direction of image acquisition
backscatter (radar)	portion of transmitted microwave energy that is reflected back to the radar antenna to create a radar image
backslope	slope that is inclined away from an incident radar beam
band	an interval in the electromagnetic spectrum whose boundaries are marked by a lower and an upper limiting wavelength, or frequency. The bands used in radar were initially given letter codes for reasons of military security. The letter codes have been declassified, but they are retained for convenient reference. The radar bands mentioned in this atlas are:

Band	Approximate Wavelength
L	15 to 30 cm
S	15.0 to 7.5 cm

The bands used on Landsat are numbered from 1 to 7. Bands 1 to 3 were used on Landsats 1 and 2 to record terrain brightness on a three-television-camera system. The system produced few images and was replaced on Landsat 3 with a single wide-band camera. Bands 4 to 7 on Landsats 1, 2, and 3 designate channels of the respective multispectral scanners that detect solar radiation reflected from the Earth's surface as listed below:

Band	Type of Radiation	Wavelength
4	Visible green	0.5 to 0.6 μm
5	Visible red	0.6 to 0.7 μm
6	Invisible reflected Infrared	0.7 to 0.8 μm
7	Invisible reflected Infrared	0.8 to 1.1 μm

caldera	large circular depression in volcanic terrain that originates from collapse, or explosion, or erosion
correlation (radar)	processes by which the Doppler phase histories recorded on tape or radar signal film are converted into radar images, using optical or digital techniques

decimeter spectral range	portion of the electromagnetic spectrum (qv) from 10.0- to 99.9-cm wavelength
dielectric constant	ratio of the electric flux density to the electric field; identical with dielectric permittivity
drumlin	a streamlined hill in the form of an elongated ellipse, up to 75 meters high, with a notably steep slope at one end. Drumlins occur in swarms with their long axis oriented approximately parallel to the flow direction of the glacial ice from which they were formed
electromagnetic spectrum	an ordered progression of radiations that includes cosmic, gamma, X, ultraviolet, visible, infrared, microwave, and radiowave energy
elevation (sun)	inclination of the sun to the horizontal
fissure eruption	emanation of lava or pyroclastic fragments from a comparatively narrow fissure
flood plain	the portion of a river valley built of sediment deposited by an existing river; the plain is covered with water when the river overflows its banks
foreslope	slope that is inclined toward an incident radar beam
glacial outwash	deposits, beyond active glacial ice, formed from meltwater streams
graben	elongated block that has been downthrown along faults that form its margins
granodioritic gneiss	banded metamorphic rock (qv) containing quartz in conjunction with plagioclase and orthoclase feldspar and mafic silicate minerals in distinct proportions
hammack	a term parochial to the Florida Everglades that denotes a cluster of trees that form a small island in the swamp
HDDR	high density digital recorder
hogback	name applied in the Rocky Mountain region to a sharp-crested ridge underlain by steeply dipping resistant rock strata
igneous rock	rock solidified from a former molten state
image	visual reproduction of a scene acquired by SAR, MSS, RBV, or photographic sensor
imbricate thrusting	deformation that produces a series of shingling or overlapping thrust sheets that all dip in the same direction

incidence angle (radar)	angle between the incident radar beam at the ground and the normal to the ground surface at the point of incidence
karst	an irregular hummocky plateau marked by subsurface drainage and numerous sinkholes interspersed with abrupt ridges. The subsurface is characterized by caverns and features formed by the solution and collapse of limestone
lacustrine	of or pertaining to a lake
Landsat	any of a series of orbital imaging satellites that measure and record reflectance from the Earth's surface at visible and infrared wavelengths. Landsat 1 was launched in July 1972. It was followed by Landsats 2 and 3 in January 1975 and March 1978, respectively. At the time of this writing, only Landsats 2 and 3 remain operative. For details of the Landsat imaging systems and supporting activities, see *Landsat Data User's Handbook*, 3rd edition, 1979, and updates, available from the U.S. Geological Survey, Arlington, VA
layover (radar)	geometric displacement of the top of a feature toward the near range on radar imagery
L-band	see band
look angle (radar)	angle between the vertical plane and the line that links an imaging-radar antenna to a feature on the ground
look direction (radar)	direction in which pulses of microwave energy are transmitted from an imaging-radar antenna; normally at right angles to the line of flight of the imaging platform
meander	any of a series of C-shaped loops that form part of a sinuous stream channel
meander scar	outline of an erstwhile meander that has been cut off from a stream channel and filled with sediment that commonly supports a distinctive vegetation
metamorphic rock	rock altered from an original condition by elevated temperature and/or pressure that produces a change of texture and mineralogy
microwave	any electromagnetic wave having a wavelength in the interval between one millimeter and one meter
monocline	a single-limbed, folded-rock structure in strata that are otherwise flat-lying
moraine	feature formed of unsorted, unstratified sediment transported and deposited by glacial ice
MSS	multispectral scanner (qv)

multispectral scanner	an airborne or spaceborne imaging system that acquires images by scanning a scene in several wavelengths simultaneously
nadir	point on the ground vertically beneath the SAR antenna
nunatak	an isolated rock peak that projects through the surface of a glacier
pahoehoe	basaltic lava flow with smooth, ropy surfaces
permafrost	perennially frozen ground. Occurs over large areas of the high northern latitudes in depths up to 1000 meters. In summer, the ground generally thaws to shallow depths, creating an annual cycle of freeze and thaw
pixel	picture element
plutonic rock	igneous rock formed and emplaced in the Earth's crust at depth below the surface
point-bar	feature formed from sediment deposited along the inside curve of a growing meander loop
PRF	pulse repetition frequency
pyroclastic rock	rock formed by the accumulation of fragments scattered by volcanic explosions
radar	radio detection and ranging; radar is used in remote sensing for measuring and mapping the Earth and planetary surfaces
range (radar imaging)	across-track direction of image acquisition
RBV	return-beam vidicon (qv)
resolution element	the minimum distance between two adjacent features on the ground, or the minimum size of a feature on the ground, that can be detected by an imaging system
return-beam vidicon	a modified television camera tube in which the screen is scanned by an electron beam to detect minute voltages that are used to form images. The RBV on Landsat 3 is a wideband sensor that operates at optical wavelengths from 0.505 to 0.750 μm
returns (radar)	backscatter (qv)
rhyolitic	silica-saturated volcanic igneous rock or magma
rift zone	fault trough formed in a divergent zone of tension in the Earth's crust
SAR	synthetic-aperture radar (qv)
SAW	surface acoustic wave

S-band	see "band"
scarp	cliff or steep slope of some extent that may form a marked topographic boundary
scene	area covered by SAR, MSS, RBV, or photographic image
Seasat	an Earth-orbiting satellite equipped with five instruments, including a side-looking synthetic-aperture imaging radar system, for studying ocean dynamics
sedimentary rock	rock formed from the accumulation of particles of preexisting rock, or from chemical or biochemical precipitation
sensitivity time control	a device on the Seasat SAR receiver to compensate for variations of the antenna gain
shadow (radar)	an area of no radar backscatter on an image caused by a ground feature that obstructs the radar beam and prevents illumination of the area behind it
shield volcano	a large broad volcanic cone with very gentle slopes built up of nonviscous basaltic flows
specular (reflections)	mirror-like returns of a radar signal
STC	sensitivity time control (qv)
STDN	Spacecraft Tracking and Data Network
strike	bearing of an inclined bed or structure on a level surface
strike-slip fault	fault in which the movement of the rocks on each side of the fault plane is predominantly horizontal. The displacement is either left-lateral or right-lateral depending on the direction of movement of the far block as viewed from either side of the fault
syncline	folded-rock structure whose limbs dip toward the fold axis
synthetic-aperture radar	a side-looking airborne or spaceborne imaging system that uses the Doppler principle to sharpen the effective beamwidth of the antenna. The result is improved resolution in the azimuth direction and constant resolution in the range direction. The radar backscatter is recorded on tape or on film and must be digitally or optically processed to form radar images
tephra	collective term for all clastic volcanic materials ejected from a crater or other type of vent and transported through the air
thermokarst	settling or caving of the ground due to melting of ground ice. Occurs in the Arctic and forms irregular topography that resembles karst (qv)

thrust fault   low-angle dip-slip fault in which the block above the fault
                      plane moves up and over the lower block

volcanic rock   igneous rock formed by eruption at the Earth's surface

water table   a subsurface plane or datum that marks the upper level of the
                      zone of groundwater saturation. Commonly fluctuates on a
                      seasonal basis, and with usage

Appendix C
Index of Images

Image No.	Seasat Image Title	Seasat Rev. No.	Date, 1978	Center Coordinates Latitude, N	Center Coordinates Longitude, W	Corresponding Image	Band	Date	Scene ID	Sun Angle Elevation	Sun Angle Azimuth	Caption's Author [a]
1	Folded Appalachians, Pennsylvania (I)	1296	Sept. 25	40°26'	77°15'	Sketch map				–	–	JPF
2	Folded Appalachians, Pennsylvania (II)	759	Aug. 19	40°22'	77°20'	Landsat MSS	7	Jan. 10, 1973	1171-15245	22°	151°	JPF
3	Sierra Madre Oriental, Mexico	738	Jul. 17	27°21'	101°40'		7	Mar. 18, 1975	2055-16372	46°	124°	JPF
4	Ouachita Mountains, Oklahoma-Arkansas	795	Aug. 21	34°40'	94°16'		7	Jan. 5, 1976	5261-15492	22°	147°	HCM
5	Arkoma Basin, Oklahoma-Arkansas	795	Aug. 21	35°20'	94°35'		7	Dec. 19, 1975	5244-15555	Average 21.5°	Average 142°	HCM
							7	Jan. 5, 1976	5261-15492			
							7	Jan. 5, 1976	5261-15490			
							7	Dec. 19, 1975	5244-15561			
6	Kettleman Hills, California	574	Aug. 6	36°00'	120°00'	Landsat MSS						RGB
7	San Rafael Swell, Utah	853	Aug. 25	39°10'	110°35'	Sketch map	7	Sept. 29, 1972	1068-17364	42°	145°	RGB
8	San Andreas Fault, Southern California	351	Jul. 21	34°15'	118°10'	Landsat MSS	7	Dec. 20, 1976	2698-17371	23°	146°	JPF
9	Great Glen Fault, Scotland	719	Aug. 16	57°00'	4°48'		7	Jan. 30, 1976	2373-10414	11°	153°	JPF
10	Pine Mountain Thrust Fault, Tennessee-Kentucky-Virginia	407	Jul. 25	36°38'	84°01'		6	Nov. 28, 1974	1858-15303	26°	150°	JPF
11	Algodones Dunes, California	1140	Sept. 14	32°55'	115°05'	Landsat MSS	7	Aug. 4, 1976	5473-16551	48°	102°	RGB
12	Sonora Dunes, Sonora, Mexico	1140	Sept. 14	32°00'	114°15'	Landsat RBV	Optical Wideband	Oct. 5, 1978 / Oct. 22, 1978	30214-17343B / 30231-17285A	Average 42°	Average 140°	RGB
13	Medicine Lake Highland, California	1406	Oct. 3	41°40'	121°30'	Sketch map				–	–	RGB
14	Newberry Volcano, Oregon	681	Aug. 13	43°40'	121°00'	Sketch map				–	–	RGB
15	Coconino Plateau, Arizona	322	Jul. 19	35°45'	111°20'	Landsat MSS	7	Oct. 30, 1973	1464-17354	35°	151°	MID
16	Askja Caldera, Iceland	719	Aug. 16	65°05'	17°00'	Landsat MSS	7	May 30, 1976	2494-11503	44°	156°	DE
17	Unimak Island, Alaska	605	Aug. 8	54°45'	164°10'	Sketch map				–	–	MID
18	Jamaica, West Indies	608	Aug. 8	18°07'	77°10'					–	–	THD
19	Northeast Dominican Republic	335	Jul. 20	19°22'	70°20'					–	–	THD
20	Dease Inlet, Alaska	322	Jul. 19	70°52'	155°45'	Sketch map				–	–	JPF
21	Drumlin Field, Ireland	791	Aug. 22	54°12'	7°17'	Landsat MSS	7	Jun. 30, 1977 / Apr. 21, 1976	5803-20324 (ruth 223, rows 22 to 24)	39°	144°	JPF
22	Death Valley, California	1140	Sept. 14	36°20'	116°50'	Landsat MSS	7	Oct. 30, 1973	1464-17354	35°	151°	MID
23	Grand Canyon, Arizona	322	Jul. 19	36°24'	111°50'	Landsat MSS	7	Jul. 13, 1979	21633-20531	40°	163°	MID
24	Camden Bay, Alaska	781	Aug. 20	70°05'	145°00'	Landsat MSS	7					JPF
25	Southern California Coast	1291	Sept. 24	33°17'	117°37'	Sketch map				–	–	ECX
26	Wabash/Ohio Rivers, Kentucky-Indiana-Illinois	565	Aug. 5	38°00'	87°55'	Sketch map				–	–	JPF
27	Sierrita Mountains, Arizona	523	Aug. 2	32°00'	111°10'	Landsat MSS	7	Dec. 21, 1973	10516-17250	28°	142°	MID
28	Everglades National Park, Florida	809	Aug. 22	25°23'	80°46'	Landsat MSS	7	May 16, 1978	21210-14475	54°	93°	THD
29	Gulf Coastal Wetlands, Louisiana	795	Aug. 21	29°55'	91°57'	Landsat MSS				–	–	MLB
30	Lower Chesapeake Bay, Virginia	1468	Oct. 7	37°15'	75°48'					–	–	THD
31	Mount McKinley National Park, Alaska	380	Jul. 23	63°03'	150°15'	Sketch map				–	–	JPF
32	Godthåbsfjord-Isua Region, Southern West Greenland	1490	Oct. 9	64°00'	49°00'	Landsat MSS	7	Oct. 14, 1973	1448-14124	16°	167°	JPF
33	The Nation's Capital	558	Aug. 5	38°53'	77°01'	Sketch map				–	–	NLB
34	Los Angeles, California (I)	660	Aug. 12	34°05'	118°04'	Landsat MSS composite	4, 5, 7	Oct. 21, 1972	1090-18012	39°	148°	NLB
35	Los Angeles, California (II)	351	Jan. 21	34°04'	118°05'	Aerial photograph	Optical	Sept. 2, 1979	NASA-JSC Flight 408	–	–	MLB
36	Denver, Colorado	580	Aug. 6	39°28'	104°58'	Sketch map				–	–	MLB
37	New Orleans, Louisiana	788	Aug. 21	30°00'	90°00'	Facing Seasat Image				–	–	MLB
		838	Aug. 24	30°07'	90°05'	Facing Seasat Image				–	–	
38	Geneva, Switzerland	762	Aug. 19	46°17'	6°12' E	Sketch map				–	–	FF
39	Plains of Central Iowa	723	Aug. 16	42°20'	93°18'	Sketch map				–	–	MLB
40	Imperial Valley, California	882	Aug. 27	33°04'	115°27'					–	–	MLB
41	Plains of Southwest Kansas	1254	Sept. 22	37°56'	100°52'	Sketch map				–	–	MLB

[a] Author abbreviations:

JPF	J. P. Ford	HCM	H. C. MacDonald
RGB	R. G. Blom		
MID	M. I. Daily		
DE	D. Evans		
THD	T. H. Dixon		
ECX	E. C. Xenos		
MLB	M. Leonard Bryan		
FF	F. Fanier		

References

Beal, R. C., 1980, "Spaceborne Imaging Radar: Monitoring Ocean Waves," *Science,* Vol. 208, No. 4450, pp. 1373-1375.

Elachi, C., 1980, "Spaceborne Imaging Radar: Geologic and Oceanographic Applications," *Science*, Vol. 209, No. 4461, pp. 1073-1082.

Ford, J. P., 1980, "Seasat Orbital Radar Imagery for Geologic Mapping: Tennessee-Kentucky-Virginia," *Amer. Assoc. Petroleum Geologists Bull.*, in press.

Henderson, F. M., S. W. Wharton, and D. L. Toll, 1980, "Preliminary Results of Mapping Urban Land Use Cover With Seasat SAR Imagery," in *Technical Papers of the American Society of Photogrammetry ACSM-ASP Convention*, St. Louis, Missouri, March 9-14, 1980, Amer. Soc. Photogrammetry, Falls Church, Va., pp. 310-317.

Jordan, R.L., 1980, "The Seasat-A Synthetic-Aperture Radar System," IEEE, *Jour. Ocean Engineering*, Vol. OE-5, No. 2, pp. 154-164.

Long, M. W., 1975, *Radar Reflectivity of Land and Sea*, D. C. Heath and Co., Lexington, Mass., 366 p.

Jensen, H., L. C. Graham, L. J. Porcello, and E. N. Leith, 1977, "Side-Looking Airborne Radar," *Scientific American*, Vol. 237, No. 4, pp. 84–95.

Sabins, F. F., R. G. Blom, and C. Elachi, 1980, "Seasat Radar Image of San Andreas Fault, California," *Amer. Assoc. Petroleum Geologists, Bull.*, Vol. 64, pp. 619–628.

Splinter, W. E., 1976, "Center-Pivot Irrigation," *Scientific American*, Vol. 234, No. 6, pp. 90–99.

Tomiyasu, K., 1978, "Tutorial Review of Synthetic-Aperture Radar (SAR) With Applications to Imaging the Ocean Surface," *IEEE proceedings*, Vol. 66, No. 5, pp. 563-583.

U.S. Geological Survey, 1973, *Land Use Map, 1970, Washington Urban Area, D. C., Md., and Va.*, Misc. Investigation Series, Map I-858-A.

U.S. Geological Survey, 1973, *Annotated Orthophoto Map, 1970, Washington Urban Area, D.C., Md., and Va.*, Misc. Investigation Series, Map I-858-B.

U.S. Geological Survey, 1974, *Denver, Colorado, Topographic Map*, scale 1:250,000 — revision of 1953 ed., Washington, D.C.

Wu, C., 1980, "A Digital Fast Correlation Approach to Produce Seasat SAR Imagery," *IEEE 1980 International Radar Conference*, Arlington, Va., pp. 153–160.

Preceding page blank